ULTRAFAST SPECTROELECTROCHEMISTRY OF MIXED IONIC–ELECTRONIC POLYMER CONDUCTORS

A THESIS SUBMITTED TO

THE GRADUATE SCHOOL OF ENGINEERING AND SCIENCE

OF BILKENT UNIVERSITY

IN PARTIAL FULFILLMENT OF THE REQUIREMENTS FOR

THE DEGREE OF

MASTER OF SCIENCE

IN

CHEMISTRY

By

Fatma Altuğ

September 2025

Ultrafast Spectroelectrochemistry of Mixed Ionic–Electronic Polymer Conductors
By Fatma Altuğ
September 2025

We certify that we have read this thesis and that in our opinion it is fully adequate, in scope and in quality, as a thesis for the degree of Master of Science.

Burak Ülgüt(Advisor)

Emrah Özensoy

J. Tyler Mefford

Approved for the Graduate School of Engineering and Science:

Orhan Arıkan
Director of the Graduate School

ABSTRACT

ULTRAFAST SPECTROELECTROCHEMISTRY OF MIXED IONIC–ELECTRONIC POLYMER CONDUCTORS

Fatma Altuğ
M.S. in Chemistry
Advisor: Burak Ülgüt
September 2025

Electron transfer and switching mechanisms in conducting polymers remain an open question. When conventional electrochemical techniques such as cyclic voltammetry are employed alone, the measured current inevitably contains contributions from both the redox process of the polymer and the capacitive charging current arising from the voltage-dependent capacitance. Thus, isolating the pure redox current requires additional deconvolution methods. Furthermore, the conventional understanding, repeatedly emphasized in the literature, is that electron transfer in conducting polymers proceeds through an ion-coupled mechanism, in which counter-ions from the electrolyte penetrate into the polymer to maintain charge neutrality.

In this thesis, we challenge this conventional description by employing *operando* ultrafast cyclic voltammetry–UV–Vis spectroscopy, in which the potential is rapidly scanned within a defined range while the spectroscopic response is simultaneously recorded. By extending the sweep rate up to 200,000 V/s, we aimed to suppress net counter-ion displacement. Under these conditions, the observed color change demonstrated that electron transfer can occur even in the absence of ion participation.

To this end, *operando* ultrafast cyclic voltammetry–UV–Vis spectroscopy was utilized. The average spectroscopic responses obtained at ultrafast cycles were deconvoluted into their minimal components using principal component analysis (PCA), and the dependence of the resulting coefficients on the sweep rate was systematically examined. Analysis of these coefficients revealed that, with increasing sweep rate, the relative lifetime of the more oxidized and reduced states changes: counter-ion diffusion becomes increasingly limited, making doping less

efficient and leading to a greater contribution from the reduced state. Moreover, optical charge values derived from the PCA coefficients approached steady-state at high sweep rates. These findings provide direct spectroscopic evidence that electron transfer in conducting polymers can proceed independently of ion motion under ultrafast potential modulation.

Keywords: Conducting polymers; Electron transfer; Ion-coupled mechanism; Ion-free electron transfer; Ultrafast cyclic voltammetry; Spectroelectrochemistry; Counter-ion diffusion; Principal component analysis (PCA).

ÖZET

KARIŞIK İYONİK–ELEKTRONİK POLİMER İLETKENLERİN ULTRA HIZLI SPEKTROELEKTROKİMYASI

Fatma Altuğ
Kimya, Yüksek Lisans
Tez Danışmanı: Burak Ülgüt
Eylül 2025

İletken polimerlerde elektron transferi ve anahtarlama mekanizmaları halen tam olarak aydınlatılamamıştır. Geleneksel elektrokimyasal yöntemlerden biri olan çevrimsel voltametri tek başına kullanıldığında, ölçülen akım hem polimerin redoks süreçlerinden hem de voltaja bağlı olarak değişen kapasitansın oluşturduğu kapasitif akımdan katkılar içerir. Bu nedenle, yalnızca redoks akımını izole etmek ek ayrıştırma yöntemleri gerektirir. Ayrıca, literatürde sıklıkla vurgulanan geleneksel anlayışa göre, iletken polimerlerde elektron transferi, polimerin yük nötrlüğünü sağlamak amacıyla elektrolitten polimer içine giren karşı iyonlarla eşleşen iyon-bağımlı bir mekanizma üzerinden gerçekleşmektedir.

Bu tezde, bu geleneksel açıklamaya alternatif bir bakış açısı sunmak amacıyla *operando* ultrahızlı çevrimsel voltametri–UV–Vis spektroskopisi kullanılmıştır. Bu yöntemde, potansiyel belirli bir aralıkta çok yüksek hızlarda taranırken eşzamanlı olarak spektroskopik yanıt kaydedilmiştir. Tarama hızının 200,000 V/s seviyelerine çıkarılmasıyla karşı iyonların net yer değiştirmesi baskılanmış, bu koşullar altında gözlemlenen renk değişimi ise elektron transferinin iyon katılımı olmadan da gerçekleşebileceğini ortaya koymuştur.

Bu amaç doğrultusunda elde edilen ultrahızlı çevrimlerden alınan ortalama spektroskopik yanıtlar temel bileşen analizi (PCA) ile en az sayıda bileşenine ayrılmış ve bu katsayıların tarama hızına bağımlılığı sistematik olarak incelenmiştir. Analizler sonucunda, artan tarama hızlarıyla birlikte daha oksitlenmiş ve daha indirgenmiş durumların görece ömürlerinin değiştiği; karşı iyon difüzyonunun sınırlanmasıyla dopinglemenin zorlaştığı ve bu nedenle indirgenmiş durumun katkısının arttığı görülmüştür. Ayrıca PCA katsayılarından

türetilen optik yük değerlerinin yüksek tarama hızlarında dengeye ulaştığı sonucuna varılmıştır. Bu bulgular, iletken polimerlerde elektron transferinin, ultrahızlı potansiyel modülasyon koşullarında iyon hareketinden bağımsız olarak gerçekleşebileceğine dair doğrudan spektroskopik kanıtlar sunmaktadır.

Anahtar sözcükler: İletken polimerler; Elektron transferi; İyon-bağlantılı mekanizma; İyon bağımsız elektron transferi; Ultra hızlı döngüsel voltametri; Spektroelektrokimya; Karşı-iyon difüzyonu; Temel bileşen analizi (PCA).

Acknowledgement

At this very moment, as I begin writing this part of my thesis, I am also closing another chapter of my life. Bilkent has been a long journey for me; however, the past three years, since joining the Ülgüt Research Group, have truly marked the real beginning. I consider the night I first dreamed of the project I have been working on for three years as the turning point of my life. Through this project, I grew, learned, stumbled, got back up, and I continue to add to what I have learned.

First and foremost, I would like to sincerely thank my advisor, Burak Ülgüt, for welcoming me into the most reliable, embracing, and home-like laboratory. Professor, I still don't know what I will "become" when I grow up, but I am deeply grateful to you for giving me such an exciting and strong starting point in the world of electrochemistry. From you, I learned not only electrochemistry but also that whatever work we do, it should be carried out in the most accurate, meticulous, and careful way. You taught me to be my own critic. The meaningful books you gifted us will always remain in my library, and you will always be a role model for me.

And of course, to the wonderful people in my lab... I would especially like to thank Ezgi Sevgen, with whom I shared endless laughter and an unforgettable Middle East adventure. I am also grateful to Gökberk Katırcı, Fazlı Eren Cıvan, and Gözde Ataç, Bilsu Özkaya for their friendship and support throughout this journey. I know this project will be in good hands with you, Bilsu.

To my dearest friends, my STEM girls, Gözde Ceran, Almila Kura, Selin Kasap, and İrem İlter. The time I spent with you has always been very precious and will always remain so.

To my family, who shared my burdens, stressed with me, and relaxed with me throughout this long journey thank you endlessly. The greatest gift you gave me was always supporting me while allowing me the freedom to make my own

choices.

Finally, to my beloved Osman Örnek, whom I was lucky enough to meet in 2023. You brighten my life every single day, and even though we have been in different countries, I have never once felt your absence. Thank you for always being with me from afar, for making me laugh when I need it most, and for caring for me with so much love.

Contents

List of Figures

List of Tables

Chapter 1

INTRODUCTION

This study aims to elucidate the electron transfer mechanism in conducting polymers and to observe the ion-free switching behavior. In such systems, electron and ion transfer are inherently coupled, yet the comparatively sluggish ion motion often limits the overall kinetics. Redox processes in electrochemically active films involve not only the oxidation and reduction of the polymer but also the migration of counter-ions from the electrolyte into the polymer matrix, governed by the principle of charge neutrality. While this mechanism has been well established in conventional conditions, here we explore an unconventional regime, where high voltage sweep rates hinder full ion penetration into the polymer. Under these circumstances, electron transfer may still proceed by overcoming Coulombic repulsion, thereby challenging the conventional understanding of ion–electron coupling. To probe this phenomenon, operando UV–Vis spectroscopy was combined with cyclic voltammetry across a broad range of sweep rates—from slow (100 mV/s) to ultrafast (up to 2×10^5 V/s) using polymer films of varying thickness.

Before turning to these analyses, a theoretical foundation is required to follow the electrochemical processes in detail. We therefore begin with an overview of the fundamental theories describing electron transfer in monolayer and multilayer films, which provide a framework for predicting the role of film thickness in electron transfer kinetics. This starting point is particularly relevant as

the present study examines both thin (< 100 nm) and micron-thick Poly(3,4-ethylenedioxythiophene) (PEDOT) films, enabling us to directly evaluate how thickness influences redox dynamics. Building on this, we review distinct charge storage mechanisms and materials, and evaluate the extent to which cyclic voltammetry can differentiate between them, while also considering its limitations.

Finally, the focus is narrowed to conjugated polymers, the core subject of this thesis, and their charge transfer mechanisms. Electrochromism, a key property of such materials, is introduced in this context, setting the stage for the integration of operando UV–Vis spectroscopy with ultrafast cyclic voltammetry. This approach allows us to distinguish between ion-coupled and ion-free electron transfer pathways under extreme experimental conditions. In the second part of the introduction, we also outline a parallel project in which cyclic voltammetry alone, modeled via fundamental electrochemical equations, is used to separate double-layer charging current from Faradaic current. This complementary study introduces the use of coupled Partial Differential Equation (PDE) systems to model electrochemical processes, providing a broader theoretical and computational backdrop for the experimental investigations presented in this thesis.

1.1 Electron Transfer in Monolayer Films

In this section, we investigate electron transfer processes in monolayer films. In the study forming the basis of this thesis, organic conducting polymers were electrodeposited onto electrode surfaces at varying thicknesses, and their spectroelectrochemical responses were analyzed accordingly. Therefore, we begin by exploring questions such as whether the electron transfer mechanism changes as we move from thin films to thick films, how the parameters affecting electron transfer vary, and which mechanisms play the central role.

A monolayer refers to a single molecule thick film adsorbed on a surface. Although initial studies were conducted on liquid surfaces, molecules were later

adsorbed onto solid surfaces, and subsequently, electrochemically active monolayer films were developed [1]. Monolayers can generally be categorized into two main classes. Langmuir monolayers are based on the organization of amphiphilic molecules containing both hydrophilic and hydrophobic regions at the air-liquid interface in a single molecular layer [2]. This form of organization influences the surface's chemical and physical properties. The second class comprises the self-assembled monolayers (SAMs), which are formed by the adsorption of molecules onto solid surfaces such as silica, metal oxides, or gold. These molecules typically contain functional groups such as thiols, silanes, or phosphonates that spontaneously adsorb onto these surfaces [2].

The first studies on monolayer films were conducted by Irving Langmuir and Henry Devaux in 1917, where they formed monomolecular films of oil molecules on water surfaces [3] . By the 1980s, self-assembled monolayers were successfully constructed on solid surfaces. Jacob Sagiv produced an organosilane-based monolayer on a silica surface [4]. Later, in the 1980s, George Whitesides developed alkanethiol based self-assembled monolayers on gold surfaces [5].

In the following years, redox active monolayer films were developed by incorporating redox active molecules into SAMs. In a study conducted by Chidsey, molecules containing ferrocene groups covalently bonded to alkanethiol chains were synthesized, and these molecules spontaneously bonded to gold surfaces, forming redox-active self-assembled monolayers. This structure enabled the measurement of the electron transfer rate constants between the gold electrode and the ferrocene groups at different temperatures [1].

Bard and Faulkner categorize the methods used to construct monolayer films on electrode surfaces into five main classes: reversible adsorption, irreversible adsorption, covalent attachment, transferred layers, and underpotential deposition. [6, p. 757]

To examine electron transfer mechanisms in electrochemically active monolayers, we begin by introducing the concepts of inner-sphere and outer-sphere electron transfer mechanisms. In inner-sphere electron transfer, a transient chemical

bridge or bond is formed between the electron donor and the electron acceptor during the electron transfer event. The electron is transmitted across this bridge, typically involving a ligand that connects a complex ion to the other reactant. This type of electron transfer is characteristically slow and kinetically controlled. The theoretical basis for this mechanism stems from the Nobel Prize-winning work led by Henry Taube in 1953 [7].

A key question at the time was whether, during an electron transfer reaction such as:

$$\mathrm{Ti}^{3+} + \mathrm{Fe}^{3+} \rightarrow \mathrm{Ti}^{4+} + \mathrm{Fe}^{2+},$$

the electron moved freely through the electrolyte or if groups such as hydroxide (OH^-) or protons (H^+) were simultaneously transferred. It was also unclear how negatively charged ligands like Cl^- and F^- influenced the redox process. Observing these effects was challenging due to the short lifetimes of the reaction intermediates. Taube addressed this limitation by using ions that undergo slower ligand exchange, such as Cr^{2+}. In a reaction between Cr^{2+} and Fe^{3+} in the presence of Cl^-, the resulting Cr^{3+} was found to have a Cl^- ion within its coordination sphere. This demonstrated that Cl^- actively participated in the electron transfer process as a bridging ligand, facilitating inner-sphere transfer. Similar observations were made in experiments with $[\mathrm{Co(NH_3)_6}]\mathrm{Br}^{2+}$, where the Br^- ligand was found to transfer to Cr^{3+}.

Further studies showed that the polarizability and bonding nature of ligands significantly influence the electron transfer rate. For instance, the rate of reduction increases in the following order [7]:

$$[\mathrm{Co(NH_3)_6}]^{3+} < [\mathrm{Co(NH_3)_5(H_2O)}]^{2+} < [\mathrm{Co(NH_3)_5Cl}]^{2+} < [\mathrm{Co(NH_3)_5Br}]^{2+}.$$

For his contributions to understanding the mechanisms of electron transfer, Henry Taube was awarded the Nobel Prize in Chemistry in 1983.

In contrast, outer-sphere electron transfer occurs without the formation of a direct chemical bond between the reactants [6, p. 142]. The electron is transferred through long-range interactions, such as orbital overlap or tunneling, with only electrostatic interaction present.

The inner- and outer-sphere mechanisms described above primarily apply to homogeneous electron transfer reactions, in which both the oxidized and reduced species are in the solution phase. By contrast, in heterogeneous systems, one of the reactants is located on the electrode surface, while the other is in the solution phase.

In heterogeneous systems, outer-sphere mechanisms involve electron transfer without direct adsorption of the redox-active ion onto the electrode surface, and no bridge is formed. On the other hand, in inner-sphere mechanisms, the redox species adsorbs onto the electrode surface, and electron transfer takes place while the species is in the adsorbed state [6, p. 143].

The mechanism of electron transfer depends on various factors such as the distance between redox centers and the nature of the medium through which the electron is transferred. Based on these considerations, electron transfer in monolayers can be studied under several theoretical frameworks: Marcus electron transfer theory, distance-dependent tunneling models and surface-confined redox systems.

We begin with the Nobel Prize-winning Marcus theory. Rudolph A. Marcus proposed that the rate of electron transfer is not solely determined by redox potentials but also by the reorganization (i.e., structural rearrangement) of both reactants and products. According to Marcus, the reaction rate depends on the standard free energy change of the reaction (ΔG°) and the reorganization energy (λ) [8].

Marcus's interest in electron transfer was first sparked in 1955, when he read an article by W.F. Libby discussing why certain isotope exchange reactions particularly those involving small ions occur at unexpectedly slow rates. Libby explained this phenomenon using the Franck–Condon principle, which states that because electrons move much faster than atomic nuclei, the nuclei (such as solvent molecules) do not have sufficient time to rearrange during the electron jump. For example, when Fe^{3+} is reduced to Fe^{2+}, the surrounding water molecules are

still oriented as if around the Fe^{3+} ion, creating an energetically unfavorable environment for the product. While Marcus acknowledged the general validity of Libby's interpretation, he considered it incomplete [8].

According to transition state theory, a chemical reaction proceeds along a potential energy surface that includes a transition state the point of highest energy between reactants and products. This concept was formalized by Eyring and Wigner through statistical mechanics and classical dynamics [9].However, Marcus argued that such a model is insufficient to describe bondless processes like outer-sphere electron transfer [8].

In outer-sphere electron transfer, no chemical bonds are formed or broken. Per the Franck–Condon principle, the nuclei remain in their original positions during the rapid electron jump. Marcus introduced a new perspective by recognizing that natural thermal fluctuations in the nuclear coordinates of the system,particularly the orientations of solvent molecules,can create a transient configuration that serves as a shared transition state for both reactants and products. If the system stochastically achieves a configuration that satisfies both the Franck–Condon principle and energy conservation, electron transfer can occur [8].

In this framework, the activation energy of the system corresponds to the energy required to achieve the necessary solvent reorganization termed the reorganization energy (λ). One of the most striking predictions of Marcus theory is the so called "inverted region", wherein increasing the driving force of the reaction (more negative ΔG°) actually slows down the electron transfer rate. This counter-intuitive phenomenon was experimentally confirmed in 1984 by Miller, Calcaterra, and Closs[10].

Marcus theory defines the rate constant of an electron transfer reaction as:

$$k = A \cdot \exp\left[\frac{-(\lambda + \Delta G^0)^2}{4\lambda k_B T}\right] \tag{1.1}$$

where:

- ΔG^0: Standard Gibbs free energy change of the reaction
- λ: Reorganization energy
- A: Pre-exponential factor
- k_B: Boltzmann constant
- T: Absolute temperature (K)

According to Marcus theory, as ΔG° becomes more negative i.e., as the reaction becomes increasingly exergonic the reaction rate eventually begins to decrease. This counter-intuitive prediction is a hallmark of the Marcus inverted region.

Another important mechanism for electron transport is the *quantum tunneling effect*. Ordinarily, electron transfer requires the electron to overcome an energy barrier, such as the activation energy or, as described in Marcus theory, the reorganization energy. However, due to the wave-like nature of matter, quantum tunneling enables the electron to pass through this barrier without acquiring the classical energy required to overcome it.

The probability of electron transfer via tunneling decreases exponentially with the increasing distance between the electron donor and acceptor. This distance dependence makes tunneling highly sensitive to molecular separation[11, p. 343].

The electron transfer rate k_{ET} depends on the donor–acceptor distance r as follows:

$$k_{ET} = k_0 \cdot e^{-\beta r} \tag{1.2}$$

where:

- k_{ET}: Electron transfer rate
- k_0: Rate constant at zero distance (i.e., direct contact)

- r: Donor–acceptor distance
- β: Electron tunneling attenuation coefficient (in units of Å^{-1})

In conclusion, when electron transport is considered within the framework of Marcus theory, the supply of reorganization energy is essential for electron transfer to occur. But in polymer-based systems immobilized on electrode surfaces, where does this reorganization energy come from? Particularly, we can identify three distinct regions: (1) the interface between the electrode surface (e.g., Fluorine-doped Tin Oxide (FTO)) and the polymer, (2) the bulk of the polymer itself, and (3) the interface between the polymer and the electrolyte. In the first case, since both the solid electrode interface and the polymer are physically immobile, reorganization energy may arise from the redistribution of charges within the polymer or the mobility of electrolyte ions and counterions that penetrate the polymer. This explanation can also be extended to the other two cases. However, it raises the question: Are different reorganization energies required for electron transfer across these three distinct interfacial regions? If so, which region demands higher reorganization energy, and which one is associated with slower electron transfer?

1.2 Electron Transfer in Multilayer Films

In the previous section, we attempted to relate monolayer electron transfer to established electron transfer theories. Briefly, in monolayer films, redox-active functional groups are initially adsorbed onto the electrode surface, and there exists a certain distance between them. The shorter this distance, the higher the probability of electron transfer via quantum tunneling. In self-assembled monolayers (SAMs), where redox-active groups such as ferrocene are immobilized on the surface through molecular bridges, the length of these bridges and any conformational changes during electron transfer directly influence the electron transfer rate [12].

On the other hand, in conductive polymer films such as PEDOT deposited onto the electrode surface, the structure is not as ordered as in SAMs. Here, electron transfer does not occur between specific redox-active functional groups but rather along the polymer backbone.

Now let us consider a multilayer system, where these chemical structures are not deposited as a single layer but rather as multiple stacked layers. In such a system, we examine the electron transfer mechanism.

To understand electron transfer in monolayer films on a macroscopic level, we refer to the model developed by Laviron in 1978 [13].In this study, Laviron introduced a voltammetric model suitable for thin-film electrode measurements, where classical diffusion-controlled models fall short. Since the redox molecules are surface-bound, the reaction is not diffusion-controlled; instead, kinetic processes are assumed to occur either at the surface or within the thin film layer.

Alternatively, in a study published in 1980 [14], a multilayer model was introduced. The primary difference between such multilayer systems and monolayers is that not all redox centers are in direct contact with the electrode. In the model, the polymer layers are divided into n segments and four assumptions are made:

1. The system is homogeneous,
2. The counter-ion transport is not limiting,
3. The counter-ion transport is faster than electron transfer,
4. There is no interaction between electrochemically active centers.

Electron transfer first occurs between the polymer layer adsorbed on the electrode and the electrode itself. Subsequently, electron transfer continues across the successive layers of the film.

In the first layer, the electrochemical reaction $O_1 + ne \rightleftharpoons R_1$ and the homogeneous electron exchange reaction:

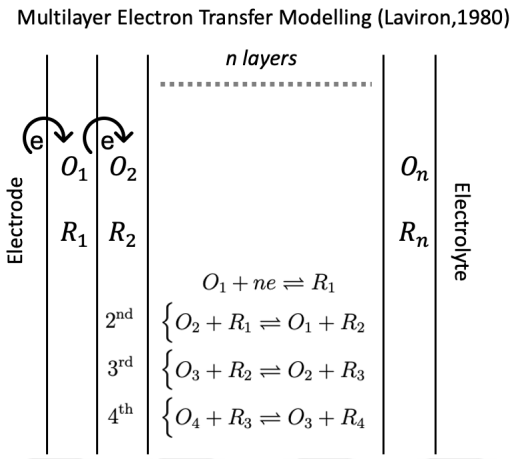

Figure 1.1: Electron transfer mechanism across multilayer redox films (redrawn and adapted).

$$O_2 + R_1 \rightleftharpoons O_1 + R_2$$

take place. In the following layers, we have the reactions [14]:

$$\begin{aligned}
2^{\text{nd}} \quad & \begin{cases} O_2 + R_1 \rightleftharpoons O_1 + R_2 \end{cases} \\
3^{\text{rd}} \quad & \begin{cases} O_3 + R_2 \rightleftharpoons O_2 + R_3 \end{cases} \\
4^{\text{th}} \quad & \begin{cases} O_4 + R_3 \rightleftharpoons O_3 + R_4 \end{cases} \\
& \vdots \\
(n-1)\text{th} \quad & \begin{cases} O_{n-1} + R_{n-2} \rightleftharpoons O_{n-2} + R_{n-1} \\ O_n + R_{n-1} \rightleftharpoons O_{n-1} + R_n \end{cases} \\
n\text{th} \quad & O_n + R_{n-1} \rightleftharpoons O_{n-1} + R_n
\end{aligned}$$

Laviron modeled the interlayer rate expression step-by-step using a propagation approach and drew an analogy with diffusion, where the behavior of electrons within the polymer was described by an effective diffusion coefficient [14].

In addition to Laviron's theoretical studies, experimental investigations have been conducted to examine the effect of electrode layer thickness on electron

transfer(ET)[15]. In one such study, redox active electrolyte solutions were deposited in very small volumes onto graphene and graphite electrodes using a micropipette, and the electron transfer rates were evaluated using cyclic voltammetry. Although no clear correlation was observed between the number of layers and the ET rate, it was concluded that the local surface conditions such as contamination and microscopic defects had a more pronounced effect on ET kinetics than the layer thickness itself.

In another study, the influence of thin metal phosphonate film thickness on the electron transfer rate between a gold electrode and either solution-phase or covalently bound redox molecules was investigated. Multilayer ZEDP (Zirconium 1,2-ethanediylbis(phosphonate)) films were adsorbed onto the gold electrode surface, and each layer was measured to have a thickness of approximately 8 Å via ellipsometry. It was found that the electron transfer rate decreased logarithmically with increasing ZEDP film thickness. Furthermore, the tunneling decay constant was determined to be $\beta \approx 0.43$ Å^{-1}, indicating that electrons likely tunnel through defect sites within the film rather than through a homogeneous medium, and that these defects limit the overall ET rate [16].

1.3 What Cyclic Voltammetry Reveals and Does Not Reveal About Different Charge Storage Mechanisms

Charge storage mechanisms can be classified into two main categories: Faradaic and non-Faradaic processes. In a Faradaic charge transfer mechanism, charge transfer occurs across the electrode–electrolyte interface, resulting in a change in the oxidation state of the material. In contrast, in non-Faradaic processes, the accumulation of counter charges occurs through the spatial arrangement of ions near the electrode surface, without any change in the oxidation state. In this section, examples of different Faradaic and non-Faradaic systems reported in the literature will be presented.[6, p. 17]

1.3.1 Faradaic Systems

Faradaic processes are fundamentally based on redox reactions. The oxidation states of the reactants involved in the reaction change because electron transfer occurs. Redox reactions form the basis of many energy storage systems. For example, the electrochemical intercalation mechanism has made the use of lithium-ion batteries widespread today [17]. What is important for intercalation is the intercalation materials. These materials are crystalline materials in which metal ions such as Li^+, Na^+, and K^+ can be reversibly inserted. The intercalation of ions is a Faradaic process. Examples of such materials include $LiCoO_2$ based on the Co^{3+}/Co^{4+} transition [18], $LiMn_2O_4$ operating through Mn^{3+}/Mn^{4+} redox reactions ([19]), $LiFePO_4$ working with the Fe^{2+}/Fe^{3+} redox couple [20], and 2D carbide and nitride-based materials such as $Ti_3C_2T_x$ [21].

In general, Faradaic processes exhibit some distinctive features when analyzed by cyclic voltammetry. For example, cathodic and anodic peaks, duck-shaped signatures due to diffusion limitations rather than rectangular shape, and peak current scaling with the square root of the sweep rate. However, the most distinctive feature is the overall shape of the voltammogram. These characteristics may not always be clearly visible in every electrochemical system involving Faradaic processes, and they may become more prominent or dominant depending on the environment. For instance, it has been reported that the $Ti_3C_2T_x$ material exhibits a rectangular shape in Li_2SO_4 medium, a rectangular shape with peaks in H_2SO_4 medium, and a diffusion-limited duck-shaped response in a $LiClO_4$/CAN medium [22]. In the same study, based on the CV shape, different charge storage mechanisms were classified as battery-type, pseudocapacitive-type, and electric double-layer-type.

1.3.2 Non-Faradaic Systems

In non-Faradaic processes, no electron transfer occurs; therefore, the oxidation states of electrochemically active species at the electrode surface remain unchanged. Instead, energy storage is achieved through the physical adsorption of ions onto the electrode surface a process known as electrosorption. Typical materials used in such systems include activated carbons, which possess high surface areas and porous structures [23], carbon nanotubes [24] and ordered mesoporous carbons, which feature tunable pore sizes optimized for ion diffusion and adsorption [25].

When double-layer capacitors are analyzed using cyclic voltammetry, they exhibit distinct electrochemical signatures, just like Faradaic systems. However, the voltammograms display a rectangular shape, with no distinct redox peaks as observed in Faradaic reactions. The observed current corresponds to capacitive charge accumulation, and it scales linearly with the scan rate [26].

Efforts are ongoing to better understand the charge storage mechanisms of non-Faradaic systems. To this end, in situ characterization and modeling techniques are employed to design supercapacitors capable of storing greater amounts of energy without sacrificing fast charge/discharge rates.

In one such study [27], nuclear magnetic resonance (NMR) was used for in situ characterization, and molecular dynamics simulations were performed. The results revealed that the electrode pores contain a significant number of ions even in the absence of an applied potential. Traditionally, it was believed that charge storage in these systems occurred solely through counter-ion adsorption. However, according to the findings of this study, the charging mechanism primarily proceeds via ion exchange. When a potential is applied to the electrode, co-ions are expelled from the pores and replaced by counter ions a process defined as ion exchange.

1.3.3 Pseudocapacitance

Conway further divided non-Faradaic accumulation into two subclasses: the double-layer capacitance and the newly introduced pseudocapacitance (which stems from redox reactions or adsorbed species), claiming that the latter type of material was first developed in his own laboratory [28].

According to the information reported in the 1990s [28], the idea of utilizing double-layer formation for electrical energy storage was first introduced by Becker and the Sohio group. They employed high-surface-area carbon powder materials together with tetraalkylammonium salt electrolytes. The carbon powders, which provided specific surface areas in the range of 100–2000 $m^2.g^{-1}$, enabled high capacitance densities of up to 250 $F.g^{-1}$. Since the charge storage mechanism in these systems relies on the physical separation of charged species (without involving chemical reactions), they exhibited high cycle stability, resulting in long operational lifetimes. The concept of pseudocapacitance was introduced later to describe systems in which electrochemical reactions contribute to charge transfer and storage.

When attempting to model double-layer capacitance using equivalent circuits, the simplest approach involves connecting a capacitor and a solution resistance in series. Although this model can adequately describe systems where no redox reactions occur within the applied potential range so-called 'ideally polarizable electrodes" it fails to accurately represent system behavior when Faradaic reactions are present, a situation Conway referred to as 'Faradaic leakage [28]." To address this limitation, Conway and his group proposed adding an adjustable Faradaic resistance into the equivalent circuit .

Later, Conway and his group introduced two distinct mechanisms to define capacitance within the system [28]. In some cases, the potential at which charge transfer occurs is directly dependent on the amount of charge accumulated on the electrode surface due to specific thermodynamic reasons. Under these conditions, capacitance can arise through two mechanisms:

- Redox reactions, where the electrode potential is a logarithmic function of the ratio of oxidized to reduced species activities.
- Surface adsorption processes, such as underpotential deposition (UPD), where a species (e.g., a metal ion) adsorbs onto the electrode surface at a potential more positive than its standard equilibrium potential.

It was proposed that pseudocapacitance arises during Faradaic charge transfer and leads to the passage of excess charge due to thermodynamic effects. An (ideally) constant electrode potential, such as that observed in a metal/metal-ion equilibrium, is maintained independently of the extent of the reaction. In contrast, processes associated with pseudocapacitance exhibit a dependence of the electrode potential on the amount of charge transferred [28].

To further explore this concept, it is instructive to consider a simple Nernstian system, such as the equilibrium between metallic silver (Ag) and its corresponding ion (Ag^+):

$$Ag^+(aq) + e^- \rightleftharpoons Ag(s) \qquad E^0 = 0.7989\,\mathrm{V\ vs.\ NHE} \tag{1.3}$$

The Nernst equation for this system is:

$$E = E^\circ + \frac{RT}{F} \ln\left(\gamma_{Ag^+}[Ag^+]\right) \tag{1.4}$$

As long as the ratio of ionic species remains constant, the electrode potential does not change, indicating dependence on ionic activity rather than on the amount of transferred charge.

In contrast, pseudocapacitive processes allow excess charge passage, and the electrode potential varies with the applied potential. Associated phenomena include:

- Underpotential deposition (UPD), such as the 2D deposition of hydrogen or copper onto platinum electrodes.

- Redox systems, where potential depends on the logarithm of the oxidant/reductant ratio.
- Chemisorption of anions with potential-dependent Faradaic charge transfer.

For example, in hydrogen sorption on Pt:

$$2H_2O + 2e^- \rightleftharpoons H_2 + 2OH^- \qquad E^0 = -0.829\,\text{V vs. NHE} \tag{1.5}$$

As the electrode potential becomes more negative, hydrogen atoms begin to adsorb on the electrode surface. Each adsorbed hydrogen atom corresponds to the transfer of one electron. To achieve full monolayer coverage ($\theta = 1$) on a smooth platinum (Pt) surface, a charge of approximately 210 mC/cm^2 is required [28].

Conway classified pseudocapacitance origins into three types [28]:

- Adsorption pseudocapacitance
- Redox pseudocapacitance
- Intercalation pseudocapacitance

These can produce capacitances 10–100 times greater than normal double-layer capacitance. For example:

$$C + e^- + H_2O \rightarrow CH + OH^- \tag{1.6}$$

For the above case the pseudocapacitance is given by:

$$C_\varphi = \sigma_H \frac{d\theta}{d\varphi} \tag{1.7}$$

- C_φ **($\mathbf{F/m^2}$):** Pseudocapacitance as a function of electrode potential.
- σ_H **($\mathbf{C/m^2}$):** The maximum surface charge density corresponding to full monolayer coverage of the active sites on the electrode surface.

- $\frac{d\theta}{d\varphi}$ **(V^{-1}):** The derivative of surface coverage with respect to electrode potential.

The equation that describes the potential-dependent surface coverage θ of redox or adsorbed species, assuming Langmuir-type adsorption behavior driven by the electrode potential φ.

$$\frac{\theta}{1-\theta} = K \exp\left(\frac{\varphi F}{RT}\right) \tag{1.8}$$

- θ**:** Fractional surface coverage.
- $1-\theta$**:** Fraction of unoccupied sites.
- K **(V^{-1}):** Adsorption equilibrium constant.
- φ **(V):** Electrode potential.
- F **(C/mol):** Faraday constant, $F = 96{,}485$ C/mol.
- R **(J/mol·K):** Universal gas constant, $R = 8.314$ J/mol·K.
- T **(K):** Absolute temperature.

Similarly, redox pseudocapacitance is defined as:

$$E = E^\circ + \frac{RT}{F} \ln\left(\frac{a(\mathrm{Fe}^{3+})}{a(\mathrm{Fe}^{2+})}\right) = E^\circ + \frac{RT}{F} \ln\left(\frac{\frac{Q(\mathrm{Fe}^{3+})}{Q}}{\frac{(1-Q)Q(\mathrm{Fe}^{2+})}{Q}}\right) \tag{1.9}$$

$$Q = Q(\mathrm{Fe}^{3+}) + Q(\mathrm{Fe}^{2+}) \tag{1.10}$$

- E° **(V):** Standard electrode potential of the redox couple.
- Q **(C):** Total Faradaic charge stored at the electrode.

- $a(Fe^{3+})$, $a(Fe^{2+})$: Activities of the oxidized and reduced species, respectively. These account for non-ideal solution behavior and are defined as $a = \gamma \cdot c$, where γ is the activity coefficient and c is the concentration [29, p. 239].

The Nernst equation for the Fe (III)/Fe (II) redox couple can be reformulated by substituting the activity terms with the corresponding transferred charge. When expressed in this manner, it reveals that the system, one-electron transfer, exhibits characteristics like electrosorption phenomena. This observation suggests that the redox process behaves analogously to an adsorption process, leading to the interpretation that a redox capacitance is formally analogous to an adsorption capacitance involving charge transfer.

Following Conway's definitions, these classifications have been widely adopted in the literature [28, 30, 31] to describe and characterize a variety of electrochemical systems.

On the other hand, Savéant examined the approach of Conway and his group to the concept of pseudocapacitance and emphasized that this concept is fundamentally incorrect, asserting that pseudocapacitors are, in fact, true capacitors [26].

To illustrate this assertion, cobalt oxide films have been examined by Savéant [26]. These films transition from an insulating state to an ohmic conducting state depending on the applied potential, during which a true electrical double layer is formed.

Double-layer capacitors, surface redox systems, and solution diffusion-controlled Faradaic systems can be distinguished from one another by analyzing their current–potential curves in cyclic voltammetry (CV) measurements [32].The voltammogram of a double-layer capacitor exhibits a rectangular shape, and the current is directly proportional to the scan rate. Surface redox systems display distinct oxidation and reduction peaks, which are mirror images of each other. In contrast, solution-phase redox systems also exhibit peaks; however, the peak current is proportional to the square root of the scan rate and is limited by diffusion.

Differentiating between Faradaic processes and double-layer charging based on their cyclic voltammetry signatures is generally straightforward. However, this clear distinction does not apply to pseudocapacitors and the concept of pseudocapacitance, as initially introduced by Conway et al., which involves redox processes that simultaneously exhibit a potentially varying capacitive signature [26].

Following the model proposed by Conway [28] and his group for the situations exemplified above, Savéant reconstructed corresponding formal capacitance versus electrode potential curves. For instance, this approach was applied to the case of hydrogen sorption.

The pseudocapacitance can also be described as:

$$\mathrm{H_3O^+} + M(1-\theta) + e^- \rightleftharpoons \mathrm{MH_{ads}}(\theta) + \mathrm{H_2O} \tag{1.11}$$

The oxidized species is $\mathrm{H_3O^+}$, and $C_{\mathrm{H^+}}$ denotes its concentration, while the reduced species is $\mathrm{MH_{ads}}$. The parameter θ represents the surface coverage of adsorbed hydrogen species.

Assuming the adsorption process obeys the Langmuir isotherm:

$$\frac{\theta}{1-\theta} = KC_{\mathrm{H^+}} \exp\left(\frac{VF}{RT}\right) \qquad \Rightarrow \qquad \theta = \frac{KC_{\mathrm{H^+}} \exp\left(\frac{VF}{RT}\right)}{1 + KC_{\mathrm{H^+}} \exp\left(\frac{VF}{RT}\right)} \tag{1.12}$$

Then the pseudocapacitance of the system is:

$$C_\varphi = q_1 \frac{d\theta}{dV} = \frac{q_1 F}{RT}\theta(1-\theta) = \frac{q_1 F}{RT} \cdot \frac{KC_{\mathrm{H^+}} \exp\left(\frac{VF}{RT}\right)}{\left(1 + KC_{\mathrm{H^+}} \exp\left(\frac{VF}{RT}\right)\right)^2} \tag{1.13}$$

When Savéant, following Conway's approach, reconstructed a capacitance versus electrode potential curve using this formulation, a peak-shaped curve was observed rather than the quasi-rectangular response expected from a precisely defined pseudocapacitive behavior. Moreover, upon examining the model proposed

for redox pseudocapacitance, Savéant found that it also produced a voltammogram characterized by diffusion-limited peaks, rather than exhibiting the quasi-rectangular shape typically associated with ideal pseudocapacitive behavior.

The fundamental question at the center of these discussions concerns the true nature of the materials used in supercapacitors. Specifically, it addresses the materials that Conway classified under "pseudocapacitance" materials whose charge storage originates from Faradaic processes yet exhibit the signature of double-layer charging, while Conway argued that they are not true capacitors in essence. In contrast, Savéant challenged the necessity of the pseudocapacitance concept altogether, asserting that these materials are, in fact, true capacitors. Although it is well established that these materials exhibit voltammograms distinctly different from those of purely Faradaic or purely double-layer mechanisms, the underlying mechanism remained in question. Savéant sought to clarify this by examining the case of cobalt oxide films as a representative example [26].

When examining the cyclic voltammograms of cobalt oxide films within the potential range of 0.59 V to 1.59 V, several distinct features are observed, which have been associated with the phenomenon referred to as pseudocapacitance. As the potential is swept from negative toward positive values, it is initially observed that the film behaves as an insulator, characterized by an absence of electrical conductivity and no measurable current. As the potential increases further into the positive range, the film transitions into a conductive state. At this stage, small peaks appear superimposed on the capacitive response, corresponding to surface proton-coupled Faradaic waves. The proton-coupled nature of these reactions is evident, as the height of the Faradaic peaks can be modulated by adjusting the pH of the electrolyte solution [26].

The quasi-rectangular shape of the voltammogram arises from the formation of a double-layer capacitor at the interface between the conductive solid film and the electrolyte, once the film reaches the conductive potential range. Another important observation is that varying the film thickness leads to changes in the measured capacitance. Under ideal conditions, increasing film thickness would not significantly impact the surface area, and thus the capacitance would

be expected to remain constant. However, the observed change in capacitance highlights the critical role of meso- to nanoscale structures in expanding the effective surface area of the metal oxide films, contributing substantially to their capacitive behavior.

Let us now examine how these meso- to nanoscale structures influence the transition of the film from an insulating to a conducting state, under which conditions charge storage occurs through redox processes versus double-layer formation, and how the changes observed in the voltammograms upon the removal of water from the metal oxide structure through annealing processes can be interpreted.

To describe the potentials within the system, three potentials are defined: φ_M, the galvani potential of the electrode; φ_S, the galvani potential of the solution; and φ, the potential of the cobaltate phase, associated with the nanoscale clusters. Cobalt nanoclusters are deposited onto the electrode surface, and phosphate ions from the electrolyte arrange themselves around these clusters. When the cobaltate phase is in its insulating state, the potential of the cobalt clusters equals that of the solution ($\varphi = \varphi_S$), and the hole density is zero. As the applied potential increases toward more positive values, a Faradaic current begins to flow, triggering chemical changes not only at the surface but also within the bulk of the cobalt oxide phase. This redox process results in an increase in the density of free charge carriers (electrons or holes) within the cobaltate phase. Consequently, the initially insulating cobaltate phase gradually transitions into a conducting state. As the potential continues to increase, the redox reactions become more active, leading to a further rise in the carrier density allowing the material to support electrical conduction. This process is referred to as the charging of the chemical capacitance of the film. During this transition, while the internal potential (φ) changes, the solution potential (φ_S) remains constant. Charge compensation during film oxidation modifies the overall charge distribution, resulting in the formation of an electrical potential gradient at the cobaltate/solution interface. This interface begins to behave as a double-layer capacitor, and the associated current exhibits capacitive characteristics. As a result, the system behaves as if two capacitors are connected in series. During a forward CV scan starting from

the insulating region, the current initially rises exponentially due to chemical capacitance charging. As the capacitance increases, the current stabilizes and the internal potential rises accordingly, with the film eventually behaving as an ohmic conductor [26].

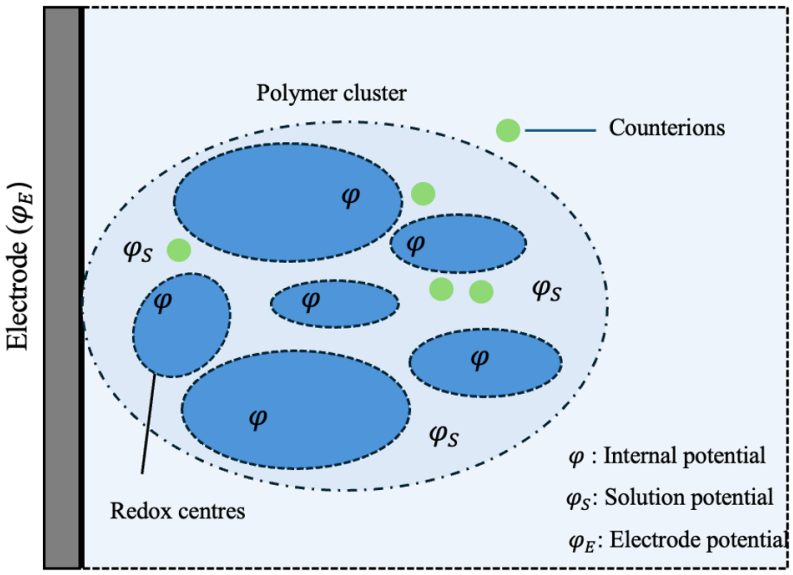

Figure 1.2: Schematic illustration of the polymer cluster model, adapted from the cobaltate phase description in [26], showing the transition from an insulating to a conducting state under applied bias.

Another prominent example of pseudocapacitive behavior is observed in ruthenium dioxide materials [26]. Interestingly, it has been found that the cyclic voltammograms of ruthenium electrodes subjected to thermal treatment differ from those of single crystal RuO_2 electrodes [26]. While single crystal RuO_2 electrodes exhibit a clear rectangular CV response, thermally treated electrodes display an ill-defined wave-like appearance [26]. After repeated cycling, ruthenized platinum electrodes eventually show a rectangular CV response in the anodic region, suggesting that interactions between redox centers and the continuous shift of the Ru standard potential under oxide coverage are responsible for the pseudocapacitive behavior observed in transition metal oxides. Later investigations proposed that these differences stem from variations in the electrode surface

structure, which were explored using atomic pair-density function analysis [26]. It was revealed that hydrated ruthenium oxide ($RuO_2 \cdot xH_2O$) forms nanocrystals or clusters (1.2–2 nm) chemisorbed and physisorbed with water molecules on the electrode surface, and that electronic conductivity is maintained through pathways between these nanocrystals. This model supports the idea that pseudocapacitors are, in fact, true capacitors [26].

The distinct Faradaic waves observed in thermally treated electrodes are explained by the absence of sufficient water molecules to bridge the nanoclusters, forcing electron transfer via a Faradaic hopping mechanism. A similar behavior has been reported for WO_3 films [26], where anhydrous WO_3 exhibits a peak-shaped Faradaic CV response, whereas hydrous WO_3 shows a capacitive-like response accompanied by an insulator-to-conductor transition, as previously described for cobalt oxide films. Small-angle X-ray scattering studies [26] further confirmed that before annealing, RuO_2 exists as 0.7 nm-sized nanoclusters dispersed within a large amount of confined water. After annealing, these nanoclusters aggregate into larger RuO_2 particles, resulting in a reduction of surface area and a corresponding decrease in capacitance. After the formation of a conductive network, the surface area of the resulting RuO_2 aggregates determines the capacitance, with the Ru^{4+}/Ru^{3+} redox processes localized at the outermost regions of these aggregates. It has also been observed that three types of currents contribute to the CV signal: double-layer charging within pores, reversible ion-specific electrosorption, and irreversible redox processes such as hydrogen or oxygen evolution.

Moreover, in the case of MnO_2 [26], it has been shown that the theoretical maximum charge based on the Mn^{4+}/Mn^{3+} redox transition (1110 C/g) can be reached—or even exceeded—without exhibiting clear Faradaic features in the CV response. This observation further challenges the strict validity of the pseudocapacitance concept as it was originally defined.

1.3.4 b-value Analysis

As the discovery of unconventional materials rapidly progresses, researchers have also sought to understand the underlying mechanisms by developing analytical approaches using conventional electrochemical techniques. Among these approaches, the so called *b-value analysis* has emerged as a tool.[33, 34] This method aims to distinguish the dominant physical processes governing an electrochemical system. [35]

As previously discussed, in purely Faradaic systems where redox processes dominate, if the system is limited by diffusion at its maximum rate, the relationship between the scan rate (ν) and the peak current (i_p) becomes proportional to the square root of the scan rate. This diffusion-controlled behavior results in a linear relationship between $\log(i_p)$ and $\log(\nu)$ with a slope (b-value) of approximately 0.5 [36].

$$i_p = 0.4463 \left(\frac{F^3}{RT}\right)^{1/2} n^{3/2} A D^{1/2} C^* \nu^{1/2} \tag{1.14}$$

where:

- i_p is the peak current (A),
- F is the Faraday constant (96,485 C/mol),
- R is the universal gas constant (8.314 J/(mol $\cdot$ K)),
- T is the temperature (K),
- n is the number of electrons transferred,
- A is the electrode surface area (cm^2),
- D is the diffusion coefficient (cm^2/s),
- C^* is the bulk concentration of the electrochemically active species (mol/cm^3),

- ν is the scan rate (V/s).

On the other hand, if the system is not limited by diffusion for instance, in cases where the electrochemically active species are adsorbed onto the electrode surface the observed peak current becomes linearly proportional to the scan rate itself. This behavior is typical for surface-confined redox systems and leads to a b-value of approximately 1.0 in the $\log(i_p)$ vs. $\log(\nu)$ plot.For systems where the electrochemically active species are adsorbed on the electrode surface, the peak current (i_p) shows a linear dependence on the scan rate (ν), and is described by the following equation: [13]

$$i_p = \frac{n^2 F^2}{4RT} \nu A \eta_0^* \tag{1.15}$$

where:

- i_p is the peak current (A),
- n is the number of electrons transferred in the redox reaction (dimensionless),
- F is the Faraday constant, $F = 96\,485\,\mathrm{C/mol}$,
- R is the universal gas constant, $R = 8.314\,\mathrm{J/mol \cdot K}$,
- T is the absolute temperature (K),
- ν is the scan rate (V/s),
- A is the electrochemically active surface area of the electrode (cm^2),
- η_0^* is the effective surface concentration of the redox-active species ($\mathrm{mol/cm}^2$).

This equation applies to surface-controlled processes where electron transfer is not limited by diffusion, as in the case of monolayers, which are essentially diffusionless systems.

The overall b-value is obtained as the slope of the line where the y-axis represents the logarithm of the peak current and the x-axis represents the logarithm of the sweep rate [37]:

$$i = a\nu^b \tag{1.16}$$

- i: Current
- ν: Scan rate
- a, b: Constants

In some experimental studies, the b-value has been observed to lie between 0.5 and 1 [38]. Conway *et al.* attributed this behavior to the overall electrochemical response arising from the simultaneous contribution of a surface-controlled process and a semi-infinite diffusion process governed by mass transport [39].

$$i(V) = k_1\nu + k_2\nu^{1/2} \tag{1.17}$$

Recent studies on b-value analysis have explored how this parameter can vary across electrochemical systems with different characteristics, using both numerical and simulation-based approaches[38]. These methods delve into the intricacies of b-value analysis. A key finding is that the b-value is not constant. Although typically a single b-value is assigned across the entire scan rate range, in reality, the b-value is not fixed. Therefore, making kinetic interpretations based on a single b-value may be oversimplified. To address this, Stek and colleagues developed a method that assigns b-values to specific scan rates instead of over an entire range. This method requires taking the derivative of experimental $\log(i_p)$ data with respect to $\log(\nu)$ across a range of scan rates that are evenly spaced on a logarithmic scale [40].

This approach was applied to Nb_2O_5 thin films of varying thicknesses [38], demonstrating that the b-value can vary between 0.5 and 1. Film thickness was

non-dimensionalized for analysis, using an approximate diffusion coefficient of 6×10^{-11} cm^2 s^{-1}. When film thickness (L), scan rate (ν), and diffusion coefficient (D) are known, b-values can be expressed as a function of X (the dimensionless thickness), forming a characteristic curve.

Instead of analyzing the b-value individually for each system, a generalized curve can be used to interpret kinetic behavior. This allows for consistent comparison across different experiments, since systems with varying film thickness, diffusion coefficient, and scan rate exhibit similar behavior when the dimensionless parameter X is held constant. As a result, this approach facilitates the optimization of design parameters for ion-insertion electrode systems.

The observation of b-values lower than 0.5 has raised questions, as such values deviate from classical diffusion-controlled expectations [41]. Although bi-directional diffusion occurs during the reverse sweep in many electrochemical systems, it is not solely responsible for $b < 0.5$ behavior. In classical Nernstian diffusion at ion-blocking electrodes, bi-directional diffusion in a semi-infinite medium does not lead to b-values below 0.5. Therefore, the emergence of $b < 0.5$ is attributed to bi-directional diffusion occurring within a finite geometry, where the film thickness is limited and the concentration profile remains unequilibrated during the potential sweep. In such cases, a localized concentration pocket can develop, resulting in simultaneous diffusion toward both the surface and the bulk of the film, thereby reducing the overall current response. However, when the dimensionless thickness parameter X becomes sufficiently large due to faster diffusion, higher scan rates, or thicker films the system approaches semi-infinite diffusion behavior, and the b-value converges back to 0.5. This indicates that $b < 0.5$ is a transient feature arising from finite size effects under kinetically constrained conditions.

1.3.4.1 Limitations of b-value Analysis

As briefly mentioned in the previous section, b-value analysis has several limitations and is not sufficient on its own to fully characterize an electrochemical

system. First, the empirical relation $i_p \propto \nu^b$ assumes a universal power-law behavior, which may not hold true for all kinetic regimes or across a wide range of scan rates [42].Similarly, assigning a constant b-value to the entire scan rate range overlooks dynamic changes in transport limitations and transitions between surface and diffusion-controlled regimes. Moreover, both experimental and simulation data have shown that b-values vary with scan rate, film thickness, and diffusivity, particularly in thin-film or nanostructured electrodes.

Additionally, finite film geometry can lead to distorted concentration profiles and bi-directional diffusion, which may result in b-values lower than 0.5 values that cannot be explained by classical theory. Ohmic drop [43], charge transfer resistance, and instrumental limitations (e.g., iR compensation) [44] can also distort the current response, especially at high scan rates. The slope of $\log(i_p)$ vs. $\log(\nu)$ plots is influenced by the number and spacing of the scan rates; poorly selected ranges can yield misleading b-values. Furthermore, similar b-values may result from fundamentally different mechanisms (e.g., capacitive-like versus diffusion-limited processes), leading to non-unique or ambiguous mechanistic interpretations.

For instance, experimental data from Li^+ intercalation processes show that b-values are not constant across varying scan rates, and instead two distinct kinetic regions are observed: between 0.1 and 20 mV s^{-1}, $b \approx 1$, while above 50 mV s^{-1}, b decreases to approximately 0.8–0.7 [45]. This demonstrates that kinetic characterization using a single b-value may be overly simplistic. At higher scan rates (e.g., 50 mV s^{-1}), both ohmic losses and diffusion limitations become significant, resulting in a reduction of b. This decrease is not only due to diffusion limitations, but also due to resistive contributions from the active material and Solid Electrolyte Interphase (SEI) layer. Therefore, the b-value depends not only on the reaction mechanism but also on the device architecture.

Moreover, because intercalation can produce b-values close to 1, similar to classical surface redox capacitance, a b-value of 1 does not necessarily indicate a surface-controlled mechanism. This further underscores that b-value analysis alone may not be sufficient to accurately distinguish between different charge

storage mechanisms.

Furthermore, in the cyclic voltammograms of certain materials, it is not always possible to distinguish a clear peak current due to the broad nature of the current response [46]. In such cases, the peak current or currents cannot be easily identified. This is particularly relevant for materials with non-constant capacitance values [47], where the system behaves as an insulator below a certain potential and becomes conductive upon electrochemical doping. In these materials, both conductivity and capacitance are intricately dependent on the doping level. Therefore, it would not be inaccurate to state that b-value analysis alone is insufficient for elucidating the dominant charge storage mechanisms in such systems with complex electrochemical behavior.

1.4 Materials Under the Scope: Conjugated Polymers (CPs) and their Oligomers

Before discussing polymers in detail, we begin with the simplest monomeric unit of PEDOT, which is the subject of this study: EDOT. 3,4-Ethylenedioxythiophene is an organosulfur compound. Structurally, it features a thiophene ring substituted at the 3 and 4 positions with an ethylenedioxy group.EDOT exhibits electropolymerization behavior under oxidative potentials. Initially, polymer formation was explained by a classical radical polymerization mechanism in which the propagation of the polymer chain proceeds via the formation of monomeric radical cations, which subsequently couple with a growing chain [48]. However, as experimental findings challenged this classical view, Heinze and Savéant [49] demonstrated the involvement of a comproportionation reaction in the mechanism. In this mechanism, highly charged oligomeric cations interact with neutral monomers to generate new radical cations, thereby accelerating the oxidation of the monomer. This process is referred to as redox catalysis and is now widely accepted as a general mechanism for electropolymerization in many systems.

A study tracking polymer growth using spectroelectrochemistry revealed that electropolymerization does not merely involve a simple surface deposition but begins with the formation of active oligomeric precursors in solution. These oligomers are crucial in both nucleation and chain growth processes. The study also highlights how parameters such as the applied potential and electrode-film interactions shape this process. [50]

Investigating the electrochemical properties of the EDOT monomer and its oligomers, such as oxidation potential and electron transfer kinetics, is challenging. This is because it requires the isolation of a single EDOT monomer; otherwise, electrochemical experiments lead to rapid polymerization, and the resulting voltammograms reflect not only monomer oxidation but also the growth of the polymer.

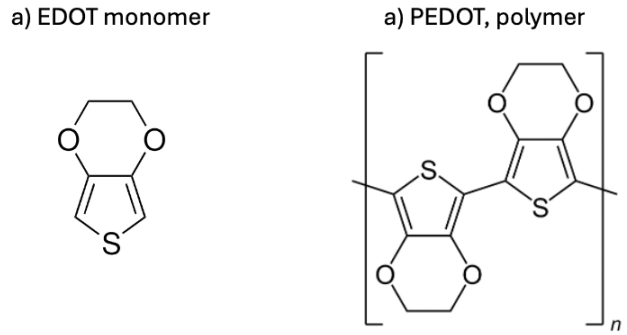

Figure 1.3: (a) Chemical structure of EDOT monomer. (b) Corresponding PEDOT polymer structure obtained afterpolymerization of EDOT.

On the other hand, PEDOT, the polymer form of EDOT, is one of the most extensively studied conducting polymers [48] due to its electrochemical stability. The chemical structures of EDOT and PEDOT are shown in Fig. 1.3. As a polymer chain, PEDOT exhibits a less poitive potential compared to its oligomers[48]. A study on polypyrrole films found that while the films became redox active at relatively less positive, the corresponding monomer (pyrrole) exhibited a more positive potential.

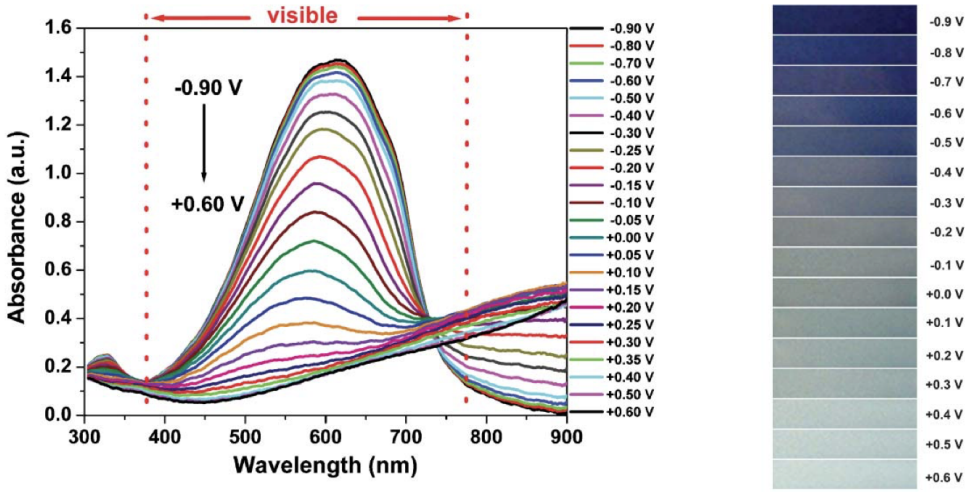

Figure 1.4: Electrochemically induced optical absorption spectra of the conducting polymer, PEDOT, film recorded between 300–900 nm at applied potentials ranging from −0.90 V to +0.60 V (vs. reference electrode). The absorption peak in the visible region decreases upon oxidation, corresponding to the color change shown on the right side from deep blue at −0.90 V to a more transparent state at +0.60 V. Reproduced with permission from [51]. Copyright 2005, Royal Society of Chemistry.

The transition from monomers and short chain oligomers to fully conjugated conducting polymers results in a progressive increase in π-electron delocalization, which significantly influences the optical absorption spectra and the redox potentials of the material.Figure 1.4 shows the electrochemically induced optical absorption spectra of a PEDOT film (300–900 nm), where oxidation leads to a decrease in the visible absorption peak accompanied by a color change from deep blue (–0.90 V) to a more transparent state (+0.60 V).The morphology of electrogenerated polymer films whether compact or porous plays a critical role in determining their electrochemical properties, particularly in terms of ionic accessibility and charge storage capacity.

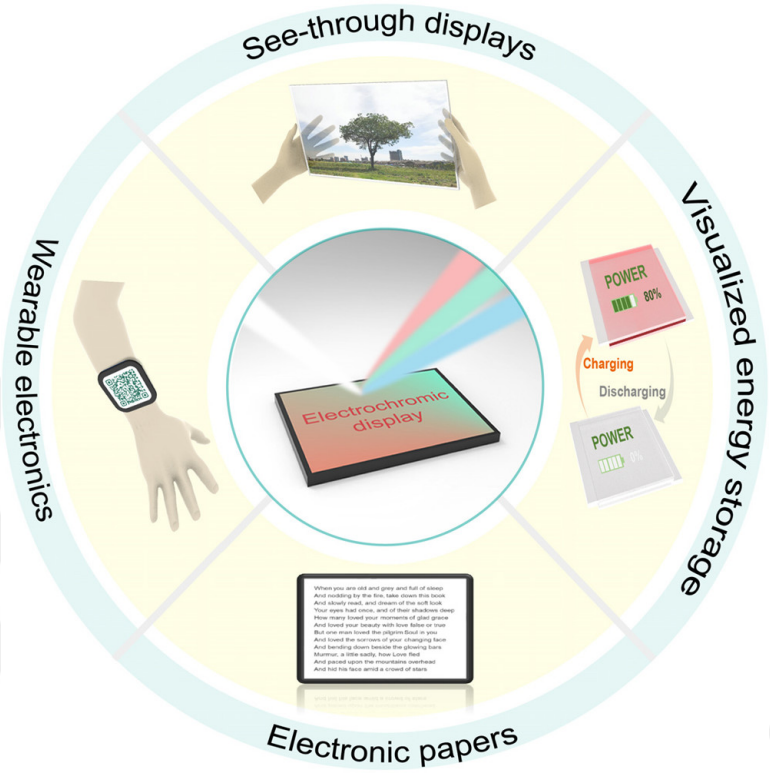

Figure 1.5: Schematic illustration of potential applications of electrochromic devices, including see-through displays, visualized energy storage, wearable electronics, and electronic papers. Reproduced from [52], licensed under CC BY 4.0.

Conducting polymer films, such as PEDOT, exhibit reversible color changes upon doping and dedoping. This optical behavior can be quantitatively tracked using UV-Vis spectroelectrochemistry and is highly relevant for applications in electrochromic devices. Figure 1.5 schematically illustrates the potential applications of electrochromic devices, such as see-through displays, visualized energy storage, wearable electronics, and electronic papers. One of the primary advantages of conducting polymers lies in their excellent redox reversibility, making them ideal candidates for long term electrochemical cycling and energy-related applications [53].

1.5 Proposed Charge Transfer Mechanism of CPs

Conducting polymers are conjugated organic molecules. Since both electronic and ionic conduction occur simultaneously, they are often referred to as mixed electronic–ionic conductors. They exhibit electrochemically active properties, meaning that depending on the applied potential, electrons or holes can be injected into the polymer, thereby increasing its conductivity.

Scientists have described the charge carriers in these materials as solitons, polarons, and bipolarons, which are defined as delocalized defects along the polymer backbone [54].

In a conducting polymer matrix, macroscopic charge transport is known to result from the coupling of multiple mechanisms. Electron motion occurs along the conjugated backbone, through interchain electron transport, and is strongly influenced by the film morphology of the polymer. Along a single chain, electrons can move via the delocalized π-orbital system. Depending on the distance between polymer chains, different types of interchain tunneling can occur. Finally, on a larger scale, if the polymer forms fibrillar structures, charge transport can proceed within individual fibers as well as between neighboring fibers [55].

The redox transition resembles a phase transition, where an insulating polymer becomes suddenly conductive upon application of an external potential. During this process, the polymer forms a biphasic system in which only part of the material is conductive. Electrical conductivity depends on the formation of a continuous pathway through connected conductive domains. When the conductive phase reaches a critical density, the overall conductivity of the system increases significantly a phenomenon that can be explained by percolation theory [55].

The dopant A binds to an available binding site S to form the complex AS: Dopant A binds with S, which has an empty binding site, to form the AS complex:

$$A + S \underset{k_r}{\overset{k_f}{\rightleftharpoons}} AS \tag{1.18}$$

Where:

- $k_f \rightarrow$ Association rate
- $k_r \rightarrow$ Ddissociation rate
- $K = \dfrac{k_f}{k_r} \rightarrow$ **Equilibrium constant**, indicates the binding affinity

A comprehensive solution and interpretation of this problem was presented by Gardner and Bartlett [56]. Dopant transport is inherently a nonlinear and time-dependent process that involves both diffusion and binding reactions. The study by Gardner and Bartlett provides a mathematical framework by non-dimensionalizing the governing equations and analyzing the system under various limiting cases [56].

According to their findings:

- When the film is **unsaturated**, the reaction is **fast**, and the number of binding sites is **low**, **diffusion dominates**.
- When the film is saturated and the reaction is fast with minimal dopant binding, diffusion remains unaffected.
- When the film is **unsaturated** and the reaction is **slow**, **diffusion occurs first**, followed by **homogeneous binding**.

These results demonstrate that the interplay between dopant diffusion and reaction kinetics in a polymer matrix can lead to complex transport behavior, which must be carefully analyzed for accurate modeling.

Alongside this theory, a comparable framework has been proposed to describe the charge carrier mechanism in semiconducting polymers. In this model, the primary charge carriers are **polarons** and **bipolarons** [57, 58].

The mechanism proceeds as follows:

- The **neutral polymer** possesses fully occupied valence bands and empty conduction bands, separated by an energy gap.
- **First oxidation** introduces a **polaron** state within the middle of the band gap.
- **Second oxidation** leads to the formation of a **bipolaron**, resulting in deeper localized defect states.
- With **further doping**, these bipolaron states broaden into **bipolaron bands**, which significantly contribute to electrical conductivity via **bipolaron hopping**.

Electrical conductivity in conducting polymers cannot be explained by a single transport mechanism. Both *intrachain* (along the polymer backbone) and *interchain* (between adjacent chains) transport processes contribute to the overall conductivity.

1.6 Electrochromism

Electrochromism refers to materials that exhibit a reversible change in color upon the application of an external potential [59]. These materials can accept or donate electrons depending on the applied potential, resulting in a change in the number of electrons in the system. This difference in the electronic structure between the initial and final states can lead to distinct spectroscopic transitions between energy levels, as the two states correspond to different electron configurations. As a consequence of these differing transitions and the associated energy differences between electronic states, the wavelength of light absorbed by the material changes, which in turn alters its perceived color [60].

Electrochromic materials can be either inorganic or organic. For instance, tungsten trioxide (WO_3) is an intercalation-type redox material that appears

bleached in its reduced form and colored in its oxidized state [61]. On the organic side, the conductive polymer PEDOT is a well-known example of an electrochromic material [62].

In electrochemical systems involving electrochromic materials, if the electron transfer is fast, the rate of color formation is limited by mass transport processes [60]. Moreover, the amount of color formed over a given time is directly linked to the rate of charge passage through the electrode. The coloration rate is proportional to the electron uptake, described by $I = \frac{dQ}{dt}$, and since absorbance (Abs) is proportional to the charge (Q), the rate of absorbance change ($\frac{d(\text{Abs})}{dt}$) follows the Cottrell $t^{-1/2}$ dependence. Upon integration, this results in Abs $\propto t^{1/2}$, which has been experimentally confirmed by the linear behavior of current (I) with respect to $t^{-1/2}$ in aqueous systems [63].

Electrochromic materials may also be deposited in solid form onto electrode surfaces, such as tungsten dioxide thin films. In such architectures, the diffusion coefficient of ions into the solid electrochemically active matrix becomes a critical factor. To achieve fast electrochromic response, the ions must migrate rapidly; thus, small ions are often preferred to minimize the response time[64].

The structure of the electrochromic material, whether amorphous or crystalline, also affects ion diffusion. It has been found that ions diffuse more rapidly in amorphous oxides compared to their crystalline counterparts [60].

The influence of film thickness on the diffusion time can be estimated using Fick's second law, which predicts that diffusion time is proportional to the square of the film thickness and inversely proportional to the diffusion coefficient [65].

The average diffusion time is given by:

$$\tau_D = \frac{d^2}{4D} \tag{1.19}$$

where:

- τ_D: Diffusion time,
- d: Film thickness,
- D: Diffusion coefficient (m^2/s).

The characteristic diffusion time can be estimated from the root-mean-square displacement relation $\langle r^2 \rangle = 2nDt$ (with $n = 2$ for planar geometry), by taking the film's characteristic distance as $d/\sqrt{2}$, which yields $\tau_D \approx d^2/(4D)$ as an order-of-magnitude timescale.

As expected, the absorbance of WO_3 films increases with the insertion coefficient(x), but deviates from Beer's law at high values of x or total charge Q.

PEDOT is an electrochromic material, and the electronic transition responsible for its absorbance change is attributed to a π–π^* interband transition. In its neutral state, PEDOT exhibits a deep blue color, which shifts to light blue upon oxidation[66].

The electrochromic properties of thiophene-based conductive polymers can be finely tuned through small modifications in the monomer structure. The position of methyl groups [67], as well as the inter-ring dihedral angle, significantly influence the conjugation length and therefore the color[68].

1.7 Color Switching in Electrochemical Cells and Limitations: Electron vs Ion Transportation

Electrochromic materials, which possess color switching mechanisms, are key components of electro-optic devices. These devices can reversibly modulate their optical properties such as light transmittance, reflectance, and color through ion migration triggered by an applied voltage. Owing to their low energy consumption

and high color contrast, electrochromic systems are actively being investigated for applications in photothermal modulation, dynamic displays, and camouflage technologies.

Among the various performance parameters of electrochromic (EC) materials, the switching time (i.e., the time required for color change) is one of the most critical for practical applications. This parameter is especially vital in systems that demand rapid response, such as smart windows and real-time display technologies[69].

These systems are typically optimized through three fundamental layers[69]. First, enhancing electron transport is achieved by selecting electrode materials with high conductivity and smooth surface morphology. Second, porous and thin films are developed to facilitate ion diffusion. Lastly, efficient ion migration is targeted by tuning parameters such as ion type and electrolyte viscosity, choosing high-mobility species like multivalent ions or proton carriers, or adopting hybrid ion strategies.

Overall, the optimization strategies primarily focus on accelerating the diffusion of migrating ions and improving ion adsorption on the surface of the electrochromic material [69].

Recent studies have shown that the structural properties of electrochromic materials play a crucial role, and even a dual-electrochromism mechanism is possible. This means that the optical response can be modulated not only in the UV–Vis region but also in regions such as the near-infrared (NIR) [70, 71].

$WO_3 \cdot H_2O$, unlike conventional WO_3, is a dual-band electrochromic material capable of independently modulating both visible and NIR light[72]. The structural water within the $WO_3 \cdot H_2O$ lattice enhances crystal permeability, allowing faster diffusion of Li^+ ions. This results in a significantly improved switching speed (i.e., coloring and bleaching time) compared to anhydrous WO The more open structure facilitated by the structural water enables faster ion insertion and extraction, leading to a rapid electrochromic response [72].

1.7.1 Ion coupled electron transfer

As discussed in earlier sections, electron transfer occurring at conducting polymer film electrodes requires the insertion or extraction of counter-ions from the electrolyte into the polymer matrix to maintain charge neutrality. This ion exchange process commonly referred to as electrochemical doping and dedoping is fundamental to the redox behavior of mixed ionic–electronic conductors such as PEDOT:PSS systems that exhibit ion dependence can be found in various contexts, and when the ion in question is a proton, the process occupies a special position as proton-coupled electron transfer (PCET). The coupling between proton and electron transfer imparts significant mechanistic diversity, encompassing both sequential and concerted pathways [73].

A recent *operando* study [74] utilizing ^{23}Na and ^{1}H NMR spectroscopy has provided quantitative insights into this process by tracking the movement of Na^+ ions and water molecules during the electrochemical cycling of PEDOT:PSS films. PEDOT:PSS, an intrinsically doped p-type semiconductor, contains holes on the PEDOT backbone that are compensated by sulfonate anions on the PSS chains. This charge compensation leads to strong Coulombic interactions and intimate mixing of PEDOT and PSS in PEDOT-rich domains. Due to the typically excess PSS content in these films, many sulfonate groups are also neutralized by external cations such as Na^+ or H^+.

Upon electrochemical dedoping, holes are removed from the PEDOT chains, resulting in unbound SO_3^- groups that attract cations from the electrolyte. Reversing the potential leads to re-injection of holes and removal of cations, effectively redoping the polymer [74].

In the aforementioned NMR study, a characteristic ^{23}Na quadrupolar splitting was observed, attributed to the partial ordering of the PSS chains within PEDOT-rich domains. Importantly, the magnitude of this quadrupolar splitting decreased with increasing hole concentration on PEDOT, reflecting the expulsion of Na^+ ions from the ordered regions. A nearly 1:1 coupling efficiency between holes and Na^+ ions was reported when using a 1 M NaCl electrolyte, indicating that Na^+

ions serve as the primary charge-compensating species under these conditions. This finding provides compelling evidence for a direct correlation between ionic motion and electronic charge modulation in PEDOT:PSS, and highlights the utility of *operando* NMR spectroscopy for probing structure–function relationships in electrochemically active polymer systems [74].

1.7.2 Ion-Free Charge Transfer Possibility in Conjugated Polymers

Conjugated polymers provide a favorable environment for electron delocalization along the molecular backbone. However, due to their typically amorphous or semi-crystalline morphology, structural disorder, and weak interchain coupling, charge carriers such as polarons and bipolarons tend to become localized. While disorder leads to electronic localization, Coulomb interactions still correlate carrier motion. These Coulombic forces play a significant role in electronic transport and, as described in condensed matter physics, give rise to what is known as a *soft Coulomb gap*.

The soft Coulomb gap appears in systems where electrons are both localized and interacting. It refers to a suppression but not a complete vanishing of the density of states (DOS) near the Fermi level, meaning that the number of accessible electronic states near this energy is reduced [75].The Fermi energy represents the highest occupied energy level at absolute zero temperature.

In a recent study utilizing organic electrochemical transistors (OECTs), extreme band filling was achieved. In molecular materials, bands are typically described using HOMO and LUMO levels. Under standard doping conditions, p-type doping involves the removal of electrons from the HOMO, while n-type doping adds electrons to the LUMO. However, under extreme band filling conditions, once the HOMO (or LUMO) is fully emptied (or filled), doping can continue into deeper (or higher) energy levels such as HOMO-1 or LUMO$+1$. This can result in a modified electronic structure and affect the conductivity, but it may

also lead to structural degradation of the polymer [76].

This regime allows researchers to explore new conduction mechanisms, such as the formation of a Coulomb gap, beyond the conventional band model. A novel double-gating technique [76] has been used to investigate these phenomena. This approach combines a chemical gate (ion gate, V_{IG}) to control bulk doping and a field-effect gate (V_{FG}) to inject additional carriers locally, without introducing new ions.

To decouple ionic motion from carrier injection, the system is cooled below the glass transition temperature ($\sim$ 200 K) while V_{IG} is applied. This freezes the ionic configuration. Subsequently, V_{FG} is applied independently to modulate electronic properties without ionic compensation, enabling the study of non-equilibrium electronic transport and changes in the DOS, including the formation of a Coulomb gap [76].

At room temperature, ionic motion is fast, and the system can equilibrate with changes in V_{FG}. However, below $\sim$ 240 K, translational ionic motion slows significantly due to its high activation energy, eventually becoming frozen. This was confirmed using ^{19}F Nuclear Magnetic Resonance (NMR), which revealed two distinct modes of ionic motion: fast intra-ionic movements (e.g., rotation of functional groups) with low activation energy, and slow translational motion of ions like the counter-anion TFSI^- within the polymer matrix, with much higher activation energy.[76]

Even when ions are frozen, electrons can still move within the polymer network. However, this motion occurs in a pre-set, frozen ionic landscape resulting in a non-equilibrium state. As a consequence, nonlinear and symmetric features were observed in the transistor transfer characteristics (current vs. gate voltage), indicating ambipolar transport behavior. In ambipolar systems, both electrons and holes contribute to charge transport, in contrast to conventional n-type or p-type devices, which typically favor only one type of carrier[76].

1.8 Dual Charge Transfer Nature of CPs: Faradaic and Capacitive Charge Accumulation

In electrochemical systems, charge storage and transfer processes are governed by both diffusion-controlled mass transport and interfacial phenomena at the electrode/electrolyte boundary. The diffusion layer defines how electrochemically active species migrate to and from the electrode surface, shaping the time-dependent current response, while the electrical double layer describes how charges are organized at the interface, giving rise to capacitive contributions. Together, these two concepts form the fundamental basis for understanding the dual charge-transfer nature of conducting polymers, where Faradaic processes driven by redox reactions coexist with capacitive charge accumulation associated with double-layer formation. In this section, a brief introduction is therefore provided to the two fundamental layers underlying these storage mechanisms: the diffusion layer, which governs mass transport, and the electrical double layer, which governs double-layer charging.

1.8.1 Diffusion Layer

In electrochemical systems, the current generated in response to an applied potential cannot be explained solely by the magnitude of the applied potential. If the species involved are particles that move freely in solution, the current arising from electrochemical redox processes depends collectively on the diffusion and migration of electrochemically active molecules, the applied potential at the electrode, and the rate of electron transfer between electrochemically active species.

As soon as the potential is applied to the electrode, species located near the electrode surface undergo oxidation or reduction, depending on the applied potential. Since this transformation is typically Nernstian and rapid, the concentrations of reduced and oxidized molecules near the electrode change quickly. For

example, when a sufficiently positive (oxidative) potential is applied, all nearby reduced species are converted into oxidized ones, and the concentration of reduced species near the electrode surface (C_R) effectively becomes zero.

To sustain the electrode reaction, the reactant species must reach the electrode surface, and the products must be transported away from it. Driven by the resulting concentration gradient, species diffuse from regions of higher concentration to regions of lower concentration. This mass transport leads to the formation of a **diffusion layer**.

The diffusion layer is a region extending from the electrode surface into the bulk solution, where species are transported solely by diffusion. It typically spans a few micrometers in thickness, and within this region, the concentration profiles of the species are dynamic.

One of the parameters that significantly influences the diffusion layer in electrochemical experiments is **time**. As time progresses, the diffusion layer expands. This expansion is governed by the diffusion coefficient, D. In long-duration experiments, the continual growth of the diffusion layer can become a limiting factor for the current.

$$\delta \approx \sqrt{2Dt} \tag{1.20}$$

where:

- δ : Thickness of the diffusion layer
- D : Diffusion coefficient of the species
- t : Time elapsed since the start of the diffusion process

As derived by Einstein (1905) and later presented in its English translation [77], one obtains $\langle x^2 \rangle = 2Dt$.(The square root of the arithmetic mean of the squares of displacements in the direction of the X-axis)

The diffusion coefficient of the species is of great importance, as it directly relates to the mobility of electrochemically active species within the solution. Species with higher diffusion coefficients exhibit faster propagation and consequently form thicker diffusion layers. The geometry of the electrode directly affects the thickness, direction, and rate of diffusion.

Whether the applied potential determines the thickness of the diffusion layer depends on the reversibility of the reaction. In quasi-reversible or irreversible systems, the diffusion layer thickness can be influenced by the potential, whereas in fully reversible systems, changes in applied potential do not significantly affect the diffusion layer [78].

In addition, factors such as convective flow, stirring of the electrolyte, and solution temperature also influence the characteristics of the diffusion layer [79].

When the diffusion layer remains small compared to the electrode dimensions, the system can be modeled as semi-infinite linear diffusion to a planar electrode surface. Under these conditions, Fick's second law simplifies to [80]:

$$\frac{\partial C_O(x,t)}{\partial t} = D_O \frac{\partial^2 C_O(x,t)}{\partial x^2} \tag{1.21}$$

This scenario leads to the classical **Cottrell equation** for the time-dependent current in chronoamperometry:

$$i(t) = \frac{nFAC_O^* \sqrt{D_O}}{\sqrt{\pi t}} \tag{1.22}$$

This inverse square-root time dependence, $i(t) \propto t^{-1/2}$, arises from the continuous depletion of electrochemically active species at the electrode surface during the electrolysis process.

In chronoamperometry involving a spherical electrode (e.g., a hanging mercury drop), the diffusion field is spherical rather than planar. This alters Fick's second

law by introducing a radial component, resulting in:

$$\frac{\partial C_O(r,t)}{\partial t} = D_O \left(\frac{\partial^2 C_O(r,t)}{\partial r^2} + \frac{2}{r} \frac{\partial C_O(r,t)}{\partial r} \right) \tag{1.23}$$

where r is the radial distance from the center of the electrode and r_0 is the radius of the spherical electrode.

The analytical solution for the diffusion-limited current at the electrode surface is given by:

$$i_{d,c}(t) = nFAD_O C_O^* \left[\frac{1}{\sqrt{\pi D_O t}} + \frac{1}{r_0} \right] \tag{1.24}$$

This expression combines a transient term proportional to $t^{-1/2}$, similar to the Cottrell current for planar electrodes, and a steady-state term $\frac{1}{r_0}$ arising from the curvature of the spherical electrode. Over time, the system transitions from transient diffusion control to a steady-state regime, with the curvature facilitating continuous access of fresh electrolyte to the electrode surface [81].

1.8.2 Electrical Double Layer Theory

The electrical double layer (EDL) forms at the interface between a solid electrode and a liquid electrolyte when an external potential is applied. This interfacial region behaves like an ideal plate capacitor in which the charged layers are separated by a small distance. Under the influence of the electric field caused by the applied potential, ions in the electrolyte migrate toward the solid surface, forming a structured layer. The interaction between the surface charges in the solid phase and the compensating counter-ions in the electrolyte phase gives rise to a capacitive effect[82].

Understanding the nature and behavior of the electrical double layer is essential for the design and optimization of high-performance electrochemical systems

such as supercapacitors, fuel cells, biosensors, photoelectrochemical cells, electrochromic devices, electrochemical sensors, and energy storage technologies.

Chronologically, the first theoretical model was proposed by Hermann von Helmholtz [83]. He suggested that when an electrode surface is charged (either positively or negatively), counter-ions from the electrolyte are attracted electrostatically to the surface and form a compact layer of adsorbed ions, similar to a charged capacitor. The system was assumed to behave like a simple plate capacitor. The capacitance in this model is given by:

$$\sigma = \frac{\varepsilon\varepsilon_0}{d}V \tag{1.25}$$

Here, ε is the dielectric constant of the medium, ε_0 is the vacuum permittivity, and d is the distance between the charged plates (i.e., the electrode surface and the counter-ion layer). From this, the differential capacitance C_H becomes [82]:

$$C_H = \frac{d\sigma}{dV} = \frac{\varepsilon\varepsilon_0}{d} \tag{1.26}$$

A key limitation of the Helmholtz model is that it predicts a constant capacitance, which contradicts experimental observations. In reality, as shown in systems like mercury in NaF solutions, the differential capacitance varies with applied potential and electrolyte concentration [84].Moreover, the model neglects important effects such as thermal motion (Brownian motion) and the random distribution of ions in the electrolyte.

To address these limitations, the Gouy–Chapman model was developed. This model is based on the following assumptions [85]:

- The electrode is an infinite, flat surface uniformly charged.
- The electrolyte is symmetric and dilute (e.g., 1:1 electrolyte like NaCl).
- Ions are treated as point charges with no volume.

- Ion distribution in the solution follows a Boltzmann distribution, dependent on the local electrostatic potential.
- The potential profile in the solution satisfies the Poisson equation.

Under these assumptions, counter-ions do not form a tightly packed layer near the surface, but instead are distributed diffusely, forming what is referred to as the *diffuse layer*. This diffuse distribution arises due to the balance between electrostatic attraction and thermal motion. The resulting charge distribution can be described by the Boltzmann distribution:

$$C_j(x) = C_j^* \exp\left(-\frac{z_j e\phi(x)}{kT}\right) \tag{1.27}$$

This model, therefore, provides a more physically realistic picture of the electrical double layer by accounting for ion mobility and thermal effects.

For each ion species, the concentration at position x is given by:

$$C_j(x) = C_j^* \cdot \exp\left(-\frac{z_j e\phi(x)}{kT}\right)$$

Where:

- C_j^*: Bulk concentration of ion j
- z_j: Charge of ion j
- e: Elementary charge
- $\phi(x)$: Electric potential at position x (relative to the bulk)
- k: Boltzmann constant
- T: Absolute temperature

Afterwards, the ion concentration term is incorporated into the Poisson equation.

The **Poisson equation** is a fundamental differential equation that relates charge density to the electric potential field. In electrochemistry, electrolytes are ionic media, and this equation is used to determine the electric potential profiles within such systems.

The Poisson equation describes the relationship between electric potential and charge density.[86, p. 43] It is a fundamental equation used to model electric fields in ionic media such as electrolytes.

$$\nabla^2 \phi(\mathbf{r}) = -\frac{\rho(\mathbf{r})}{\varepsilon \varepsilon_0}$$

$$\frac{d^2\phi(x)}{dx^2} = -\frac{\rho(x)}{\varepsilon \varepsilon_0}$$

- $\phi(x)$: Electric potential at position x, in volts (V)
- $\rho(x)$: Charge density at position x, in coulombs per cubic meter ($\mathrm{C/m^3}$)
- ε: Relative permittivity (dielectric constant) of the medium (dimensionless)
- ε_0: Vacuum permittivity, $\varepsilon_0 = 8.85 \times 10^{-12}\,\mathrm{F/m}$

The second derivative in the Poisson equation directly originates from **Gauss's law**:[86, p. 65]

$$\nabla \cdot \mathbf{E} = \frac{\rho}{\varepsilon \varepsilon_0}$$

The electric field $\mathbf{E}$ is the **vector derivative (gradient)** of the scalar electric potential ϕ:

$$\mathbf{E} = -\nabla\phi$$

Substituting into Gauss's law:

$$\nabla \cdot (-\nabla\phi) = -\nabla^2\phi = \frac{\rho}{\varepsilon\varepsilon_0} \quad \Rightarrow \quad \nabla^2\phi = -\frac{\rho}{\varepsilon\varepsilon_0}$$

This yields the general form of the Poisson equation.

As the distance from the electrode increases, the distribution of ions becomes more dilute.

At very high ion concentrations, the effect of **ion crowding** is typically neglected, which limits the model's accuracy. In addition, the model tends to fail at **high surface potentials**, where linear approximations or basic assumptions no longer hold. Returning to the **Gouy–Chapman model**, we can define the *charge density* as a function of position and then relate it to the **Poisson equation** to obtain the potential profile in the diffuse layer.

$$\rho(x) = \sum_j z_j e C_j(x) = \sum_j z_j e C_j^* \exp\left(-\frac{z_j e\phi(x)}{kT}\right)$$

$$\frac{d^2\phi}{dx^2} = -\frac{\rho(x)}{\varepsilon\varepsilon_0}$$

By combining equations, we obtain the **Poisson–Boltzmann equation**, which describes the electric potential in ionic solutions.

For a symmetric electrolyte (e.g., NaCl), the differential equation for the potential is:

$$\frac{d\phi}{dx} = -\left(\frac{8kTn_0}{\varepsilon\varepsilon_0}\right)^{1/2} \sinh\left(\frac{ze\phi}{2kT}\right) \tag{1.28}$$

By integrating, the potential profile is obtained (for small potentials):

$$\phi(x) = \phi_0 e^{-\kappa x} \quad \text{(for small potentials)} \tag{1.29}$$

- κ^{-1}: **Debye length** – indicates how far the potential extends before decaying toward zero.
- At **low ionic strength**, the diffuse layer is **thicker**; at **high ionic strength**, it is **thinner**.

By integrating the potential gradient, the potential profile $\phi(x)$ can be obtained. This leads to the concept of the **Debye length** κ^{-1}, which indicates how far the electric potential extends into the solution before approaching zero. It represents the distance over which ions can sense the electrode's electric field.

The **Gouy–Chapman model** defines the relationship between surface charge density and surface potential, and enables the calculation of the *differential capacitance*:

- The differential capacitance varies with potential and has a **V-shaped** profile.
- The minimum capacitance occurs near the **point of zero charge (PZC)**.
- This model performs well under **low ionic strength** and **small potential differences**.
- It fails at high potentials or high concentrations due to neglected factors such as ion size, specific adsorption, and solvent effects.

To overcome these shortcomings, the **Stern model** was proposed. Unlike the Gouy–Chapman model, which allows point ions to approach arbitrarily close to the electrode (leading to unrealistically large capacitance at high potential), the Stern model introduces the concept of finite-sized, solvated ions.

- The closest plane ions can approach is called the **Outer Helmholtz Plane (OHP)**.
- The region between the electrode and the OHP is the **compact (Helmholtz) layer**.
- Beyond the OHP lies the **diffuse layer**, which still follows Gouy–Chapman behavior.
- The total double layer is modeled as **two capacitors in series**: one for the Helmholtz layer, and one for the diffuse layer.

In the **Stern model** [82], the differential capacitance is represented as two capacitors connected in series:

$$\frac{1}{C_{\text{GCS}}} = \frac{1}{C_H} + \frac{1}{C_D} \tag{1.30}$$

Where:

- C_H: Capacitance of the Helmholtz (compact) layer — constant.
- C_D: Capacitance of the Gouy–Chapman (diffuse) layer — potential-dependent.

This model better matches experimental behavior

- At low potential and low ionic strength, C_D is small, leading to a **V-shaped** total capacitance profile.
- At high ionic strength, C_D becomes large, so the total capacitance is dominated by the constant C_H.

The Debye length λ_D, also expressed as κ^{-1}, for a symmetric $z:z$ electrolyte is given by:

$$\lambda_D = \kappa^{-1} = \left(\frac{\varepsilon \varepsilon_0 kT}{2 n_0 z^2 e^2} \right)^{1/2} \tag{1.31}$$

Where:

- ε: Relative permittivity of the medium
- ε_0: Vacuum permittivity ($8.85 \times 10^{-12}\,\mathrm{F/m}$)
- k: Boltzmann constant ($1.38 \times 10^{-23}\,\mathrm{J/K}$)
- T: Absolute temperature (K)
- n_0: Bulk number density of ions (ions/m^3)
- z: Ion valence
- e: Elementary charge ($1.602 \times 10^{-19}\,\mathrm{C}$)

For aqueous solutions at 25°C, the formula can be simplified as:

$$\lambda_D\,(\mathrm{nm}) \approx \frac{0.304}{z\sqrt{C^*}} \tag{1.32}$$

where C^* is the bulk electrolyte concentration in mol/L.

Although the **GCS model** (Gouy–Chapman–Stern) better reflects the behavior of real systems, it is still not entirely sufficient, as it neglects several important effects, including:the potential dependence of the Helmholtz layer capacitance,ion–ion interactions,specific adsorption phenomena,and electron spillover near the electrode surface. A study proposes a new double-layer model that incorporates ion–surface attraction as a parallel capacitive element to explain deviations from the Gouy–Chapman–Stern model observed even in dilute electrolytes. The model suggests that the interaction is weak, non-specific to ion type, and that ion size plays a role in determining the potential of minimum capacitance[85].

1.9 Introduction to Cyclic Voltammetry and Modelling

Cyclic voltammetry is an electrochemical measurement technique in which a potential is applied over a defined range at a specific rate (called the sweep rate), and the resulting current is measured. Before the development of cyclic voltammetry, the dropping mercury polarography method was invented in 1922 [87]. However, going even further back, we can refer to Lippmann's work and his invention of the capillary electrometer to measure the surface tension of polarized mercury [87].

Later, in 1903, Professor Kucera modified this system [87]. Lippmann's setup is referred to as a static method because the mercury in the capillary does not flow or drip; instead, its height is adjusted to remain constant. In this way, it provided the first quantitative demonstration of how electric potential affects surface tension. With Kucera's modification, the system evolved into what we now recognize as the dropping mercury setup, through which he investigated the relationship between mercury drop weight and applied potential [87].

The drop weight in Lippmann's method depends solely on surface tension (a function of potential) and remains independent of the mercury column height or flow pressure. This modification was referred to as a dynamic method, in contrast to Lippmann's static approach. Kucera's dynamic electrocapillary measurements occasionally exhibited anomalous curves with a secondary maximum, unlike the typical single peaked curves observed by Lippmann. These anomalies were particularly seen in dilute electrolyte solutions and aqueous solutions of lower fatty acids, although their origin remained unexplained at the time [87].

It was precisely at this point that these anomalies attracted the attention of Jaroslav Heyrovský, who became determined to explore the problem further. He would later explain that these anomalies were caused by a streaming effect the convective mass transport induced by the falling mercury drop occurring in addition to normal diffusion. During this research, Heyrovský's interest increasingly

shifted toward studying electrode processes and electrochemical phenomena [87].

Unlike previous methods, he developed an electronic circuit that could measure the current generated under an applied potential, which led him while investigating the irregularities in Kucera's curves to invent a new electrochemical technique: polarography [87]. With these pioneering contributions, Heyrovský was eventually awarded the Nobel Prize in Chemistry in 1959. From then until now, this technique was developed further, a third electrode is added as referred as counter electrode and different kind of workings electrodes are invented like microelectrodes, rotating disk electrodes, working electrodes are from various king of materials like carbon materials or transparent doped glass materials. Those improvements enhance power of cyclic voltammetry.

The advancements in cyclic voltammetry are not limited to experimental techniques; significant efforts have also been made to analyze it computationally. The first initiatives in computational electrochemical analysis date back to 1967, introduced by John Newman [88] , and later in 1988 by Ralph E. White [89].

They described electrochemical systems based on three fundamental processes: diffusion, electromigration, and electrochemical reaction, all of which are interdependent. These processes are mathematically represented by partial differential equations (PDEs) to describe their evolution in space and time. Since the governing equations are inherently coupled, the overall system is referred to as a set of coupled partial differential equations. In the 1960s and 1970s, computational resources were limited, and there were few effective tools available to solve such complex systems. FORTRAN, introduced in 1957, was one of the earliest programming languages used for solving linear equation systems. Leveraging this infrastructure, Newman developed an efficient matrix-based solution method [90], known as the BAND matrix method, where the equations at each spatial point are solved within a structured matrix system. This approach proved especially useful for modeling electrochemical systems.

Ralph E. White and his group utilized this method to simulate theoretical cyclic voltammograms of conducting polymers... as shown in a mathematical

model for polypyrrole [89]. Today, while the theoretical framework of electrochemical systems remains fundamentally similar, new tools have been developed for their solution. For instance, software such as COMSOL Multiphysics [91] and Python-based libraries [92] are now commonly used. Moreover, Newman's BAND matrix methodology can also be implemented using Python, allowing for flexible and customizable simulations [93].

1.10 Partial Differential Equations, Coupled PDEs and Solutions

Partial differential equations (PDEs) arise naturally in scientific disciplines and often form the foundation of scientific theories. A PDE involves more than one independent variable, and the unknown function depends on these variables and their partial derivatives. PDEs describe various physical, biological, and chemical processes such as transport, wave mechanics, and enzymatic reactions. Each of these corresponds to a specific type of process.

For instance, one of the most well-known phenomena in transport is diffusion. The diffusion of particles depends on the concentration gradient, as described by Fick's First Law [94, 95]:

$$J = -D\frac{\partial c}{\partial x} \tag{1.33}$$

Here, J represents the diffusive particle flux, c is the concentration (in three spatial dimensions x, y, z), x denotes the spatial coordinate, and D is the diffusion coefficient (or diffusivity). This formulation describes how the concentration of particles evolves in space. When expressed in three dimensions, it is classified as a linear partial differential equation; however, if c depends only on a single spatial variable, the equation reduces to an ordinary differential equation.

In mathematics, elements that perform operations on functions are called *operators*. For example, let us define an operator L, whose task is to take the derivative:

$$L = \frac{\partial}{\partial x} \tag{1.34}$$

This operator takes the derivative of a function with respect to x. Applying this operator to a function v yields:

$$Lv = \frac{\partial v}{\partial x} = v_x \tag{1.35}$$

Another operator may perform a more complex operation. For example:

$$L = \frac{\partial}{\partial x} + y\frac{\partial}{\partial y} \tag{1.36}$$

Then the operator acting on a function u gives:

$$Lu = u_x + yu_y \tag{1.37}$$

Linear operators are special types of operators that satisfy two fundamental properties: *additivity* and *homogeneity* (with respect to scalar multiplication) [96, p. 2].

- **Additivity:** Applying the operator to the sum of two functions is equivalent to applying the operator to each function separately and then adding the results:
$$L(u + v) = Lu + Lv \tag{1.38}$$
- **Homogeneity:** Applying the operator to a scalar multiple of a function allows the scalar to be factored out:
$$L(cu) = cLu \tag{1.39}$$

Let us illustrate these properties with an example. When examining Fick's First Law, we observe that the diffusive particle flux depends solely on the first derivative of concentration. If we apply the above two properties to this relationship, it becomes evident that the underlying differential equation possesses linear characteristics. Here, we assume that the diffusion coefficient D is constant. If, however, D is a function of space or concentration (as may be the case in biological tissues or other heterogeneous systems), the system may become non-linear. Linear equations can be either homogeneous or inhomogeneous:

- $Lu = 0$ (Homogeneous linear equation)
- $Lu = g$ (Inhomogeneous linear equation, where $g \neq 0$)

A key advantage of homogeneous linear equations is that they obey the principle of superposition, meaning that linear combinations of solutions are also solutions.

Another important type of partial differential equations (PDEs) is their coupled form. Let us consider a system that is closed, containing no particles initially. When a certain number of particles is introduced into the box, they begin to diffuse from regions of high concentration to regions of low concentration. This represents a relatively simple case, and the concentration of particles at a given position or time depends only on the concentration gradient.

$$\frac{\partial C_i}{\partial t} = D\frac{\partial^2 C_i}{\partial x^2} \qquad \text{(Case 1)} \tag{1.40}$$

Now, by developing the system, we consider the same box filled with a liquid containing ionic species, i.e., positively and negatively charged particles. These charged particles can also be driven by an electric field. As a result, the change in concentration over time will depend on both the diffusion of particles and their electromigration. This relationship can be expressed mathematically as:

$$\frac{\partial C_i}{\partial t} = D\frac{\partial^2 C_i}{\partial x^2} + \frac{z_i F D_i}{RT}\frac{\partial}{\partial x}\left(C_i \frac{\partial \Phi_2}{\partial x}\right) \qquad \text{(Case 2)} \tag{1.41}$$

Next, we introduce a boundary on one side of the system, composed of an electrochemically active material. When an external potential is applied, this material begins to transfer electrons, causing its net charge to change. In response to this change, the material becomes either positively or negatively charged, thereby attracting oppositely charged counter-ions from the solution. The mathematical expression of such a system is given by:[89]

$$\frac{\partial C_i}{\partial t} = D\frac{\partial^2 C_i}{\partial x^2} + \frac{z_i F D_i}{RT}\frac{\partial}{\partial x}\left(C_i \frac{\partial \Phi_2}{\partial x}\right) - \frac{S_i}{nF}a_j \qquad \text{(Case 3)} \tag{1.42}$$

In such a complex setup the evolution of the number of charged particles depends not only on diffusion, but also on electromigration (movement under an electric field), and electrochemical reactions occurring at the electrochemically active interface. If we introduce yet another element, such as convective flow (because we are working in a liquid environment), this flow will also influence the spatial and temporal evolution of the concentration of charged species.

Another example is chemical reactions. Chemical reactions do not always proceed in a single step; instead, they often consist of multiple sequential steps, each characterized by a different rate constant and reaction order. Some of these steps occur more slowly, while others proceed more rapidly. This distinction determines the so-called rate-determining step. Consecutive reactions can be described using coupled partial differential equations, as the concentrations of the intermediate and product species are interdependent—each species is both formed and consumed as part of the overall reaction mechanism.

Analytical or numerical methods can be used to solve PDEs. An analytical solution is an exact mathematical expression obtained using methods such as separation of variables or transform techniques (e.g., Laplace and Fourier) [96]. However, not all PDEs can be solved analytically. Equations that are nonlinear,

involve complex geometries, or are defined over heterogeneous systems are typically solved approximately using numerical methods. Examples of such methods include the finite difference method, finite element method, Newton–Raphson, Thomas algorithm, and various other numerical algorithms [97].

1.10.1 A Numerical Solution Method of Coupled Partial Differential Equations for Chemical Systems: Newman Algorithm

In the solution methodology presented herein [90], a one-dimensional (1D) spatial domain is considered. Let the x-axis represent the direction along which the variable of interest varies. This domain is discretized into j intervals. The points at $j = 0$ and $j = j_{\max}$ correspond to the boundaries of the system and are defined by appropriate boundary conditions. In order to obtain a complete numerical solution, the values at these boundary nodes must be specified. For all interior nodes, that is, nodes excluding the boundary points, the governing equations can be expressed in the following general form:

$$\sum_{k=1}^{n} A_{i,k}(j)C_k(j-1) + B_{i,k}(j)C_k(j) + D_{i,k}(j)C_k(j+1) = G_i(j) \tag{1.43}$$

The equation of the unknown variable is expressed from C_1 to C_n, indicating that there are n coupled equations within the system. These equations are interdependent, forming a coupled system. The index i denotes the equation number, while C_k represents the unknown variable. The terms $A_{i,k}(j)$, $B_{i,k}(j)$, and $D_{i,k}(j)$ correspond to the coefficients of the unknowns at the mesh points $j-1$, j, and $j+1$, respectively [88].

The equation presented above is used to express linear coupled equations through the finite difference method. The finite difference method is a numerical technique commonly used for solving differential equations. Before discussing the

linearization of the equation and the meaning of the coefficients, let us briefly review the finite difference method.

The primary objective of the finite difference method is to approximate equations that are expressed in the form of partial differential equations (PDEs). Using this method, the approximated equations are transformed into an algebraic system of equations, which can then be solved numerically using computational tools instead of analytically. Since this method provides an approximate solution, it is essential to assess and analyze the accuracy of the system [98].

To proceed with the method, let us consider a function that depends on x, namely $u(x)$. We assume that $u(x)$ is continuous and differentiable. The derivative of the function, $u'(x)$, evaluated at a point a, can be expressed as follows. The forward difference approximation of the derivative at point a is given by:

$$D_+u(a) = \frac{u(a+h) - u(a)}{h} \tag{1.44}$$

Here, h is a small positive value. As $h \to 0$, this expression approaches the standard definition of the derivative based on the limit:

$$\lim_{h\to 0} \frac{u(a+h) - u(a)}{h} = u'(a) \tag{1.45}$$

Geometrically, the value $D_+u(a)$ represents the slope of the line that passes through the points $(a, u(a))$ and $(a+h, u(a+h))$. In practice, the derivative can be approximated using the forward-difference formula:

$$D_+u(a) = \frac{u(a+h) - u(a)}{h} = u'(a) + \mathcal{O}(h) \tag{1.46}$$

This approximation is valid for values of $x > a$, and its truncation error is of order $\mathcal{O}(h)$, meaning the accuracy improves linearly as h decreases.

For values $x < a$, the derivative can be approximated using the backward-difference formula:

$$D_{-}u(a) = \frac{u(a) - u(a-h)}{h} = u'(a) + \mathcal{O}(h) \tag{1.47}$$

The backward-difference method also has a truncation error of order $\mathcal{O}(h)$. These two approximations are known, respectively, as the forward-difference and backward-difference schemes [98], and are both classified as first-order accurate methods.

An alternative approach is the central difference approximation, which is defined as:

$$D_0 u(a) = \frac{u(a+h) - u(a-h)}{2h} = \frac{1}{2}\left(D_{+}u(a) + D_{-}u(a)\right) \tag{1.48}$$

This expression gives the slope of the line that passes through the points $(a-h, u(a-h))$ and $(a+h, u(a+h))$. The central difference method is more accurate than both the forward and backward methods. It is a second-order accurate approximation, meaning that the associated error decreases more rapidly as $h \to 0$.

The error introduced by finite difference expressions is known as the truncation error. Finite difference approximations of a function can be derived by expanding the function using its Taylor series around the point a. [98]

The Taylor series expansion of $u(x)$ about the point a evaluated at $a+h$ and $a-h$ is given respectively by:

$$u(a+h) = u(a) + hu'(a) + \frac{h^2}{2!}u''(a) + \frac{h^3}{3!}u^{(3)}(a) + \frac{h^4}{4!}u^{(4)}(a) + \cdots \tag{1.49}$$

$$u(a-h) = u(a) - hu'(a) + \frac{h^2}{2!}u''(a) - \frac{h^3}{3!}u^{(3)}(a) + \frac{h^4}{4!}u^{(4)}(a) - \cdots \tag{1.50}$$

Subtracting the two equations for the central difference method:

$$u(a+h) - u(a-h) = 2hu'(a) + \frac{2h^3}{6}u^{(3)}(a) + \cdots \tag{1.51}$$

Dividing both sides of the last expression by $2h$ gives the central difference approximation:

$$\frac{u(a+h) - u(a-h)}{2h} = u'(a) + \frac{h^2}{3!}u^{(3)}(a) + \cdots \tag{1.52}$$

This shows that the truncation error of the central difference method is of the order $\mathcal{O}(h^2)$, as the leading error term is proportional to h^2. Therefore, the central difference is a second-order accurate approximation of the first derivative.

The expression above represents the first derivative of a function using the finite-difference method. It is also possible to approximate the second derivative of the same function using a similar approach.

The second-order central difference approximation for the second derivative of a function $u(x)$ at point a is given by:

$$u''(a) \approx \frac{u(a+h) - 2u(a) + u(a-h)}{h^2} \tag{1.53}$$

This formula is derived by adding the Taylor series expansions of $u(a+h)$ and $u(a-h)$, and eliminating the first derivative terms.The truncation error of this approximation is of order $\mathcal{O}(h^2)$, making it a second-order accurate method for estimating the second derivative.

Let us now consider the expressions above in conjunction with the general equation (Eq. (1.43)). It is evident that the point a corresponds to node j in the mesh system, $a - h$ corresponds to node $j - 1$, and $a + h$ corresponds to node $j + 1$. Therefore, when expressing the first and second derivatives of an unknown variable C_k at node j, the following central finite difference approximations can be used [88]:

$$\left.\frac{\partial C_k}{\partial x}\right|_j \approx \frac{C_k(j+1) - C_k(j-1)}{2h} + \mathcal{O}(h^2) \tag{1.54}$$

$$\left.\frac{\partial^2 C_k}{\partial x^2}\right|_j \approx \frac{C_k(j+1) - 2C_k(j) + C_k(j-1)}{h^2} + \mathcal{O}(h^2) \tag{1.55}$$

At the boundary point where $j = 0$, the term $C_k(j-1)$ cannot be evaluated directly due to the lack of information beyond the physical domain. Therefore, an alternative technique known as the *image point method* is employed at such locations[99, p. 611].This method will be discussed in detail later. For now, let us focus on how the equations are formulated at the interior node points, excluding the boundaries.

We start with a general form of a linear system that involves the second derivative, first derivative, and the function itself for each unknown variable. Therefore, each term in this expression can be represented individually using finite difference approximations.

$$\sum_{k=1}^{n} a_{i,k}(x)\frac{d^2 c_k(x)}{dx^2} + b_{i,k}(x)\frac{dc_k(x)}{dx} + d_{i,k}(x)c_k(x) = g_i(x) \tag{1.56}$$

Starting from Eq. (1.56), we obtain its finite difference form, which corresponds to the discretized system in Eq. (1.43). Each derivative term multiplied by the coefficients $a_{i,k}(x)$, $b_{i,k}(x)$, and $d_{i,k}(x)$ can be expressed using central difference approximations as follows:

$$a_{i,k}(x) \cdot \frac{d^2 c_k(x)}{dx^2} \approx a_{i,k}(x) \cdot \frac{C_k(j+1) - 2C_k(j) + C_k(j-1)}{h^2} \tag{1.57}$$

$$b_{i,k}(x) \cdot \frac{dc_k(x)}{dx} \approx b_{i,k}(x) \cdot \frac{C_k(j+1) - C_k(j-1)}{2h} \tag{1.58}$$

$$d_{i,k}(x) \cdot c_k(x) \approx d_{i,k}(x) \cdot C_k(j) \tag{1.59}$$

Substituting these approximations into Equation Eq. (1.56), we obtain the following discrete form:

$$\begin{aligned} a_{i,k}(x_j) \cdot \frac{C_k(j+1) - 2C_k(j) + C_k(j-1)}{h^2} \\ + b_{i,k}(x_j) \cdot \frac{C_k(j+1) - C_k(j-1)}{2h} \\ + d_{i,k}(x_j) \cdot C_k(j) = g_i(x_j) \end{aligned} \tag{1.60}$$

In the next step, the coefficients corresponding to the unknowns $c(j-1)$, $c(j)$, and $c(j+1)$ are grouped and denoted by A, B, and D, respectively.

$$C_k(j) = c_k(x_j) \qquad \text{for all } j \tag{1.61}$$

The index j represents the position of a node on the discretized mesh and is an integer counter. The corresponding spatial coordinate is given by $x_j = jh$, where h is the uniform grid spacing. The function $c_k(x)$ represents the continuous solution of the differential equation, whereas $C_k(j)$ denotes its numerical approximation at the discrete mesh point x_j.

$$A_{i,k}(j) = a_{i,k}(x_j) - \frac{h}{2} b_{i,k}(x_j) \qquad \text{for } j = 1 \text{ to } NJ \tag{1.62}$$

$$B_{i,k}(j) = -2a_{i,k}(x_j) + h^2 d_{i,k}(x_j) \qquad \text{for } j = 1 \text{ to } NJ \tag{1.63}$$

$$D_{i,k}(j) = a_{i,k}(x_j) + \frac{h}{2} b_{i,k}(x_j) \qquad \text{for } j = 1 \text{ to } NJ \tag{1.64}$$

$$G_i(j) = h^2 g_i(x_j) \qquad \text{for } j = 1 \text{ to } NJ \tag{1.65}$$

We have now obtained a general finite representation of the partial differential equations by expressing them in finite difference form, resulting in the formulation presented in Eq. (1.43).

In a mesh-based system, the unknown at each point can be expressed using this general equation form. For instance, in a system where the starting index is $j = 0$, the equations corresponding to the points $j = 1$, $j = 2$, and $j = 3$ and $j = 4$ are written as follows:

$$\sum_{k=1}^{n} B_{i,k}(0)\, C_k(0) + D_{i,k}(0)\, C_k(1) = G_i(0) \tag{1.66}$$

$$\sum_{k=1}^{n} A_{i,k}(1)\, C_k(0) + B_{i,k}(1)\, C_k(1) + D_{i,k}(1)\, C_k(2) = G_i(1) \tag{1.67}$$

$$\sum_{k=1}^{n} A_{i,k}(2)\, C_k(1) + B_{i,k}(2)\, C_k(2) + D_{i,k}(2)\, C_k(3) = G_i(2) \tag{1.68}$$

$$\sum_{k=1}^{n} A_{i,k}(3)\, C_k(2) + B_{i,k}(3)\, C_k(3) + D_{i,k}(3)\, C_k(4) = G_i(3) \tag{1.69}$$

$$\sum_{k=1}^{n} A_{i,k}(4)\, C_k(3) + B_{i,k}(4)\, C_k(4) = G_i(4) \tag{1.70}$$

At the initial point $j = 0$, the term containing A cannot be written, as the value at $j - 1$ is not known. Similarly, at the final point $j = j_{\max} = 4$, the term containing D cannot be written, since the value at $j + 1$ is not available.

It is known that the resulting system of equations is linear. In the case of non-linear systems, linearization is typically applied. While solving such a system manually for three mesh points may be feasible, attempting the same approach for $j = 100$ points is highly inefficient and impractical. Therefore, the system is reformulated in a matrix-compatible form and solved by inverting the coefficient matrix.

Accordingly, the matrix representation of the system can be expressed as:

$$\mathbf{A} \cdot \mathbf{C} = \mathbf{G} \tag{1.71}$$

where $\mathbf{A}$ denotes the coefficient matrix, $\mathbf{C}$ is the vector of unknowns, and $\mathbf{G}$ represents the known right-hand side vector.By taking the inverse of the matrix $\mathbf{A}$, the unknown vector $\mathbf{C}$ can be computed as:

$$\mathbf{C} = \mathbf{A}^{-1} \cdot \mathbf{G} \tag{1.72}$$

Now, let us represent the system of equations defined at the mesh points $j = 0, 1, 2, 3, 4$ in matrix form.

$$\begin{bmatrix} B(0) & D(0) & 0 & 0 & 0 \\ A(1) & B(1) & D(1) & 0 & 0 \\ 0 & A(2) & B(2) & D(2) & 0 \\ 0 & 0 & A(3) & B(3) & D(3) \\ 0 & 0 & 0 & A(4) & B(4) \end{bmatrix} \begin{bmatrix} C(0) \\ C(1) \\ C(2) \\ C(3) \\ C(4) \end{bmatrix} = \begin{bmatrix} G(0) \\ G(1) \\ G(2) \\ G(3) \\ G(4) \end{bmatrix} \tag{1.73}$$

Before obtaining the solution by inverting the coefficient matrix, one final step remains: defining the boundary conditions. The general equation we use for this purpose will differ from Eq. (1.43).

$$\sum_{k=1}^{n} p_{i,k}(x)\frac{dc_k}{dx} + e_{i,k}(x)\, c_k = f_i(x) \tag{1.74}$$

In general, three types of boundary conditions are commonly used: Dirichlet, Neumann, and Robin conditions. In the Dirichlet condition, the boundary value is fixed, for example $C(0) = c_0$. In the Neumann condition, the boundary is defined by the first derivative and this derivative is constant, such as $\frac{dc}{dx}(0) = 0$ [98]. Finally, the Robin condition is a mixed type, involving both the value and its derivative [100].

The boundary condition used by Newman, as presented above, is also of the Robin type, as it includes both the derivative and the value at the boundary. However, in order to evaluate the derivative using the central difference method, information from both the preceding and following mesh points is required. For example, let $j = 0$ denote the left boundary and $j = 4$ the right boundary. To enable the application of the central difference approximation at these boundaries, the points $j = 1$ and $j = 3$ are redefined as the new physical boundaries. Accordingly, the original boundary points $j = 0$ and $j = 4$ are treated as *image points*.

The next step is to express the boundary condition equation Eq. (1.74) in its general form using the central difference approximation and to derive the specific forms of the X and Y coefficients for the boundaries. After this step, the complete matrix system can be constructed.

Using the central difference approximation given in Eq. (1.54), the first derivative term in the boundary condition can be discretized accurately.

$$\sum_{k=1}^{n} p_{i,k}(x)\frac{dc_k}{dx} + e_{i,k}(x)c_k = f_i(x) \tag{1.75}$$

To use central difference approximations for the derivatives in Eq. (1.75), Newman introduced the concept of an image point. That is, he let the points $j = 0$

and $j = NJ$ be image points and the physical boundaries be at $j = 1$ and $j = NJ - 1$.

Then, for $j = 0$, Eq. (1.75) becomes:

$$\sum_{k=1}^{n} B_{i,k}(0)C_k(0) + D_{i,k}(0)C_k(1) + X_{i,k}C_k(2) = G_i(0) \tag{1.76}$$

$$B_{i,k}(0) = -X_{i,k} = -\frac{p_{i,k}(0)}{2} \tag{1.77}$$

$$D_{i,k}(0) = h\, e_{i,k}(0) \tag{1.78}$$

$$G_i(0) = h\, f_i(0) \tag{1.79}$$

and for $j = NJ$ becomes:

$$\sum_{k=1}^{n} Y_{i,k}C_k(NJ-2) + A_{i,k}(NJ)C_k(NJ-1) + B_{i,k}(NJ)C_k(NJ) = G_i(NJ) \tag{1.80}$$

$$\begin{aligned} \text{where} \quad Y_{i,k} &= -B_{i,k}(NJ) = -\frac{p_{i,k}(x)}{2} \\ A_{i,k}(NJ) &= h\, e_{i,k}(x) \\ G_i(NJ) &= h\, f_i(x) \end{aligned} \tag{1.81}$$

After the above descriptions regarding the boundary conditions and interior points, the finalized structure of the matrix is given as follows:

$$\begin{bmatrix} B(0) & D(0) & X & & & & & \\ A(1) & B(1) & D(1) & & & & & \\ & A(2) & B(2) & D(2) & & & & \\ & & \ddots & \ddots & \ddots & & & \\ & & & A(j) & B(j) & D(j) & & \\ & & & & \ddots & \ddots & \ddots & \\ & & & & Y & A(NJ) & B(NJ) \end{bmatrix} \begin{bmatrix} C(0) \\ C(1) \\ C(2) \\ \vdots \\ C(j) \\ \vdots \\ C(NJ) \end{bmatrix} = \begin{bmatrix} G(0) \\ G(1) \\ G(2) \\ \vdots \\ G(j) \\ \vdots \\ G(NJ) \end{bmatrix}$$

1.10.1.1 Reaction-Diffusion Model for an Enzymatic system a Simple Example

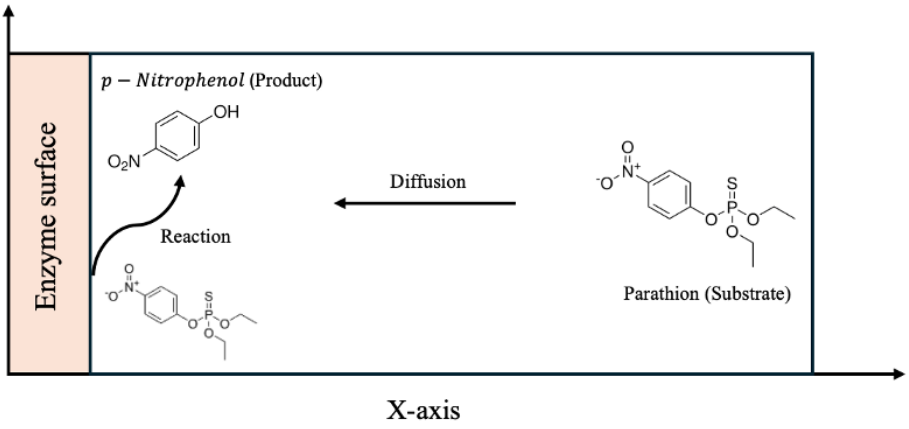

Figure 1.6: Illustration of the reaction-diffusion mechanism.

To understand the concepts summarized in the previous chapters, a simpler example than cyclic voltammetry modeling can be considered.Figure 1.6 schematically illustrates the reaction–diffusion mechanism, where the substrate parathion undergoes enzymatic reaction at the enzyme surface to form *p*-nitrophenol, followed by diffusion away from the interface.

In this model, **parathion**,an organophosphate insecticide and acaricide,is enzymatically converted to **p-nitrophenol**, and this conversion is studied using Michaelis–Menten kinetics.

The enzymatic reaction can be expressed as:

$$\mathrm{E} + \mathrm{S} \underset{k_{-1}}{\overset{k_1}{\rightleftharpoons}} \mathrm{ES} \xrightarrow{k_2} \mathrm{E} + \mathrm{P}$$

- **E**: Enzyme
- **S**: Substrate (Parathion)
- **ES**: Enzyme-substrate complex
- **P**: Product (P-nitrophenol)

The overall chemical equation is:

$$\text{Parathion} + \mathrm{H_2O} \xrightarrow{\text{OPH}} \text{p-Nitrophenol} + \text{Diethyl thiophosphate}$$

- **OPH**: Organophosphorus hydrolase enzyme

Based on Michaelis–Menten kinetics (with the steady-state assumption), the rate of product formation is given by:

$$\frac{d[P]}{dt} = k_2[\mathrm{ES}] = \frac{V_{\max}[S]}{K_m + [S]} \tag{1.82}$$

where:

$$K_m = \frac{k_{-1} + k_2}{k_1} \tag{1.83}$$

- $[S]$: Substrate concentration
- [ES]: Enzyme-substrate complex concentration

- $V_{\max} = k_2[E_T]$: Maximum velocity of product formation due to the limited enzyme amount
- $[E_T]$: Total enzyme concentration

In this system, the enzyme is adsorbed onto the surface, and the substrate diffuses toward the enzyme-covered surface. Upon collision, the enzyme–substrate complex is formed, which then leads to the production of the final product.

Diffusion is defined by Fick's second law[94]; it states that species move from regions of high concentration to regions of low concentration. The mathematical description of diffusion is given by:

$$\frac{\partial C(x,t)}{\partial t} = D\frac{\partial^2 C(x,t)}{\partial x^2} \tag{1.84}$$

Now, as time passes, the concentration of substrate depends on two factors: first, the diffusion of the substrate, and second, the rate of the enzymatic reaction. This behavior can be expressed mathematically as:

$$\frac{\partial C_s}{\partial t} = D\frac{\partial^2 C_s}{\partial x^2} - \frac{V_{\max} C_s}{K_m + C_s} \tag{1.85}$$

$$\frac{\partial C_p}{\partial t} = D\frac{\partial^2 C_p}{\partial x^2} + \frac{V_{\max} C_s}{K_m + C_s} \tag{1.86}$$

Equations (1.85) and (1.86) describe a chemical process governed by enzymatic activity. These two partial differential equations are coupled and must be solved simultaneously using the Newman method.

Before moving on to the numerical solution, these equations will be non-dimensionalized. Non-dimensionalization involves scaling all variables with appropriate characteristic values to remove physical units from the equations. This

results in a unitless form of the model, making it more general and simplifying the computational process.

The non-dimensional variables introduced are:

- t^* : dimensionless time
- x^* : dimensionless spatial coordinate
- C_s^* : dimensionless substrate concentration
- C_p^* : dimensionless product concentration

$$t = \frac{t^* L^2}{D_s}, \quad C_s = C_s^* K_m, \quad C_p = C_p^* K_m, \quad x = x^* L$$

Substituting t^*, C_s^*, C_p^*, x^* into equations (1.85) and (1.86) gives:

$$\left(\frac{D_s K_m}{L^2}\right) \frac{\partial C_s^*}{\partial t^*} = \left(\frac{D_s K_m}{L^2}\right) \frac{\partial^2 C_s^*}{\partial (x^*)^2} - \frac{V_{\max} C_s^* K_m}{K_m + C_s^* K_m} \tag{1.87}$$

$$\left(\frac{D_p K_m}{L^2}\right) \frac{\partial C_p^*}{\partial t^*} = \left(\frac{D_p K_m}{L^2}\right) \frac{\partial^2 C_p^*}{\partial (x^*)^2} + \frac{V_{\max} C_s^* K_m}{K_m + C_s^* K_m} \tag{1.88}$$

So,

$$\frac{\partial C_s^*}{\partial t^*} = \frac{\partial^2 C_s^*}{\partial (x^*)^2} - \left(\frac{L^2 V_{\max}}{D_s K_m}\right) \frac{C_s^*}{1 + C_s^*} \tag{1.89}$$

$$\frac{\partial C_p^*}{\partial t^*} = \frac{\partial^2 C_p^*}{\partial (x^*)^2} + \left(\frac{L^2 V_{\max}}{D_p K_m}\right) \frac{C_s^*}{1 + C_s^*} \tag{1.90}$$

Defining Thiele modulus:

$$\phi_s = L\sqrt{\frac{V_{\max}}{D_s K_m}}, \quad \phi_p = L\sqrt{\frac{V_{\max}}{D_p K_m}} \tag{1.91}$$

Now simplified and non-dimensionalized forms of equations (1^*) and (2^*) are:

The dimensionless time-dependent governing equations are:

$$\frac{\partial C_s^*}{\partial t^*} = \frac{\partial^2 C_s^*}{\partial (x^*)^2} - \frac{\phi_s^2 C_s^*}{1 + C_s^*} \tag{1.92}$$

$$\frac{\partial C_p^*}{\partial t^*} = \frac{\partial^2 C_p^*}{\partial (x^*)^2} + \frac{\phi_p^2 C_s^*}{1 + C_s^*} \tag{1.93}$$

These two coupled partial differential equations can be solved either time-dependently or time-independently. The time-independent solutions are referred to as steady-state solutions.

Steady-state analysis involves removing the time dependence from a partial differential equation (PDE) by assuming that the system has reached equilibrium, or a constant state over time. As a result, steady-state solutions describe how the concentrations vary in space, but not how they change over time.

$$\frac{\partial C_s^*}{\partial t^*} = 0 \tag{1.94}$$

Substituting this into Equation (1.92), we get:

$$\frac{\partial^2 C_s^*}{\partial (x^*)^2} - \frac{\phi_s^2 C_s^*}{1 + C_s^*} = 0 \tag{1.95}$$

Multiplying both sides by $(1 + C_s^*)$:

$$(1 + C_s^*)\frac{\partial^2 C_s^*}{\partial (x^*)^2} - \phi_s^2 C_s^* = 0 \tag{1.96}$$

This is now a second-order nonlinear ordinary differential equation (ODE) in space only.

Now the time-independent (steady-state) equations become:

$$(1 + C_s^*)\frac{\partial^2 C_s^*}{\partial (x^*)^2} - \phi_s^2 C_s^* = 0 \tag{1.97}$$

$$(1 + C_s^*)\frac{\partial^2 C_p^*}{\partial (x^*)^2} + \phi_p^2 C_s^* = 0 \tag{1.98}$$

In Chapter 1.3.2, the linearization of PDEs was explained. In parallel to that approach, the following two nonlinear equations are linearized. The parameters to be linearized are C_s^* and C_p^*:

$$C_p^* = C_{p,\text{old}}^* + \Delta C_p \tag{1.99}$$

$$C_s^* = C_{s,\text{old}}^* + \Delta C_s \tag{1.100}$$

Here, ΔC_p and ΔC_s represent infinitesimal changes in C_p^* and C_s^*, respectively. Upon substitution into the steady-state equations, the system becomes:

$$(1 + C_{s,\text{old}}^* + \Delta C_s)\frac{\partial^2}{\partial (x^*)^2}(C_{s,\text{old}}^* + \Delta C_s) - \phi_s^2 (C_{s,\text{old}}^* + \Delta C_s) = 0 \tag{1.101}$$

$$(1 + C_{s,\text{old}}^* + \Delta C_s)\frac{\partial^2}{\partial (x^*)^2}(C_{p,\text{old}}^* + \Delta C_p) + \phi_p^2 (C_{s,\text{old}}^* + \Delta C_s) = 0 \tag{1.102}$$

Equation (1.101) becomes, after substitution and expansion:

$$\begin{aligned}&\frac{\partial^2 C_{s,\text{old}}^*}{\partial (x^*)^2} + \frac{\partial^2 \Delta C_s}{\partial (x^*)^2} + C_{s,\text{old}}^* \frac{\partial^2 C_{s,\text{old}}^*}{\partial (x^*)^2} + C_{s,\text{old}}^* \frac{\partial^2 \Delta C_s}{\partial (x^*)^2} \\ &+ \Delta C_s \frac{\partial^2 C_{s,\text{old}}^*}{\partial (x^*)^2} + \Delta C_s \frac{\partial^2 \Delta C_s}{\partial (x^*)^2} - \phi_s^2 C_{s,\text{old}}^* - \phi_s^2 \Delta C_s = 0\end{aligned} \tag{1.103}$$

Nonlinear terms such as :

$$\Delta C_s \frac{\partial^2 \Delta C_s}{\partial (x^*)^2}$$

are neglected in the linearization process.

After expansion and grouping the unknown terms, equation (1.101) becomes:

$$(1 + C^*_{s,\text{old}}) \frac{\partial^2 \Delta C_s}{\partial (x^*)^2} + \left(\frac{\partial^2 C^*_{s,\text{old}}}{\partial (x^*)^2} - \phi_s^2 \right) \Delta C_s = - \left((1 + C^*_{s,\text{old}}) \frac{\partial^2 C^*_{s,\text{old}}}{\partial (x^*)^2} - \phi_s^2 C^*_{s,\text{old}} \right) \tag{1.104}$$

Similarly, the linearized version of equation (1.102) is:

$$(1 + C^*_{s,\text{old}}) \frac{\partial^2 \Delta C_p}{\partial (x^*)^2} + \left(\frac{\partial^2 C^*_{p,\text{old}}}{\partial (x^*)^2} + \phi_p^2 \right) \Delta C_s = - \left((1 + C^*_{s,\text{old}}) \frac{\partial^2 C^*_{p,\text{old}}}{\partial (x^*)^2} + \phi_p^2 C^*_{s,\text{old}} \right) \tag{1.105}$$

The left-hand sides of equations (1.104) and (1.105) contain the unknowns ΔC_s and ΔC_p, and will form the elements of the system matrix to be solved. The right-hand sides consist of known quantities and will constitute the constant (source) vector in the matrix formulation.

Before constructing the coefficient matrix, we must perform back substitution in order to compute the updated values of C_s and C_p.

Using the definitions:

$$\Delta C_s = C^*_s - C^*_{s,\text{old}} \tag{1.106}$$

$$\Delta C_p = C^*_p - C^*_{p,\text{old}} \tag{1.107}$$

and substituting back into the linearized equations, we obtain:

$$(1 + C^*_{s,\text{old}})\frac{\partial^2 C^*_s}{\partial (x^*)^2} + \left(\frac{\partial^2 C^*_{s,\text{old}}}{\partial (x^*)^2} - \phi_s^2\right) C^*_s = \frac{\partial^2 C^*_{s,\text{old}}}{\partial (x^*)^2} C^*_{s,\text{old}} \tag{1.108}$$

$$(1 + C^*_{s,\text{old}})\frac{\partial^2 C^*_p}{\partial (x^*)^2} + \left(\frac{\partial^2 C^*_{p,\text{old}}}{\partial (x^*)^2} + \phi_p^2\right) C^*_s = \frac{\partial^2 C^*_{p,\text{old}}}{\partial (x^*)^2} C^*_{s,\text{old}} \tag{1.109}$$

The general form of a linearized second-order PDE in Newman's notation is:

$$\sum_k \left(a_k \frac{\partial^2 c_k}{\partial x^2} + b_k \frac{\partial c_k}{\partial x} + d_k c_k\right) = g \tag{1.110}$$

where:

- a_k, b_k, and d_k are coefficient functions depending on space (and possibly previous iteration values),
- c_k are the unknowns (e.g., C^*_s, C^*_p),
- g is the known right-hand-side function.

Here, the coefficients of the linearized equations are organized in Newman's band matrix form:

	a	**b**	**d**	**g**
$\boldsymbol{C^*_s}$	$(1 + C^*_{s,\text{old}})$	0	$\frac{\partial^2 C^*_{s,\text{old}}}{\partial (x^*)^2} - \phi_s^2$	$\frac{\partial^2 C^*_{s,\text{old}}}{\partial (x^*)^2} C^*_{s,\text{old}}$
$\boldsymbol{C^*_p}$	0	0	0	0

Table 1.1: Coefficient matrix structure for the non-dimensionalized linearized form of equation (1.85) in Newman notation.

Now, the coefficient matrices namely $\mathbf{sm}_a$, $\mathbf{sm}_b$, $\mathbf{sm}_d$, and $\mathbf{sm}_g$ for the parameters (C^*_s, C^*_p) can be constructed as:

	a	**b**	**d**
$\boldsymbol{C_s^*}$	0	0	$\frac{\partial^2 C^*_{p,\text{old}}}{\partial (x^*)^2} + \phi_p^2$
$\boldsymbol{C_p^*}$	$(1 + C^*_{s,\text{old}})$	0	0

Table 1.2: Coefficient matrix structure for the non-dimensionalized and linearized form of equation (1.86) in Newman notation.

$$\mathbf{sm}_a = \begin{bmatrix} (1 + C^*_{s,\text{old}}) & 0 \\ 0 & (1 + C^*_{s,\text{old}}) \end{bmatrix}$$

$$\mathbf{sm}_b = \begin{bmatrix} 0 & 0 \\ 0 & 0 \end{bmatrix}$$

$$\mathbf{sm}_d = \begin{bmatrix} \frac{\partial^2 C^*_{s,\text{old}}}{\partial (x^*)^2} - \phi_s^2 & 0 \\ \frac{\partial^2 C^*_{p,\text{old}}}{\partial (x^*)^2} + \phi_p^2 & 0 \end{bmatrix}$$

$$\mathbf{sm}_g = \begin{bmatrix} \frac{\partial^2 C^*_{s,\text{old}}}{\partial (x^*)^2} \cdot C^*_{s,\text{old}} \\ \frac{\partial^2 C^*_{p,\text{old}}}{\partial (x^*)^2} \cdot C^*_{s,\text{old}} \end{bmatrix}$$

There only remains the construction of the boundary matrices. Boundary condition 1 is applied at $x^* = 0$, and boundary condition 2 is applied at $x^* = 1$.

At $x^* = 0$:

$$\frac{\partial C_s^*}{\partial x^*} = 0, \qquad C_p^* = 0$$

At $x^* = 1$:

$$C_s^* = \frac{C_{s,\text{bulk}}}{K_m}, \qquad C_p^* = 0$$

Newman's general boundary condition form is given as:

$$\sum_k \left(p_k \frac{\partial c_k}{\partial x} + e_k c_k \right) = f$$

At $x^* = 0$

Equation: $\frac{\partial C_s^*}{\partial x^*} = 0$	**p**	**e**	**f**
C_s^*	1	0	0
C_p^*	0	0	

Equation: $C_p^* = 0$	**p**	**e**	**f**
C_s^*	0	0	0
C_p^*	0	1	

$$\mathbf{sm}_p = \begin{bmatrix} 1 & 0 \\ \\ 0 & 0 \end{bmatrix}, \quad \mathbf{sm}_e = \begin{bmatrix} 0 & 0 \\ \\ 0 & 1 \end{bmatrix}, \quad \mathbf{sm}_f = \begin{bmatrix} 0 \\ \\ 0 \end{bmatrix}$$

At $x^* = 1$

Equation: $C_s^* = \dfrac{C_{s,\text{bulk}}}{K_m}$	**p**	**e**	**f**
C_s^*	0	1	$\dfrac{C_{s,\text{bulk}}}{K_m}$
C_p^*	0	0	

Equation: $C_p^* = 0$	**p**	**e**	**f**
C_s^*	0	0	0
C_p^*	0	1	

$$\mathbf{sm}_p = \begin{bmatrix} 0 & 0 \\ & \\ 0 & 0 \end{bmatrix}, \quad \mathbf{sm}_e = \begin{bmatrix} 1 & 0 \\ & \\ 0 & 1 \end{bmatrix}, \quad \mathbf{sm}_f = \begin{bmatrix} \dfrac{C_{s,\text{bulk}}}{K_m} \\ \\ 0 \end{bmatrix}$$

These matrices are the sub-coefficient matrices calculated separately for each spatial point in the two coupled equations. In other words, if the solution is to be computed for 100 spatial points, then 100 individual matrices are generated for each of $\mathbf{sm}_a$, $\mathbf{sm}_b$, $\mathbf{sm}_d$, and $\mathbf{sm}_g$.

By incorporating these matrices into the numerical code, the system is iteratively solved to obtain the steady-state solution.

This simulation represents a steady-state, time-independent model. The x-axis denotes the distance along the electrode, while the y-axis indicates concentration (Figure 1.7). Starting with the substrate profile, we observe that for a certain region, the substrate concentration remains constant at zero. This can be attributed to the rapid formation of the [ES] complex. In the Michaelis-Menten mechanism, it is generally accepted that the binding step is fast. Therefore, there is no rate-limiting step at this stage, and the [ES] complex forms quickly.

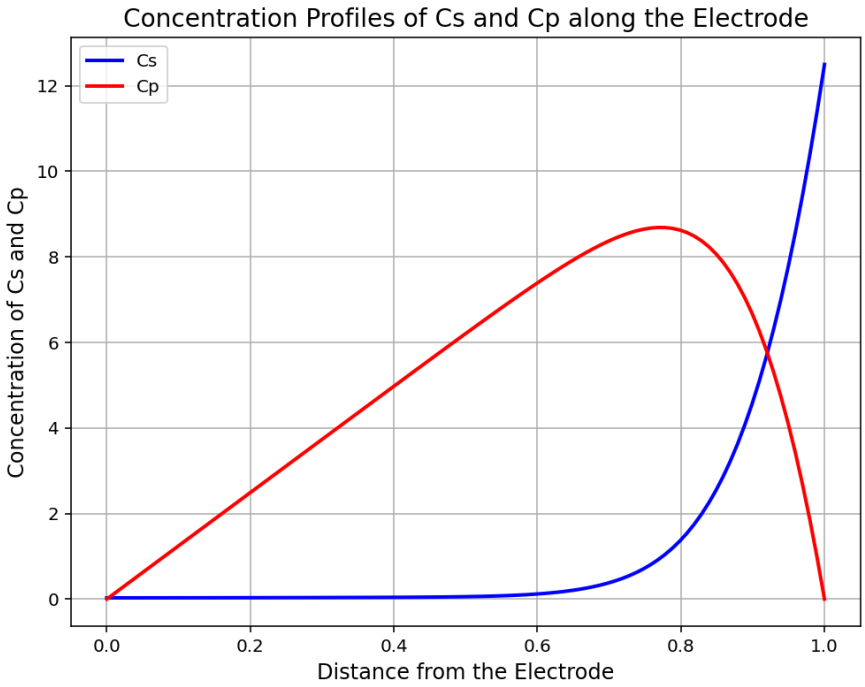

Figure 1.7: Concentration evolution of reactant and product across the electrode, simulated using Python.

Similarly, product formation increases almost linearly up to a certain point and then reaches a peak. The region where Cs drops sharply indicates the most active reaction zone, where the substrate is rapidly converted into the product. At the beginning of the electrode, Cp is zero, increases toward the middle, reaches a maximum, and then declines. This suggests that the product is formed in the region where the substrate becomes depleted. As we move away from the electrode surface, the substrate concentration approaches the bulk concentration. Substrate diffusion occurs from right to left, while product diffusion occurs from left to right. The point at which Cp reaches its maximum corresponds to a region slightly beyond the main reaction zone, where the product accumulates. In this region, all active enzyme sites are saturated, and the reaction reaches its maximum rate.

1.11 Modelling of Electrochemical Systems: Nernst-Planck-Poisson and electroneutrality approximation

In modeling electrochemical polymer systems, five fundamental state variables are typically required: (i) the concentrations of counter-ions, C_+ and C_-, (ii) the Faradaic charge accumulated within the conducting polymer phase at oxidizing potentials, Q_F, (iii) the solid-phase potential, Φ_1, and (iv) the electrolyte potential, Φ_2. Since the system involves five unknowns, at least five independent governing equations are needed[99].

The first two equations arise from the mobility of counter-ions. In p-doping systems such as PEDOT, the polymer becomes conductive at positive potentials, i.e., when electrons are withdrawn from the polymer backbone leaving behind positively charged carriers (holes). To preserve charge neutrality under these conditions, negatively charged ions from the electrolyte penetrate the polymer phase. Conversely, when the potential is driven negative, these anions are expelled[101]. Thus, ion doping–dedoping operates in concert with electron transfer, ensuring overall charge balance. In the absence of convection, the ionic fluxes are described by the Nernst–Planck equations for mass transport, which together with the principle of conservation of mass yield the governing equations for C_+ and C_-.

$$\mathbf{J}_i = -D_i \left(\nabla C_i + \frac{z_i F}{RT} C_i \nabla \phi \right) \tag{1.111}$$

where

- $\mathbf{J}_i$: flux of species i ($\mathrm{mol \cdot m^{-2} \cdot s^{-1}}$),
- D_i : diffusion coefficient of species i ($\mathrm{m^2/s}$),
- C_i : concentration of species i ($\mathrm{mol/m^3}$),

- z_i : charge number of species i (dimensionless),
- F : Faraday constant (96,485 C/mol),
- R : universal gas constant (8.314 J/mol·K),
- T : absolute temperature (K),
- ϕ : electrostatic potential (V),
- ∇ : spatial gradient operator.

$$\frac{\partial C_i}{\partial t} = -\nabla \cdot \mathbf{J}_i = D_i \nabla \cdot \left(\nabla C_i + \frac{z_i F}{RT} C_i \nabla \phi \right) \tag{1.112}$$

The third governing equation corresponds to Q_F and is obtained from electrochemical kinetics, typically expressed through the Butler–Volmer formalism. The fourth equation is related to the solid-phase potential Φ_1, which follows from the balance between potential distribution, electronic conductivity, and the divergence of the electronic current. This divergence equals the interfacial reaction current density, thereby linking charge transport within the solid to the Faradaic processes at the polymer electrolyte boundary.

The fifth and final governing equation must describe the charge distribution in the electrolyte phase. Two approaches are possible: (i) the charge neutrality approximation or (ii) the Poisson equation. The charge neutrality condition assumes that the sum of ionic charges in the electrolyte is strictly zero, i.e., no charge separation exists in the bulk. This condition is, in fact, a limiting form of the Poisson equation [102].Starting from Gauss's law, the charge density is defined by the ionic species in the electrolyte, leading directly to the Poisson equation:

$$\nabla^2 \phi = -\frac{\rho}{\varepsilon_s \varepsilon_0} \tag{1.113}$$

$$\nabla^2\phi + \frac{F}{\varepsilon_s\varepsilon_0}\sum_i z_i C_i = 0 \tag{1.114}$$

where

- ϕ : electrostatic potential (V),
- ∇^2 : Laplacian operator (spatial second derivative),
- F : Faraday constant (96,485 C/mol),
- ε_s : relative permittivity (dielectric constant) of the solvent,
- ε_0 : vacuum permittivity (8.854×10^{-12} F/m),
- z_i : charge number of ionic species i (dimensionless),
- C_i : concentration of ionic species i (mol/m^3).

$$2r_D^2\nabla^2\theta + \sum_i z_i c_i = 0 \tag{1.115}$$

which couples the electrostatic potential to the spatial distribution of charge. A dimensional analysis of the Poisson equation reveals that, in systems where the Debye length (r_D) approaches zero, the condition of local charge neutrality emerges as a valid approximation. Since the Debye length in typical electrochemical systems is on the nanometer scale, the electroneutrality assumption is often well justified and widely adopted in modeling [102].

1.12 Structure of this Thesis

This thesis is structured into six main chapters, each addressing a different aspect of the investigation, from theoretical foundations to experimental validation, modeling, and outlook.

Chapter 1 provides the introduction and theoretical background. It begins with a discussion of electron transfer in monolayer and multilayer films, followed by a comparison of different charge storage mechanisms revealed through cyclic voltammetry. The chapter further introduces conjugated polymers (CPs) and their oligomers, emphasizing their proposed charge transfer mechanisms, electrochromism, and the interplay between ion-coupled and ion-free transfer. The dual charge-transfer nature of CPs is then detailed, highlighting both faradaic and capacitive processes through diffusion layer theory and electrical double layer concepts. Finally, the chapter introduces the modeling frameworks, including coupled partial differential equations, the Nernst–Planck–Poisson approach, and the electrochemically active polymer model equations, before concluding with a summary of the thesis structure.

Chapter 2 describes the experimental work. It details the materials, electrode preparation, and electro-polymerization procedures, as well as the electrochemical techniques employed, including cyclic voltammetry, ultrafast CV, chronoamperometry, chronopotentiometr. The chapter also presents the spectroelectrochemical methods, such as operando UV–Vis spectroscopy and principal component analysis (PCA), alongside the setup of the electrochemical/optical cell, data acquisition strategies.

Chapter 3 presents the combined electrochemical and spectroelectrochemical results. It discusses operando UV–Vis/CV measurements of PEDOT films of varying thicknesses, sweep rate dependencies, b-value analyses, PCA of thin and thick films, and the extraction of optical coefficients to understand the sweep rate effect on charge transport and color change dynamics.

Chapter 4 is dedicated to the modeling aspects of electrochemical processes in conducting polymers. It explains the setup and linearization, the construction of coefficient matrices, and the numerical solution approaches applied to the model equations.

Chapter 5 summarizes the main conclusions of the study, consolidating the theoretical, experimental, and modeling insights into a coherent understanding

of charge transfer in conjugated polymers.

Finally, Chapter 6 outlines perspectives for future work.

Chapter 2

EXPERIMENTAL

2.1 Materials

The materials used in this study include 3,4-Ethylenedioxythiophene (EDOT, Sigma-Aldrich), Tetrabutylammonium hexafluorophosphate ($TBAHPF_6$, 98%, powder, Sigma-Aldrich) as the supporting electrolyte, and Acetonitrile (Sigma-Aldrich, 99.9%, analytical grade) as the solvent. Fluorine-doped tin oxide (FTO) coated glass electrodes (Aldrich), graphite electrode, and silver wire (Alfa Aesar, 1.0 mm diameter, 99.9%) were used for electrochemical measurements.

2.2 Electrode Preparation and Electro-polymerization

2.2.1 Cleaning and Coating the electrode

The FTO coated glass electrodes are cleaned through ultrasonication in the following sequence: first, in de-ionized water, then alcohol, and finally in acetone, with each step lasting for 10 minutes. After drying, they are coated with epoxy, as illustrated below. Prior to electro-polymerization, the epoxy coating is allowed to

cure for one day. The epoxy coating ensures that the PEDOT layer forms only in the desired area and shape.Figure 2.1 shows the FTO glass electrode before and after polymer coating, where the conductive circular area was defined by an epoxy mask and subsequently covered with the polymer through electropolymerization.

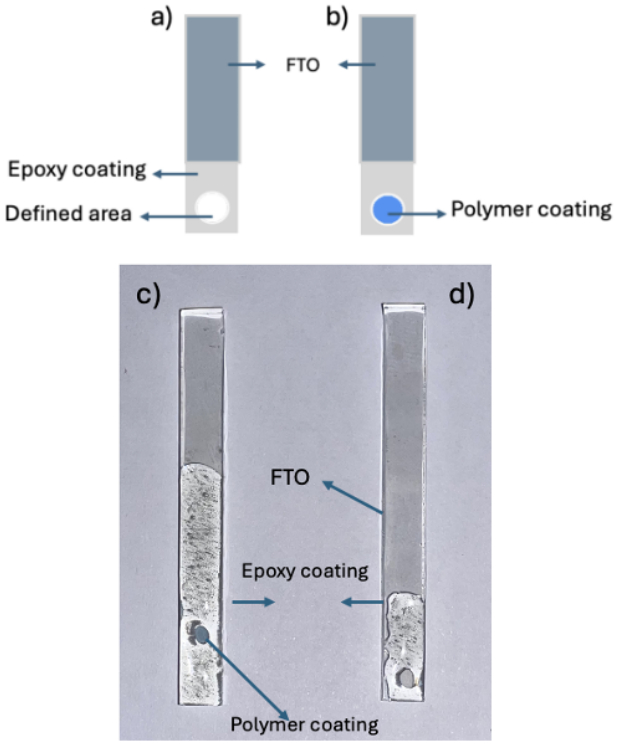

Figure 2.1: a) FTO glass electrode before polymer coating. The circular area was created by coating the surface with epoxy, so that only the remaining circular area is conductive, and electropolymerization will occur here. b) After electropolymerization.

2.2.2 Electropolymerization

A 0.1 M Tetrabutylammonium hexafluorophosphate solution is prepared using acetonitrile in a 25 mL volumetric flask. Then, a 25 mM solution of 3,4-Ethylenedioxythiophene (EDOT), an electroactive conductive monomer, is prepared. Molecular sieves are also added. Afterward, clean FTO glass electrodes,

coated with epoxy, are placed in the monomer solution, ensuring that the conductive circular area remains in contact with the solution. The FTO glass electrode is used as the working electrode, a graphite rod electrode serves as the counter electrode, and a silver wire is placed as the reference electrode in the solution. Chronopotentiometry is performed with a current of 5 mA, and the time is varied at different lengths (e.g., 0.01, 0.1, 1, 10 s), to prepare electrodes with varying coating thicknesses.

2.3 Electrochemical methods

In this study, the electrochemical methods used, from preparation to measurements, are summarized and categorized under subheadings according to their purpose. The methods employed include Chronopotentiometry, Spectrochronoamperometry, Spectro-Cyclic Voltammetry (CV) (0.1 V/s to 1 V/s), Spectro-Ultrafast CV (1 V/s to 150,000 V/s), and finally, Electrochemical Impedance Spectroscopy (EIS). Electrochemical experiments in the range of 0.1 V/s to 1 V/s were performed using a commercial potentiostat (Gamry Interface 1000E, Gamry Instruments). In situ UV–Vis measurements were carried out with a Gamry UV–Vis fiber-optic spectrophotometer (Gamry Instruments) in a 12.5 × 12.5 × 45 mm quartz cuvette (ISO LAB, ES quartz). Ultrafast cyclic voltammetry experiments were performed using a custom-designed potentiostat developed in our laboratory. The details of the ultrafast cyclic voltammetry design, the circuit scheme, and the implementation of IR compensation have been described in previous studies [103].

2.3.1 Chronopotentiometry

Chronopotentiometry, as the name suggests, is a time-dependent potential measurement technique. In this measurement, a constant current is applied to the system, and the potential response of the system is observed over time. Technically, this method controls the current between the working and counter electrodes,

while the potential between the working and reference electrodes is recorded. As described in the introduction to control-current measurements, the theory behind this technique is derived from diffusion control. While a constant current is applied to the electrode, electrochemical transformations continue at the electrode surface until the system reaches a mass transport limitation. During this period, the electrode potential changes continuously [82].

At time $t = 0$, when no current has yet been applied, the potential of the electrode is constant. At $t > 0$, for instance, when a 5 mA current is applied, oxidation reaction begins, and the potential shifts to more positive values. Initially, the reaction proceeds rapidly as the electroactive species diffuses to the electrode surface and is oxidized. As time progresses, the potential continues to shift, but the rate of change becomes slower due to the concentration gradient at the surface. The potential will eventually approach a steady-state value, where it no longer changes significantly with time. This steady state indicates that the diffusion of electroactive species to the electrode surface is balanced by the consumption of those species during the electrochemical reaction. Figure 2.2 shows the chronopotentiometric response, where the applied constant current leads to a potential shift over time that approaches a steady-state value as diffusion and consumption of electroactive species reach equilibrium.

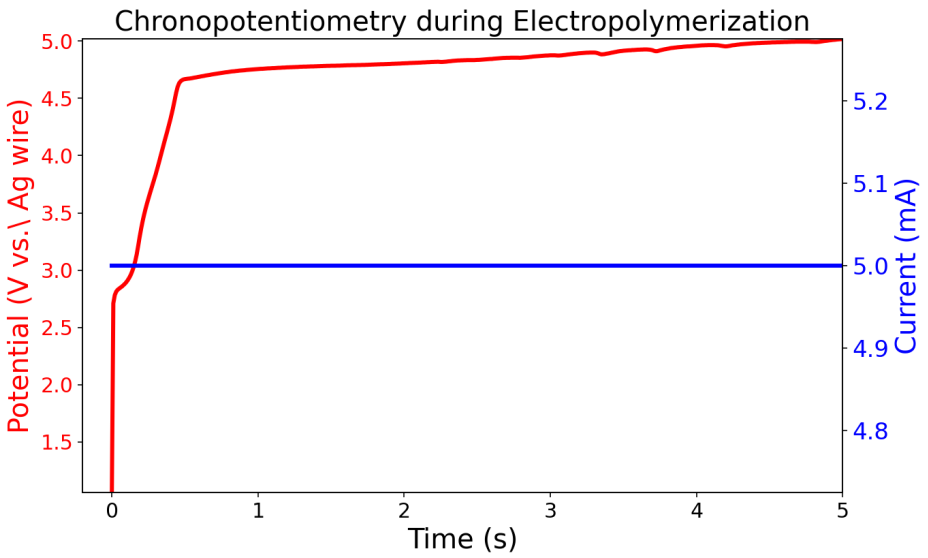

Figure 2.2: Chronopotentiometric response showing the potential shift over time as a constant current is applied, with the potential approaching a steady-state value as diffusion and consumption of electroactive species reach equilibrium.

2.3.2 Spectro-Chronoamperometry

In spectrochronoamperometry, a constant potential is applied to the polymer in the range of -0.4, -0.3, -0.2, -0.1, 0.0, 0.1, 0.2, 0.3, 0.4, 0.5, and 0.6 V. The polymer is held at each of these potentials for 10 seconds, and immediately afterward, UV-VIS measurements are taken to monitor the response of the polymer at each potential.

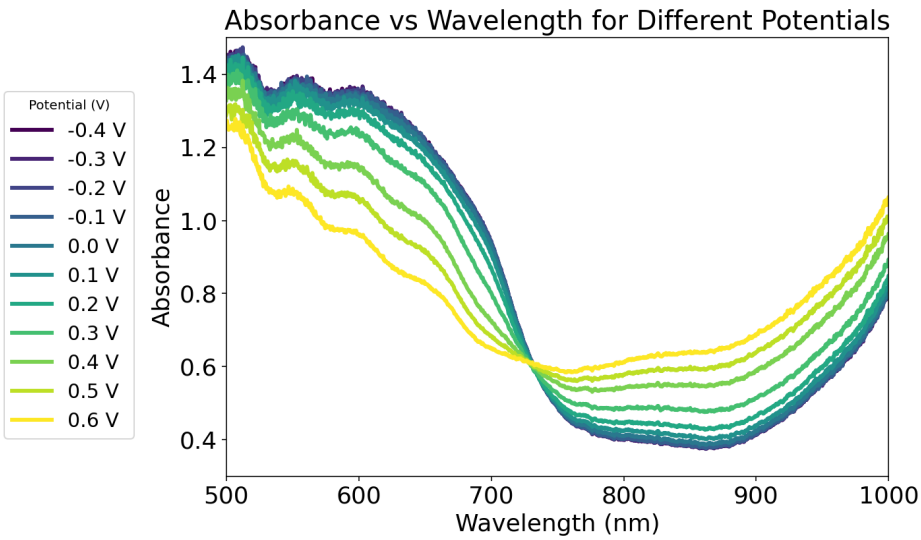

Figure 2.3: Spectrochronoamperometric measurement of polymer absorbance at various applied potentials, used to select a signature wavelength for reconstructing the forward cyclic voltammetry curve.

This data will then be used to select a signature wavelength for reconstructing a forward cyclic voltammetry (CV) curve by analyzing the absorbance at that specific wavelength.

2.3.3 Spectro Cyclic Voltammetry and Ultrafast Cyclic Voltammetry Measurements

In its simplest form, our system's spectroelectrochemistry experiments rely on simultaneous cyclic voltammetry and UV-VIS measurements taken at different scan rates.

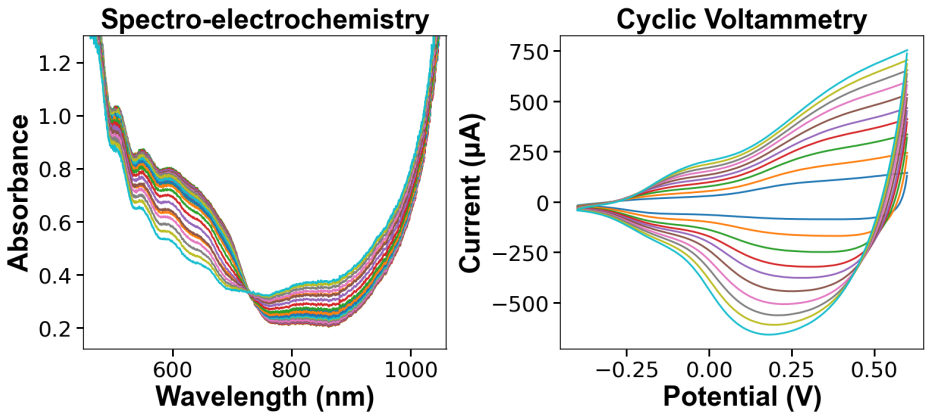

Figure 2.4: Representative simultaneous absorbance vs. wavelength data (left) and corresponding cyclic voltammetry measurements (right).

2.3.3.1 Preparation of the Electrochemical/Optical Cell

A three-electrode system is used. As the electrolyte, 0.1 M Tetrabutylammonium hexafluorophosphate solution is prepared, with acetonitrile as the solvent. The PEDOT polymer-coated FTO electrode serves as the working electrode, while a graphite rod acts as the counter electrode and a silver wire functions as the reference electrode. The system is set up in a quartz cuvette for optical measurements (3.5 ml macro size). The electrodes are placed in the cuvette such that they do not move. The cuvette is positioned in an optical holder with fiber optic cable attachments on both sides. Figure 2.5b.

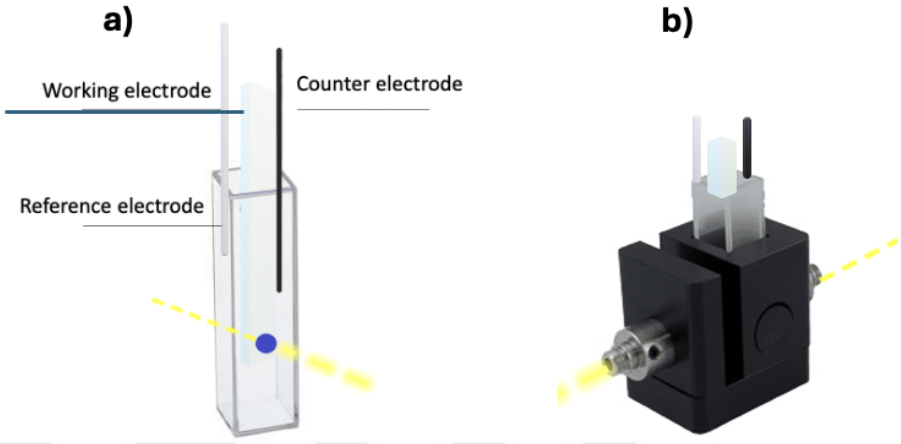

Figure 2.5: Schematic representation of the three-electrode system setup for spectroelectrochemical measurements, with optical holder placement for UV-VIS measurements.

2.3.3.2 Data Acquisition during Spectro-CV and Averaging the Spectra

For SpectroCV measurements, the system is allowed to reach a steady state with no applied voltage. After measuring the open circuit potential (OCP), the actual measurements begin. The sweep rate for the measurement is determined, and the OCP voltage is applied as the conditioning voltage to the system (Figure2.6a1). While the polymer is held at this conditioning voltage, spectroscopic measurements are taken (Figure(2.5a2), which we refer to as the conditioning or before cycling measurements. Following this, the voltage begins to change according to the sweep rate, typically ranging from -0.4 V to +0.4 V.(Figure2.5b1). This voltage range is chosen to minimize polymer degradation after multiple cycles and to ensure optimum measurements. Other voltage ranges, such as -0.4 V to +0.6 V, can also be used, with color change still observed.

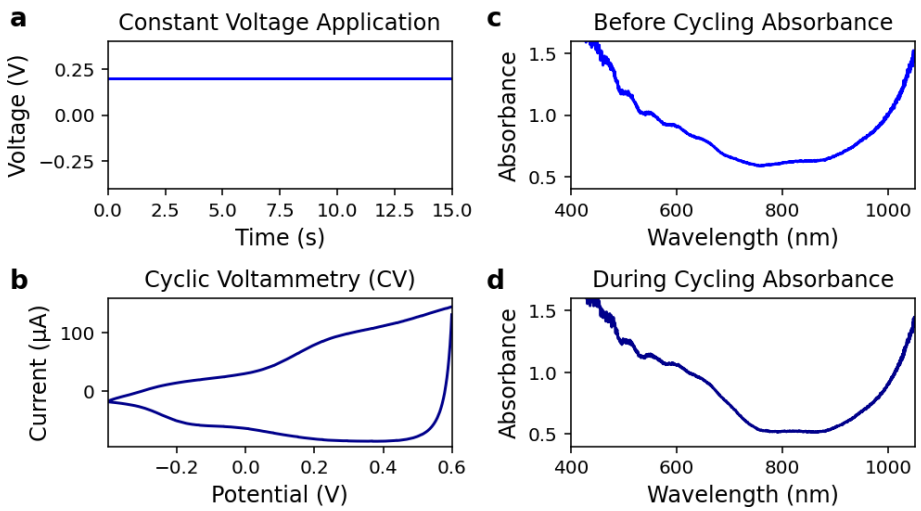

Figure 2.6: Schematic overview of the SpectroCV measurement process: (a) system conditioning at the open circuit potential (OCP), (c) conditioning or before cycling spectroscopic measurements, (b) voltage sweep from -0.4 V to +0.4 V, and (d) observed color change during the measurement.

During the voltage sweep, 1000 spectra are collected within 30 seconds, averaged, and presented as one spectrum (Figure2.7). This process is repeated three times, corresponding to three cycles of the polymer, lasting a total of 1 minute and 30 seconds. Each cycling spectrum, containing the average of 1000 spectra, is identical.

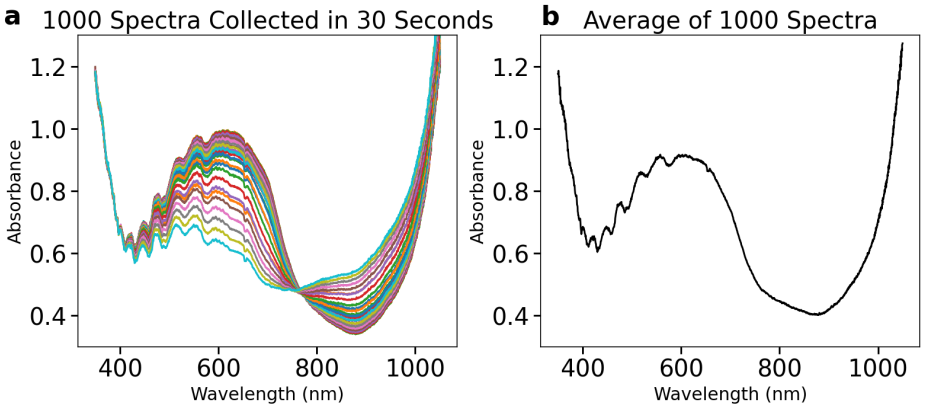

Figure 2.7: Averaged spectrum obtained from 1000 spectra collected within 30 seconds (a) during the voltage sweep, repeated over three cycles of the polymer.

2.4 Principal Component Analysis

As a result of data acquisition, we obtain one before cycling spectrum and one during cycling spectrum (Figure 2.6). The spectrum labeled as the average of 1000 spectra represents the mean absorbance versus wavelength obtained during cycling. Since analyzing the system's response at varying scan rates is difficult with this single spectrum, it is decomposed into its components, and the changes of these components relative to the before cycling components are examined. The first step in this process is to determine how many components are needed. Principal Component Analysis (PCA) is employed for this purpose. For the analysis, the basis set, before cycling, and during cycling absorbance data are compiled into an excel file, where each column represents an absorbance measurement.

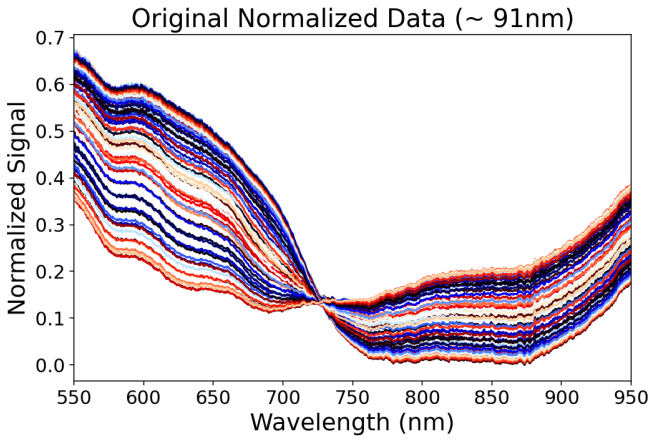

Figure 2.8: Normalized absorbance spectra of the polymer film recorded between 550–950 nm. Each curve corresponds to a different time step during the potential sweep, and all data are normalized for comparability.

In the second step, these values are normalized (Figure 2.8) by finding the lowest absorbance value among all columns and subtracting it from every column, ensuring that all values become positive. In other words, all spectra are normalized by subtracting the minimum value [104].

Then covariance matrix is calculated to determine the correlations between

variables. The eigenvalues of the covariance matrix indicate the amount of information (variance) carried by each principal component (PC), while the eigenvectors define the directions of these components in the original data space (Figure 2.9).

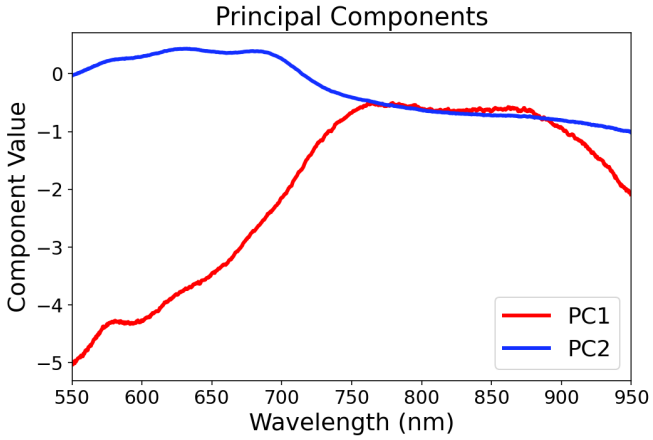

Figure 2.9: Principal components (PC1, PC2, ...) extracted from the normalized absorbance data. Each component corresponds to a direction of maximum variance in the dataset.

The resulting scores (X_{PCA}) represent the projection of the data in the principal component space. The reconstruction error (2.10) is used to determine the minimum number of PCs required to describe the data with sufficient accuracy [104].

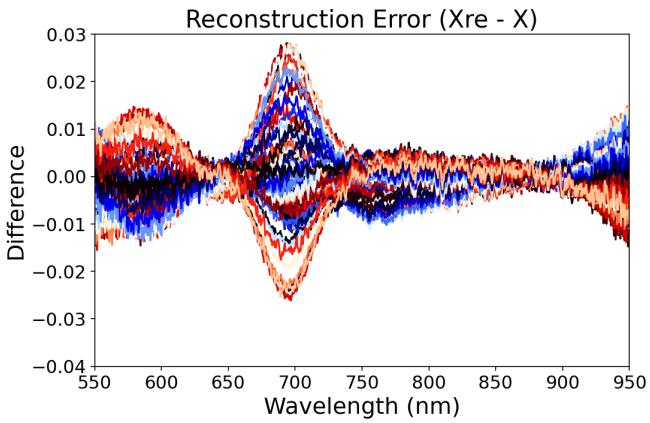

Figure 2.10: Reconstruction error obtained by subtracting the original normalized spectra from the data reconstructed using the selected principal components. The small difference indicates that the chosen components are sufficient to represent the dataset.

By providing a small dataset and performing Principal Component Analysis (PCA), we observe that a three-dimensional vector space can be effectively represented by two vectors, since two of the original vectors are linearly dependent.

2.4.1 PCA on a small dataset (step by step)

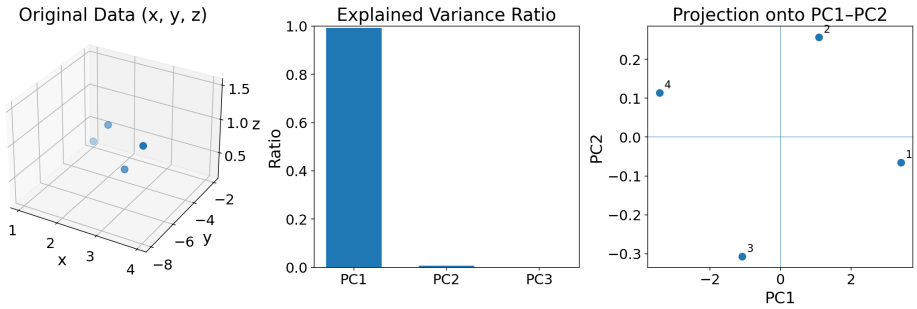

Figure 2.11: Illustration of principal component analysis (PCA). (a) Original dataset in three dimensions. (b) New orthogonal axes PC1 and PC2 indicating the directions of maximum variance. (c) Data projected into the PC1–PC2 space.

Given three variables with $n = 4$ measurements

$$x = \{1, 2, 3, 4\}, \quad y = \{-2, -4, -6, -8\}, \quad z = \{0.2,\ 0.9,\ 0.7,\ 1.5\},$$

form the data matrix (rows = Measurements, columns = variables)

Centering is performed by subtracting the mean of each vector from its individual variables, rather than subtracting the minimum value.

$$X = \begin{bmatrix} 1 & -2 & 0.2 \\ 2 & -4 & 0.9 \\ 3 & -6 & 0.7 \\ 4 & -8 & 1.5 \end{bmatrix}, \qquad \boldsymbol{\mu} = \frac{1}{n}\sum_{i=1}^{n} X_{i,:} = \begin{bmatrix} 2.5 & -5 & 0.825 \end{bmatrix}.$$

Mean-center the data:

$$X_c = X - \boldsymbol{\mu} = \begin{bmatrix} -1.5 & 3 & -0.625 \\ -0.5 & 1 & 0.075 \\ 0.5 & -1 & -0.125 \\ 1.5 & -3 & 0.675 \end{bmatrix}.$$

Then comes the covariance matrix. The **covariance matrix** is a square matrix that contains the covariances between pairs of variables in a dataset. Each element of the matrix represents how two variables vary together[104]:

$$\mathbf{C} = \begin{bmatrix} \operatorname{cov}(X_1, X_1) & \operatorname{cov}(X_1, X_2) & \cdots & \operatorname{cov}(X_1, X_n) \\ \operatorname{cov}(X_2, X_1) & \operatorname{cov}(X_2, X_2) & \cdots & \operatorname{cov}(X_2, X_n) \\ \vdots & \vdots & \ddots & \vdots \\ \operatorname{cov}(X_n, X_1) & \operatorname{cov}(X_n, X_2) & \cdots & \operatorname{cov}(X_n, X_n) \end{bmatrix} \tag{2.1}$$

where the covariance between variables X_i and X_j is defined as "The covariance between two variables X_i and X_j is calculated as the expected value of the product of their deviations from their respective means:

$$\operatorname{cov}(X_i, X_j) = \frac{1}{N-1} \sum_{k=1}^{N} \left(x_{i,k} - \bar{x}_i\right) \left(x_{j,k} - \bar{x}_j\right) \tag{2.2}$$

where:

- $x_{i,k}$ and $x_{j,k}$ are the k-th observations of variables X_i and X_j,
- $\bar{x}_i$ and $\bar{x}_j$ are the sample means of X_i and X_j,
- N is the total number of measurements.

After computing the covariance matrix, an eigen-decomposition is performed, where the columns of V are the eigenvectors (principal component directions) and Λ is a diagonal matrix containing the corresponding eigenvalues. The magnitude of each eigenvalue λ_k indicates the variance of the data along its associated eigenvector direction. A larger eigenvalue means that the corresponding principal component explains a greater portion of the total variance in the dataset.

For the covariance matrix C:

$$C = V \Lambda V^{\top}$$

where:

- V: Each column represents a *principal component direction*,
- Λ: Diagonal matrix containing the variances along these directions,
- Not: If λ_1 is the largest eigenvalue, the first component explains the most variance.

Interpretation. Since $y = -2x$ exactly, the (x, y) subspace is rank-1; the second principal component captures the small independent variation in z ($r_2 \ll 1$), and the third component carries no variance ($\lambda_3 \approx 0$). Thus, two PCs suffice for exact reconstruction in this example.

Our Data Interpretation. In our dataset, the variance is dominated by a single principal component, while the second principal component accounts for only a small independent contribution. The third component carries negligible variance. Therefore, two principal components are sufficient to reconstruct the dataset with high accuracy.

Chapter 3

ELECTROCHEMISTRY AND SPECTROELECTROCHEMISTRY

In this chapter the experimental results will be examined in light of the well-established theories discussed in the introduction. Since conducting polymers facilitate electron transport through complex and interrelated mechanisms, their analysis was carried out using UV-VIS spectroscopy in conjunction with simultaneous cyclic voltammetry and ultrafast cyclic voltammetry techniques.

3.1 Cyclic Voltammetry Analysis

The analysis will first focus solely on cyclic voltammetry, and following the demonstration through experimental results that this technique alone is insufficient to fully capture the behavior of the system, the discussion will proceed with the presentation and analysis of spectroscopic data.

3.1.1 b-value Analysis

As discussed in the *Limitations of b-Value Analysis* section (1.3.4) in the introduction, the broad shape of the polymer's cyclic voltammograms complicates the analysis of peak current versus sweep rate. Moreover, the cyclic voltammetry response inherently includes contributions from both capacitive and redox currents, each possessing distinct peak features; in contrast to an ideal capacitor with a constant capacitance, the polymer exhibits a capacitance that increases with the doping level. Due to the overlap between these two current components, the resulting peak current reflects a convolution of diffusion-limited redox processes and capacitive charging related to the polymer's maximum capacitance. Consequently, the derived b-value does not exclusively represent a single mechanism but rather a combination of both.

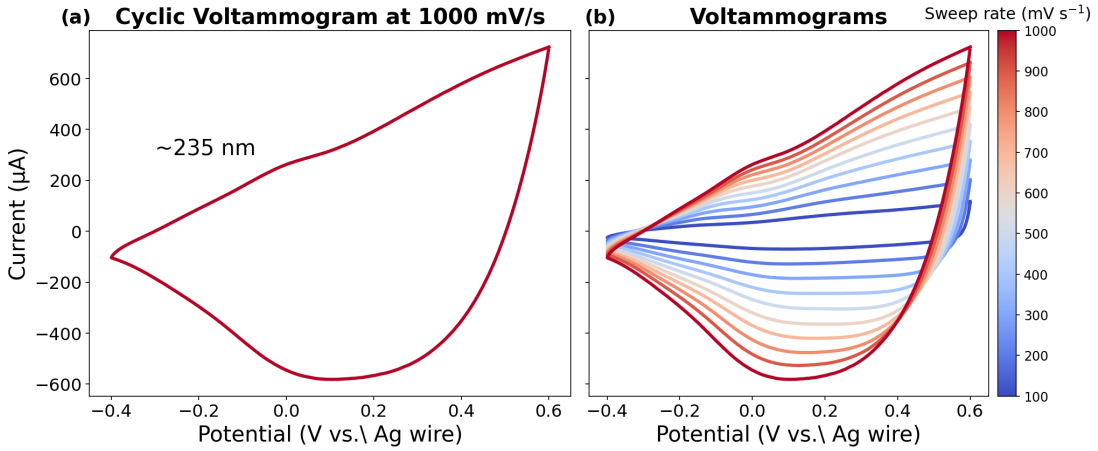

Figure 3.1: Cyclic voltammogram at 1000 mV/s (left) and voltammograms at sweep rates ranging from 100 to 1000 mV/s (right). As expected, the current increases with increasing sweep rate. It is difficult to identify a distinct peak current, though a shoulder appears to be present around 0 V, likely embedded within broader features.

As seen in Figure 3.1, it is difficult to select a distinct peak current for peak value analysis, as the voltammogram lacks the well-defined peak that is typically observed in diffusion-controlled systems. A similar situation is observed in

Figure 3.2, where the film is relatively thin; comparable thicknesses were determined using VKX measurements, with a calibration curve employed to obtain the average height of the scanned film surface.

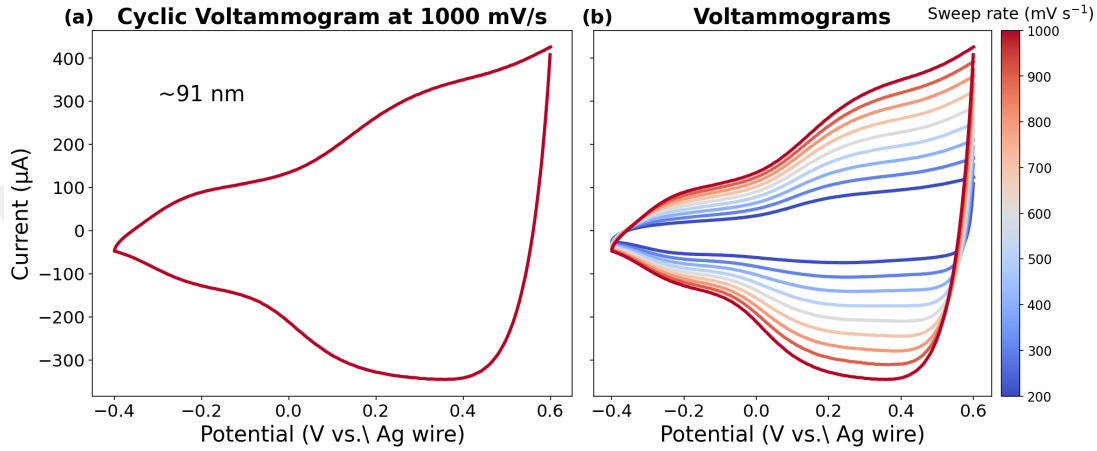

Figure 3.2: Cyclic voltammogram of a 91 nm film at 1000 mV s^{-1} (left) and voltammograms of the same film at sweep rates ranging from 100 to 1000 mV s^{-1}.

The key difference between Figures 3.2 and 3.1 is the film thickness, which is explicitly varied as the main experimental parameter. For example, the film in Figure 3.2 has a thickness of 91 nm, as determined by VKX profilometry. Thickness values were obtained from a calibration curve relating the scanned surface height to film thickness.

3.1.2 Current Normalization by the Square Root of Sweep Rate and by Sweep Rate

As evident from the previously presented cyclic voltammograms, distinct peak currents could not be identified. Therefore, instead of performing a *b*-value analysis, the entire current was normalized by both the square root of the sweep rate and the sweep rate itself. This normalization allows for the evaluation of the system's behavior across the full potential window, revealing which potential regions are dominated by diffusion-limited processes and which are governed by

surface-controlled responses (Figure 3.3).

To better understand the concept of normalization, let us refer to the Cottrell equation. If we express time in terms of sweep rate, we obtain:

$$i(t) = \frac{nFAD^{1/2}C}{\sqrt{\pi t}} \tag{3.1}$$

- $i(t)$: Time-dependent current (A)
- n: Number of electrons transferred (dimensionless)
- F: Faraday constant, $96485\,\mathrm{C}\cdot\mathrm{mol}^{-1}$
- A: Electrode surface area (cm^2)
- D: Diffusion coefficient (cm^2/s)
- C: Bulk concentration of the electroactive species ($\mathrm{mol}/\mathrm{cm}^3$)
- t: Time (s)

$$t = \frac{E - E_0}{v} \quad \Rightarrow \quad t^{1/2} = \left(\frac{E - E_0}{v}\right)^{1/2}$$

Substituting this into the Cottrell equation yields:

$$i(E) = \frac{nFAD^{1/2}C^*}{\pi^{1/2}} \cdot \left(\frac{v}{E - E_0}\right)^{1/2}$$

By dividing both sides of the equation by the only variable in the system, namely the sweep rate, we obtain a constant that contains the diffusion coefficient. When this normalization is applied to all current values at each potential point across all sweep rates, we observe that the currents tend to converge in certain potential regions, approaching a limiting behavior. These regimes where the current values converge define the diffusion-controlled potential domains. Similarly, when the current is normalized directly by the sweep rate itself, only constants

remain in Laviron's equation. This characteristic trend is also observed in our experimental data (Figure 3.3).

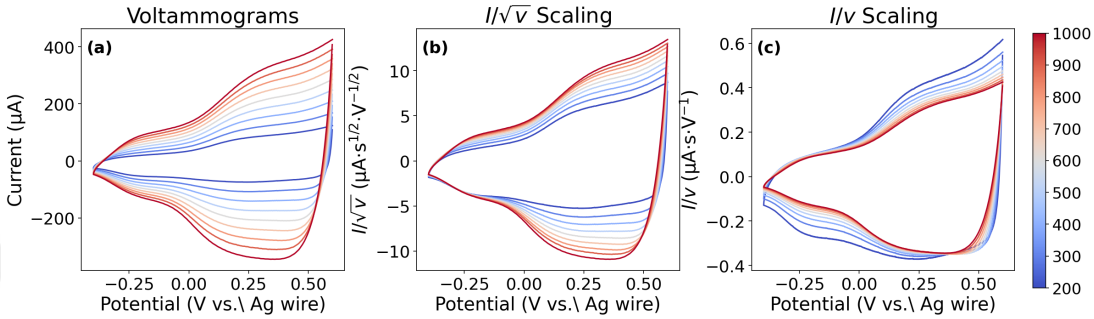

Figure 3.3: Overlay of cyclic voltammetry data for various scan rates. (a)Raw current response; (b)Current normalized by the square root of the sweep rate, $I/\sqrt{v}$; (c) Current normalized by the sweep rate, I/v.

As shown in Figure 3.3.b, when the current is normalized by the square root of the sweep rate, the responses at approximately –0.1 V and 0.2 V overlap for increasing sweep rates. This observation indicates that the electrochemical process occurring in this region is diffusion-limited. However, it would be inaccurate to describe this potential region as governed purely by diffusion, since, as seen in Figure 3.3.c, the current curves between –0.3 V and 0.0 V show a higher degree of overlap. This suggests that both diffusion and surface redox processes contribute to the current response in this region. Assuming that the capacitive current responds linearly with increasing sweep rate, it is also likely that capacitive contributions are present in this potential window.

During the reverse scan, although the behavior between 0.2 V and 0.4 V appears to be dominated by capacitive effects, the influence of diffusion becomes noticeable again in the potential window between 0.2 V and -0.3 V.

Electrochemical impedance spectroscopy (EIS) and equivalent circuit modeling studies further support this interpretation [105]. When the capacitive and Faradaic components of the current are deconvoluted, it has been reported that a Faradaic current peak appears around 0.0 V (vs Ag/AgCl), while a capacitive current peak is observed at approximately 0.1 V (vs Ag/AgCl) for polyaniline

films. Both capacitive and Faradaic processes are active under applied potentials; however, while the diffusion-limited Faradaic current dominates near 0.0 V (vs Ag/AgCl), the capacitive current becomes more prominent beyond this point. Similar trends can also be replicated using mathematical models.

As demonstrated by this analysis, for a researcher aiming to understand solely the relationship between sweep rate and redox behavior of the polymer, the analysis is limited to a certain extent by the unpredictable and, as of yet, mathematically undeconvoluted capacitive current components of the polymer film. In the following section, we will discuss how this analysis is expanded through the use of UV-VIS spectroscopy.

3.2 Basis Set Analysis of PEDOT Films under Slow Sweep Rates

At a scan rate of 2 mV/s, the UV-VIS spectra collected throughout the full range of oxidation states of the polymer are referred to as the *basis set*. The basis set is unique to each fabricated film; in other words, each film has its own corresponding basis set data. All subsequent analyses are performed with reference to the respective basis set of that specific film. Since the scan rate is very slow, the polymer is probed at quasi-equilibrium during different oxidation levels, allowing the collection of optical data corresponding to its instantaneous redox states.

When this measurement is performed on polymer films of different thicknesses (nanometer-scale for thin films versus micrometer-scale for thick films), two distinct differences are observed between the thin and thick films. Even when the same potential window is applied during cyclic voltammetry, the change in absorbance ($\Delta A = A_{\max} - A_{\min}$) at the boundary potentials is smaller for thin films compared to thick films. In other words, thin films exhibit a lower absorbance modulation between fully reduced and fully oxidized states than thick films under

the same electrochemical conditions.

As shown in the Figure 3.4, the absorbance of the thin films varies between approximately 0.1 and 0.5, whereas for the thick films, it ranges from about 0.5 to 2. This demonstrates that the optical modulation of the thick films is significantly greater than that of the thin films under the same experimental conditions.

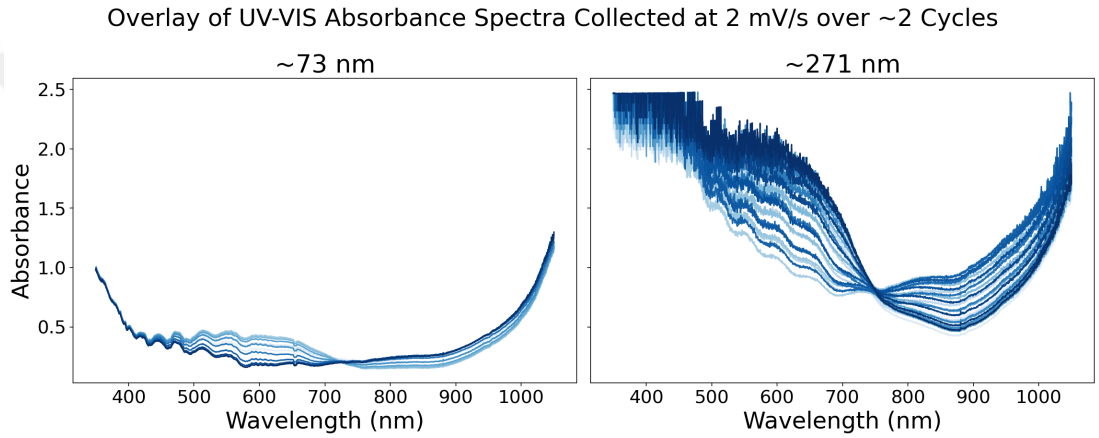

Figure 3.4: UV-VIS absorbance spectra collected at 2 mV/s for thin and thick PEDOT films.

The second observed difference is related to stability. Under identical conditions, thin films that were electrodeposited exhibited better color change stability compared to thick films, even after a high number of cycles. Despite extended cycling, the thin films maintained their optical contrast more effectively, suggesting improved electrochemical durability relative to their thicker counterparts. This highlights that both color contrast and electrochemical stability have an optimal range for practical applications, indicating a trade-off between these two properties.

Since thicker films were obtained by applying the same current for a longer duration, the prolonged potential application may have led to overoxidation [106], thereby reducing the number of healthy cycles for the polymer. Under prolonged oxidative conditions, irreversible structural degradations such as bond cleavage and the formation of oxygenated functional groups occur, ultimately leading to

the loss of conductivity, electrochromic contrast, and electrochemical reversibility [107].

Nevertheless, the potential window and data intervals used in this study were carefully selected to ensure the preservation of the polymer's stability throughout the measurements.

3.3 Color contrast as a function of sweep rate

Since the main objective of this study is to understand the charge transfer mechanism as a function of increasing sweep rate, UV-VIS measurements were carried out at various scan rates for the polymer films. Ten measurements ranging from 100 mV/s to 1000 mV/s were performed and overlaid for both thin and thick films.

Preliminary observations indicate that as the sweep rate increases, the change in absorbance between the conditioning potential and the **average response** during cyclic voltammetry ($A_{\mathrm{CV}} - A_{\mathrm{cond}}$) gradually decreases. However, the rate of this decrease becomes less significant at higher sweep rates. This distinction is more pronounced and visually observable in thin films, making the sweep rate-dependent behavior easier to interpret (Figure3.5).

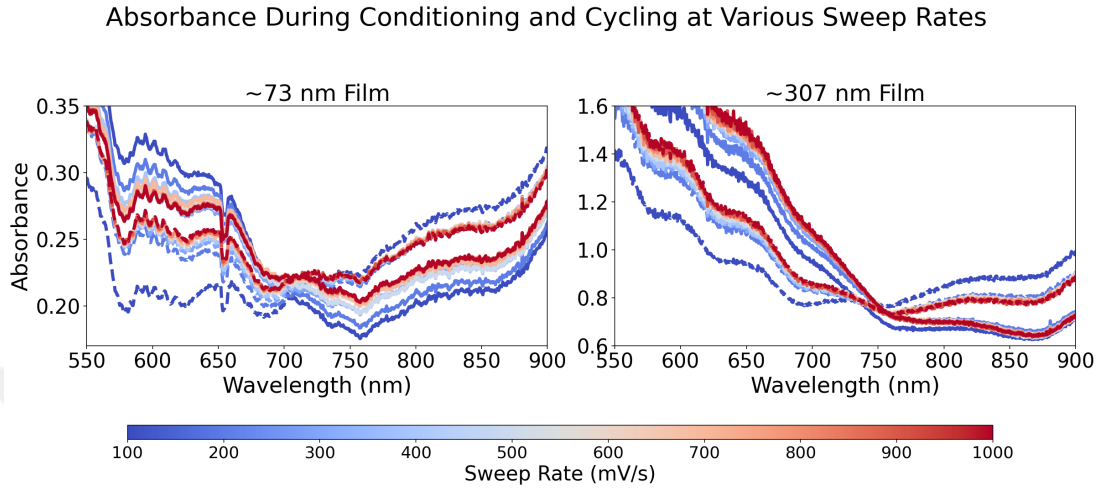

Figure 3.5: Overlay of absorbance spectra collected at different sweep rates (100–1000 mV/s) for thin and thick polymer films. The difference in absorbance between the conditioning potential and the **average response** during cyclic voltammetry ($A_{\mathrm{CV}} - A_{\mathrm{cond}}$) decreases with increasing sweep rate, particularly in thin films. Conditioning spectra are represented with dashed lines, while spectra collected during cyclic voltammetry are shown with solid lines.

As observed in thin films, the difference in absorbance between conditioning and cycling is most pronounced at 100 mV/s across the entire wavelength range. This difference decreases with increasing sweep rate, and the rate of decrease itself becomes less significant at higher sweep rates, indicating a nonlinear response. In contrast, the trend observed in thick films is more complex. With increasing sweep rate, a general upward shift in absorbance is evident, making it more difficult to clearly define the relationship between absorbance change and sweep rate, as was done for thin films. Furthermore, in both film types, the absorbance values appear to approach a limiting value at higher sweep rates, suggesting the presence of a saturation behavior in the optical response.

These results were also found to be consistent with those from other samples. The observation of absorbance shifts along the y-axis in thin films (see Figure 3.6b) suggests that this behavior is influenced by factors beyond just film thickness.

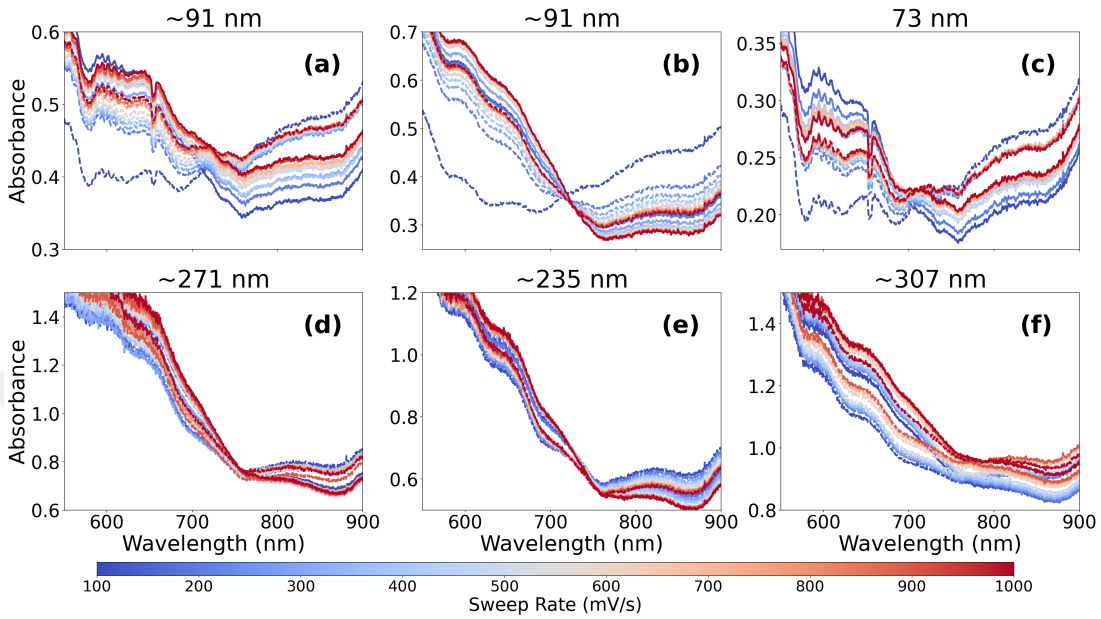

Figure 3.6: Overlay absorbance spectra collected during conditioning and cycling between 100 and 1000 mV/s for three relatively thin and three thick films

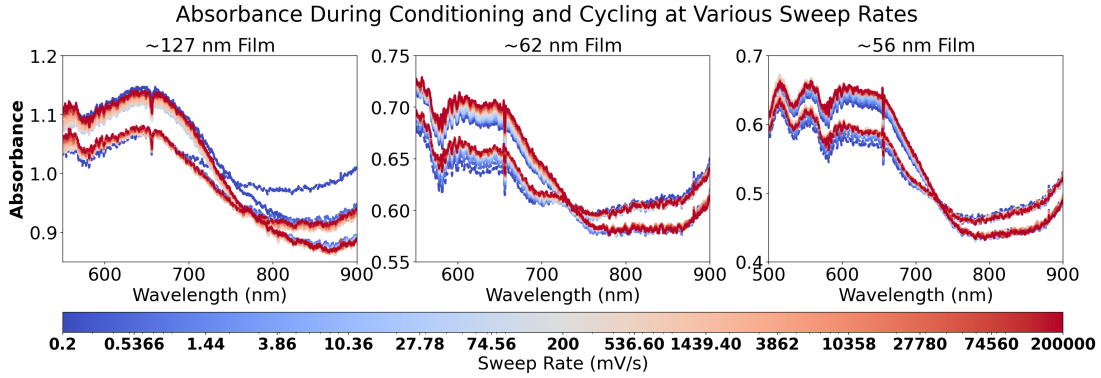

Figure 3.7: Absorbance spectra of polymer films with different thicknesses (127 nm, 62 nm, and 56 nm) collected during initial conditioning (dashed lines) and subsequent cyclic voltammetry (solid lines) at sweep rates ranging from 0.2 to 200,000 V/s. The color gradient (blue to red) represents the sweep rate, with lower rates in blue and higher rates in red.

3.4 Principal Component Analysis of the Films at Different Thickness

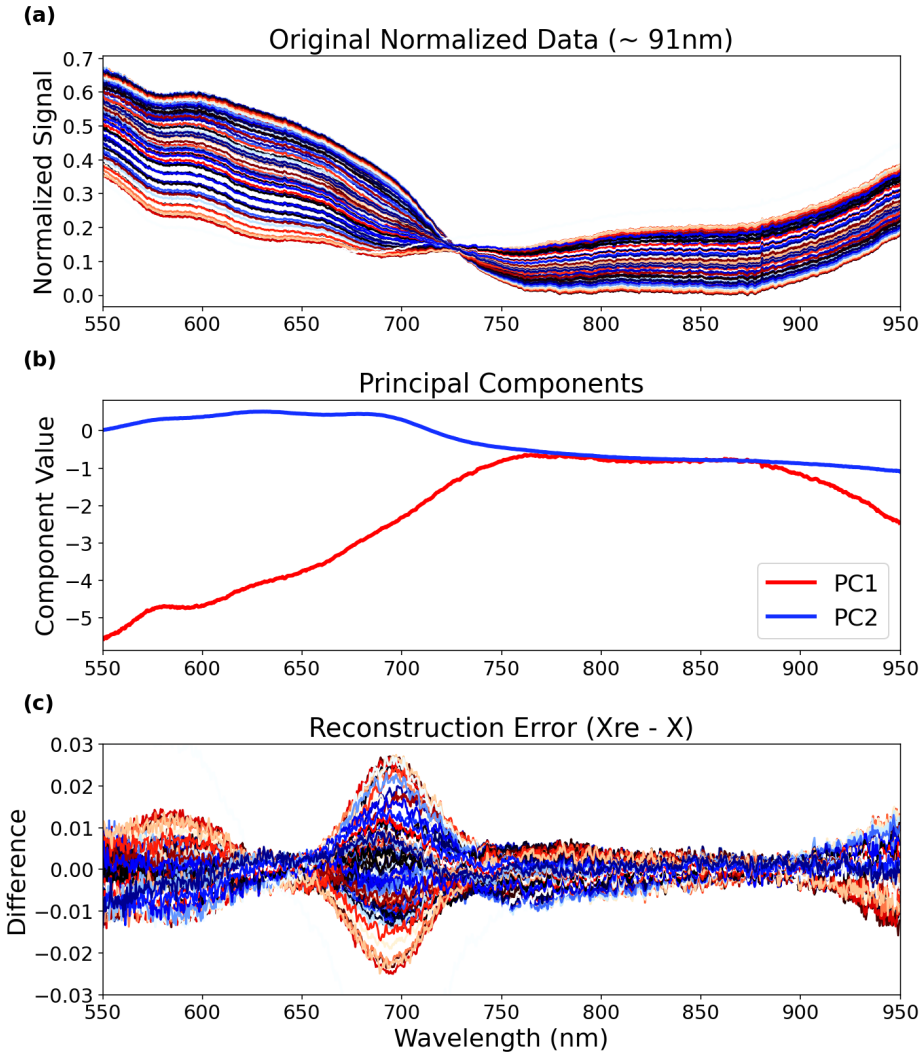

Figure 3.8: Principal Component Analysis (PCA) results for a 91 nm polymer film. (a) Original normalized spectral data obtained from the dataset. Each curve represents an individual spectral trace. (b) The first two principal components (PC1 and PC2) derived from the PCA, capturing the dominant modes of variation in the data. (c) Reconstruction error between the original data and the PCA-based reconstruction using the first two components. The low reconstruction error indicates that most of the variance in the dataset is well-represented by PC1 and PC2.

All experimental data used for PCA analysis including the basis set conditioning and the absorbance versus wavelength data collected during cycling were normalized. First, the minimum value across the entire dataset was identified and subtracted from all data points. As a result, all values became non-negative. After this normalization process, the data were scaled naturally between 0 and 0.8, as shown in Figure 3.8a.

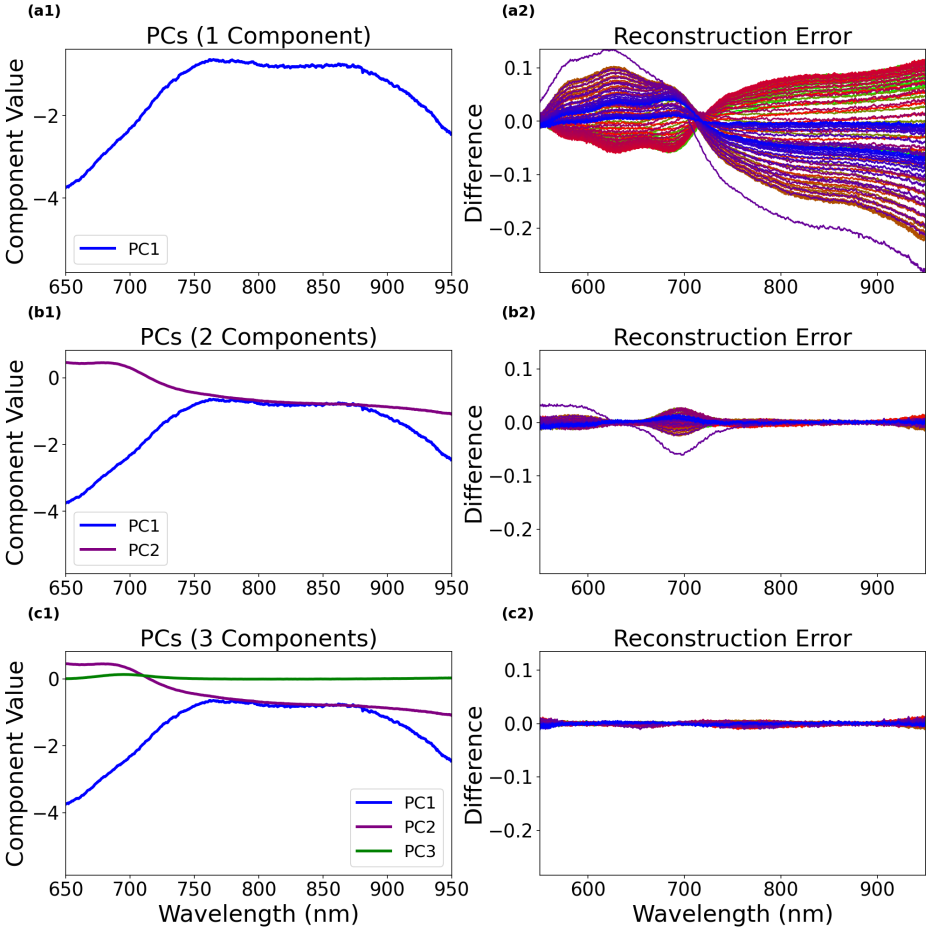

Figure 3.9: Reconstruction errors for the 91 nm film using one, two, and three principal components (PCs). The explained variance ratios for PC1 to PC5 are 95.47%, 4.30%, 0.10%, 0.054%, and 0.019%, respectively. Increasing the number of components from one to two drastically reduces the reconstruction error, while adding a third component results in only a marginal improvement.

Figure 3.8b presents the first two principal components obtained from PCA.

The first principal component (PC1) explains the greatest amount of variance in the dataset, while the second component (PC2) explains the second most. The shapes of PC1 and PC2 must be distinct, as each represents an orthogonal direction of variation. These components capture the dominant modes of change in the dataset and serve as a compressed summary of the original data. When a third principal component is introduced, The third principal component (PC3) remains approximately constant at zero, indicating that it does not capture any significant additional variance in the data and may reflect noise or redundancy. (see Figure 3.9)

The proportion of variance explained by each principal component (PC) are as follows: PC1 accounts for 99.15% of the total variance, PC2 explains 0.68%, and PC3 contributes only 0.10%. The fourth and fifth components explain even smaller amounts of variance, with 0.027% and 0.0067%, respectively. These results indicate that nearly all of the relevant information in the dataset is captured by the first principal component alone, with minimal contributions from the subsequent components. Including more than two or three components is therefore unlikely to yield significant improvements in data reconstruction and may only introduce noise or redundancy.

Finally, in Figure 3.8c, the original data are reconstructed using the selected principal components, and the reconstruction error is visualized. If the number of PCA components (PCs) is sufficient, this error remains small, suggesting that PCA has successfully captured the majority of the data's structure. Conversely, a large error implies that additional components are needed to fully represent the data.For the dataset corresponding to the 91 nm film, which ranges from 0 to 0.8 in normalized values, the reconstruction error was observed to range between -0.06 and $+0.03$.

For thicker films (approximately 307 nm), after normalization of the dataset, the maximum signal is observed to reach around 1.4. Similar to the thinner films, this dataset can also be described using only two principal components. The explained variance ratios are 95.5% for PC1, 4.3% for PC2, and less than 0.2% for each of the remaining components. This confirms that PC1 and PC2 capture

nearly all meaningful variation in the data. A noticeable parabolic increase in the reconstruction error is observed around 700 nm, similar to the thinner film case. This local increase in error may be attributed to abrupt spectral changes or structural transitions and is also reflected in the fits. Further PCA analysis results can be found in Appendix A.

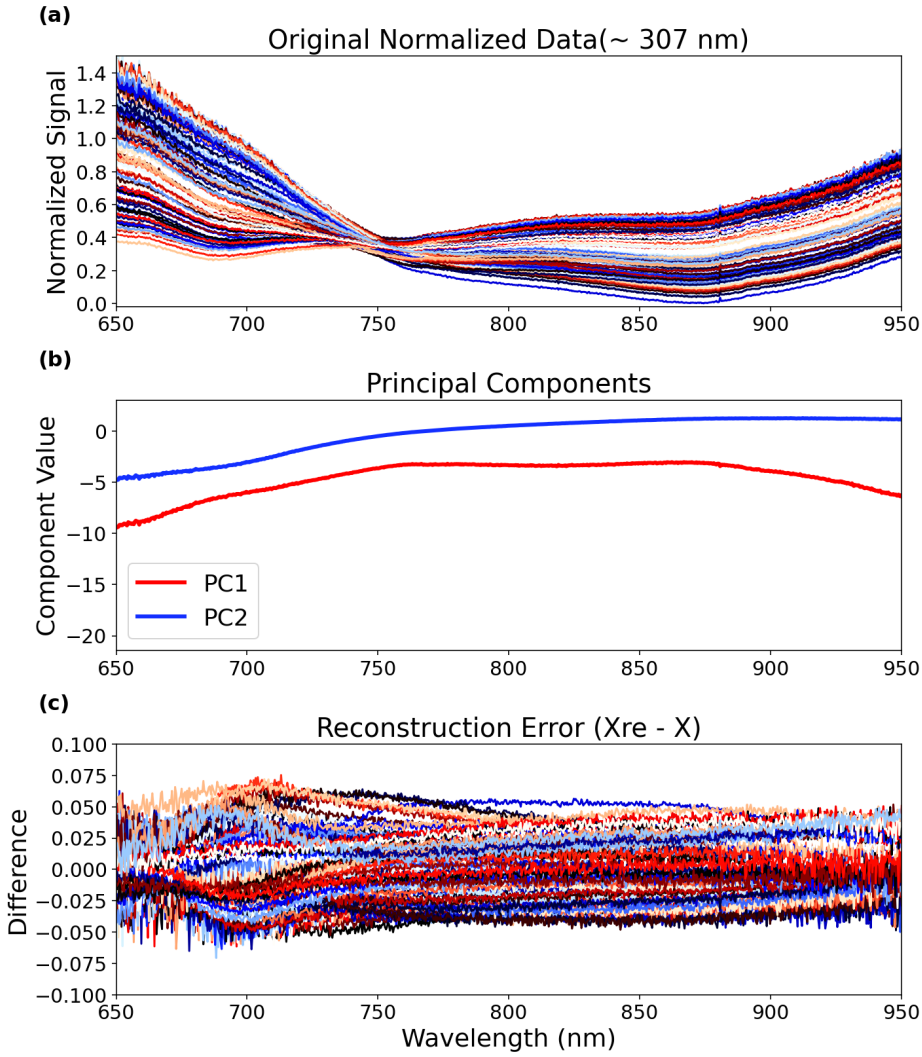

Figure 3.10: For the 307 nm film, two principal components explain over 99.8% of the variance, with PC1 and PC2 accounting for 95.5% and 4.3%, respectively.

3.5 Isosbestic Point

An isosbestic point is defined as the wavelength at which the absorption spectra of two interconverting species intersect, such that the absorbance remains constant despite changes in their relative concentrations. In earlier studies, isosbestic points in conducting polymers have been reported, as shown by Garreau *et al.* [108]. In the present work, in some films such as in Fig. 3.11, a single isosbestic point is observed within the basis set data. In contrast, for relatively thicker films, for example in Fig. 3.12, the isosbestic point shifts, resulting in the presence of multiple isosbestic points within the same basis set. Such shifts, or even the disappearance of isosbestic points in two-component systems, have also been noted in previous studies[109], and a correction method was proposed. Beer's Law applies in dilute solutions, but in condensed-phase conducting polymers the dielectric local field alters the absorbance, peak position, and bandwidth. This leads to nonlinear spectral behavior and the loss of isosbestic points.

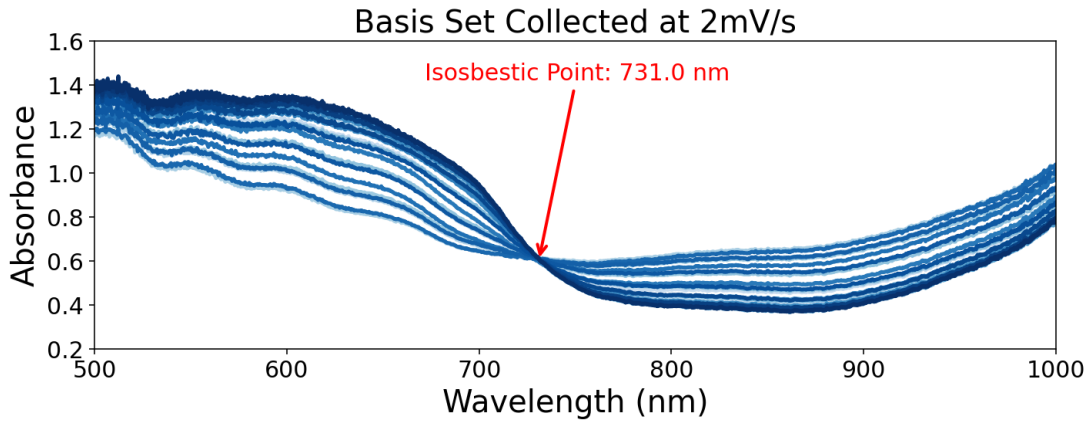

Figure 3.11: Basis set measurement of the 145 nm thick film, showing a clear isosbestic point at 731 nm, which indicates a well-defined interconversion between two dominant spectral states.

Figure 3.12 demonstrates that in the 307 nm film the isosbestic point shifts with potential, revealing deviations from ideal two-state behavior.

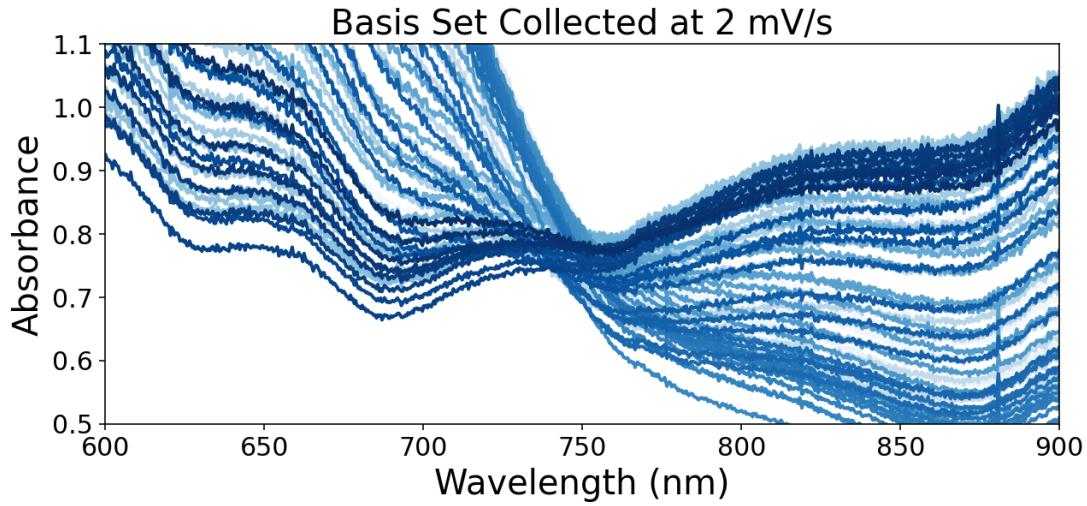

Figure 3.12: Basis set measurement of the 307 nm thick film. The isosbestic point is observed to shift rather than remain fixed, indicating deviations from ideal two-state behavior.

Isosbestic points are observed not only in the basis set data but also in the initial and average spectra obtained at different sweep rates. While the conditioning spectrum under a constant potential represents the steady-state optical response of the film, the onset of cycling, where the film starts to change color, gives rise to spectral differences that likewise exhibit isosbestic points. This indicates that the occurrence of isosbestic behavior is not restricted to the basis set representation but is also present in the dynamic spectral evolution of the polymer during redox cycling (Fig. 3.13).

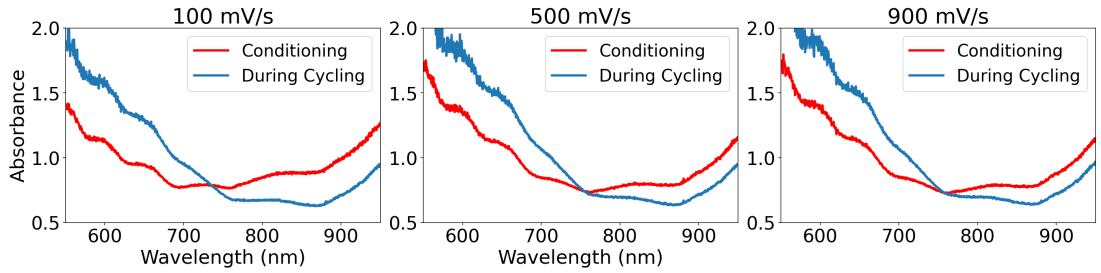

Figure 3.13: Absorbance spectra of the conducting polymer film obtained from *Initial* (before cycling) and *Average* (during cycling) measurements at selected sweep rates (100, 500, and 900 mV/s). The comparison highlights the position and stability of the isosbestic point, illustrating how it evolves with increasing scan rate.

3.6 Spectral Curve Fitting

The plots below show an example of the fit for a $\approx 73\,\text{nm}$ film. The appropriate coefficients are found by selecting two elements from the basis set, multiplying them with their respective basis set curves, and summing them to obtain the calculated curve.

The left plots show the fit for the measurements taken when a fixed potential was applied to the polymer film, and the right plots show the fit for the measurements taken during cycling. These fits are shown for sweep rates ranging from 100 to 1000 mV/s. In general, the fits align well across all wavelengths, although there is a slight mismatch between the calculated and measured curves in the range of 600-700 nm. This issue was observed in other film samples as well. PCA analyses revealed that the reconstruction error for the reconstructed curve corresponding to this wavelength range was higher, as seen in the error margins. This suggests that the fit discrepancy in this range might be associated with higher error during reconstruction.

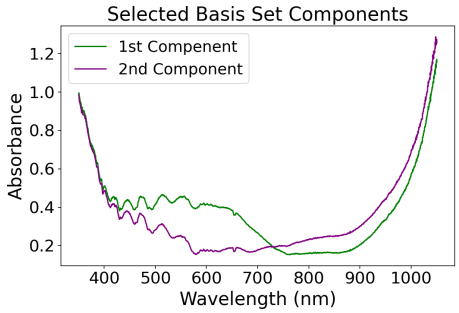
Selected Basis Set Components
1st Compenent
2nd Component
Absorbance
Wavelength (nm)

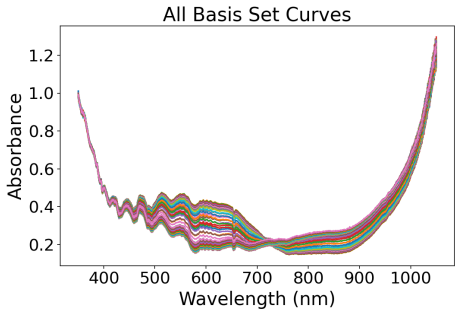
All Basis Set Curves
Absorbance
Wavelength (nm)

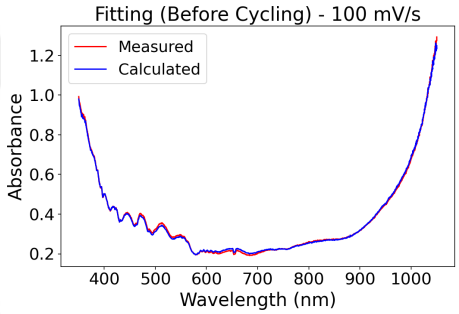
Fitting (Before Cycling) - 100 mV/s
Measured
Calculated
Absorbance
Wavelength (nm)

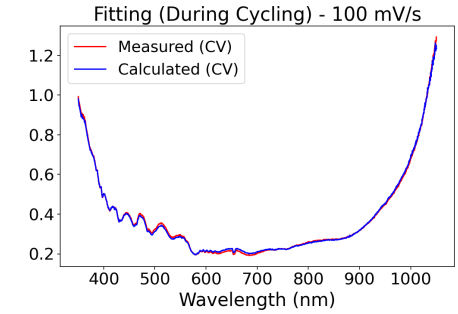
Fitting (During Cycling) - 100 mV/s
Measured (CV)
Calculated (CV)
Absorbance
Wavelength (nm)

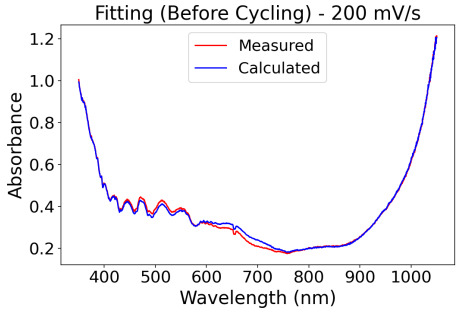
Fitting (Before Cycling) - 200 mV/s
Measured
Calculated
Absorbance
Wavelength (nm)

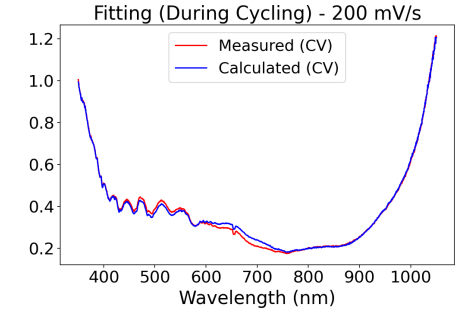
Fitting (During Cycling) - 200 mV/s
Measured (CV)
Calculated (CV)
Absorbance
Wavelength (nm)

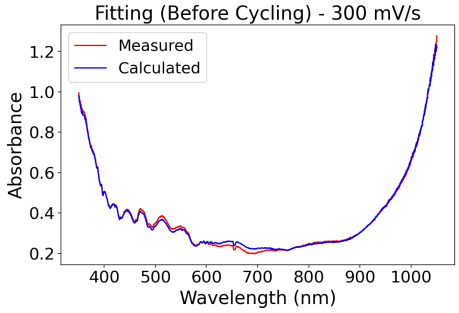
Fitting (Before Cycling) - 300 mV/s
Measured
Calculated
Absorbance
Wavelength (nm)

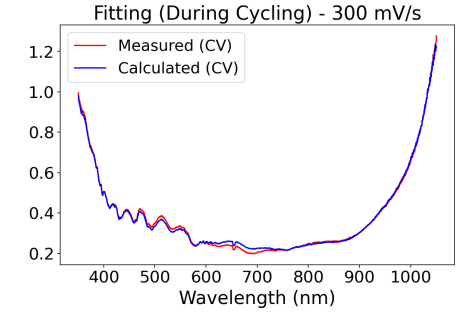
Fitting (During Cycling) - 300 mV/s
Measured (CV)
Calculated (CV)
Absorbance
Wavelength (nm)

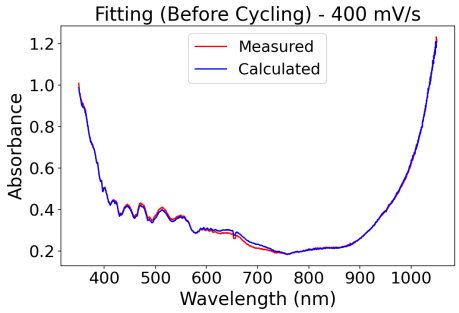
Fitting (Before Cycling) - 400 mV/s
Measured
Calculated
Absorbance
Wavelength (nm)

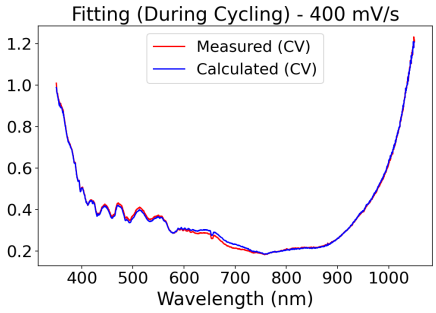
Fitting (During Cycling) - 400 mV/s
Measured (CV)
Calculated (CV)
Wavelength (nm)

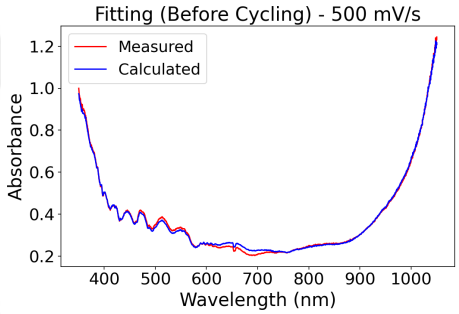
Fitting (Before Cycling) - 500 mV/s
Measured
Calculated
Absorbance
Wavelength (nm)

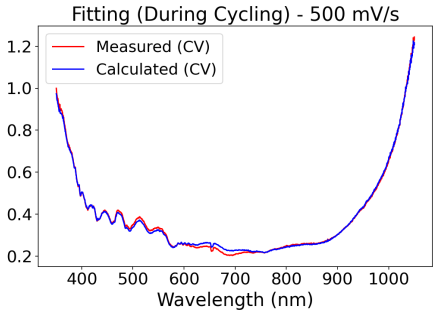
Fitting (During Cycling) - 500 mV/s
Measured (CV)
Calculated (CV)
Wavelength (nm)

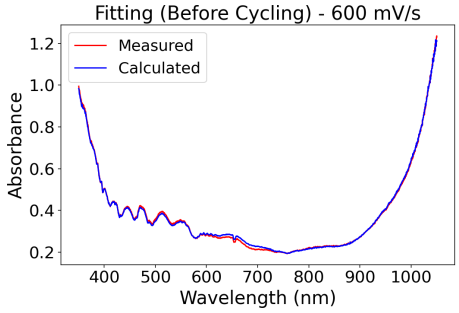
Fitting (Before Cycling) - 600 mV/s
Measured
Calculated
Absorbance
Wavelength (nm)

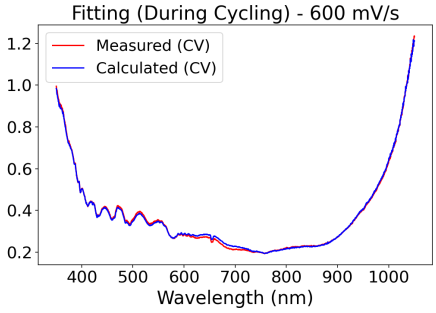
Fitting (During Cycling) - 600 mV/s
Measured (CV)
Calculated (CV)
Wavelength (nm)

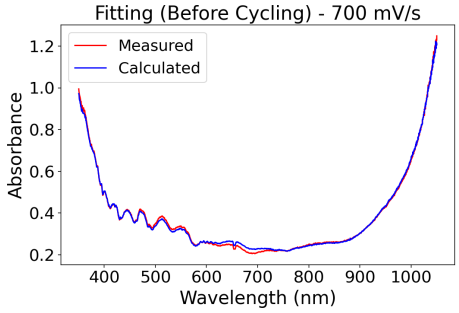
Fitting (Before Cycling) - 700 mV/s
Measured
Calculated
Absorbance
Wavelength (nm)

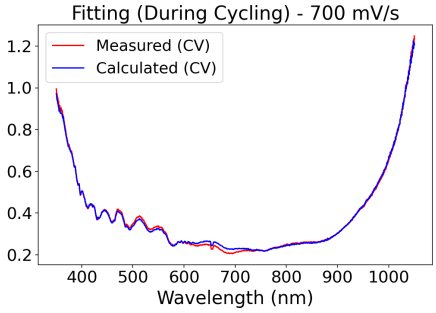
Fitting (During Cycling) - 700 mV/s
Measured (CV)
Calculated (CV)
Wavelength (nm)

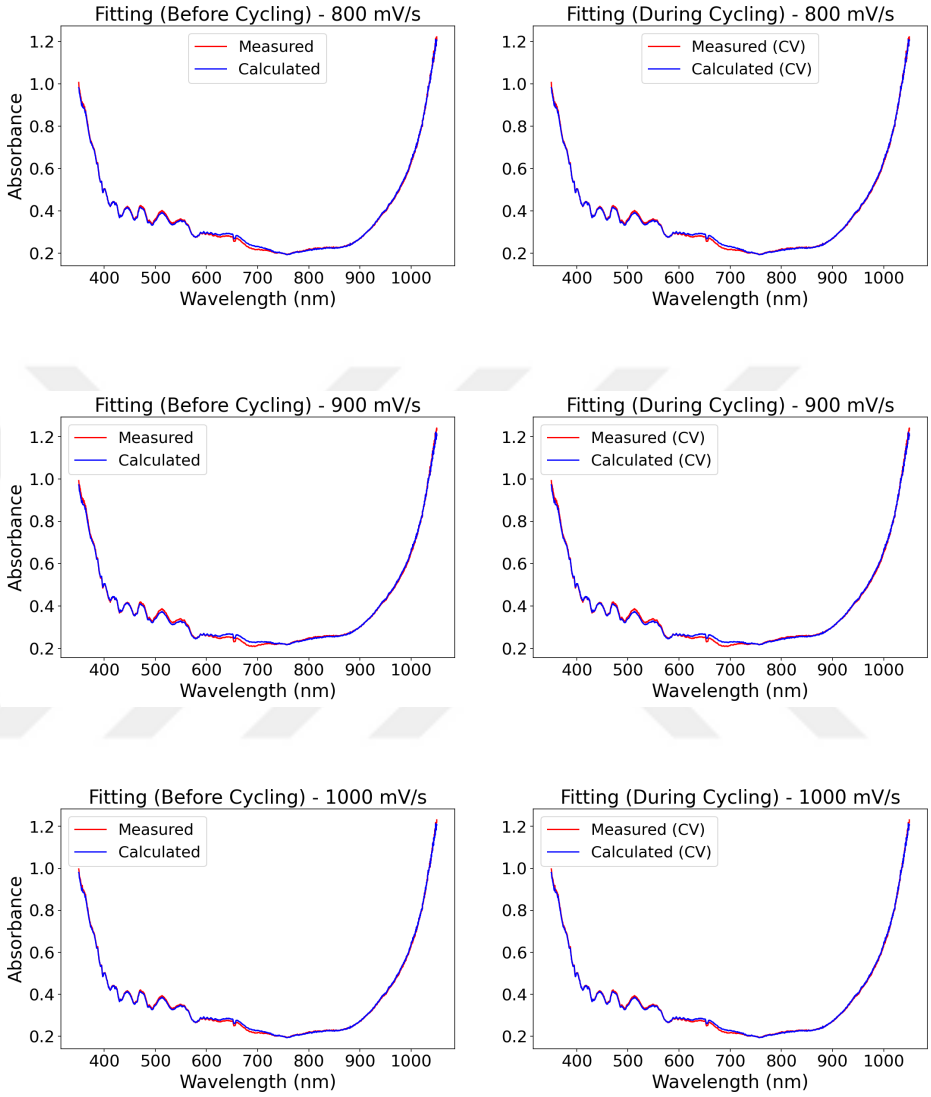

Table 3.1 summarizes the fitted coefficients (*coeff1* and *coeff2*) obtained from the basis set analysis during the conditioning and cyclic voltammetry (CV) measurements.

Table 3.1: Fitted coefficients (*coeff1* and *coeff2*) obtained from basis set analysis during *Conditioning* and subsequent *CV* measurements at different sweep rates (100–1000 mV/s). The alternating row colors highlight the difference between conditioning and CV data at each sweep rate.

Measurement	**Coeff 1**	**Coeff 2**
100 Conditioning	0.038	0.95
100 CV	0.54	0.46
200 Conditioning	0.19	0.79
200 CV	0.47	0.53
300 Conditioning	0.20	0.77
300 CV	0.37	0.62
400 Conditioning	0.20	0.76
400 CV	0.40	0.58
500 Conditioning	0.22	0.75
500 CV	0.37	0.62
600 Conditioning	0.21	0.76
600 CV	0.37	0.61
700 Conditioning	0.21	0.75
700 CV	0.38	0.60
800 Conditioning	0.21	0.75
800 CV	0.35	0.63
900 Conditioning	0.22	0.74
900 CV	0.35	0.63
1000 Conditioning	0.22	0.74
1000 CV	0.35	0.63

For the fitting of a thicker film sample (≈307 nm), refer to the details in the Appendix B.

3.7 Optical Charge Coefficients and Sweep Rate Effect

The PCA analysis showed that two components from the basis set were sufficient for fitting the optical data, a finding also observed in the basis set and cyclic voltammetry spectroCV measurements (isosbestic point). The basis set vectors represent the absorbance data, which were collected within the wavelength range of 350–1100 nm during a potential sweep from −0.4 to 0.4 V. Dimensionality reduction analysis revealed that the data can be explained by a single component with an explanatory power exceeding 95%. In order for this mathematical result to gain physical meaning, the basis set data were examined in greater detail. Figure 3.14 (a, b, c) displays the absorbance evolution over time at selected wavelengths for three different polymers with varying thicknesses.From left to right, the film thickness increases, with approximate values of 56, 62, and 127 nm, respectively.

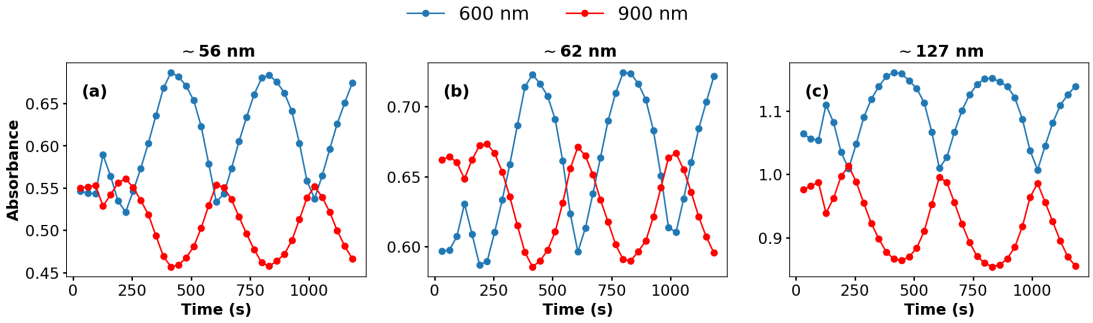

Figure 3.14: Absorbance of the basis set for films with thicknesses of 56 nm (a), 62 nm (b), and 127 nm (c), evaluated at the specific wavelengths of 600 nm and 900 nm, at a scan rate of 2 $\mathrm{mV\,s^{-1}}$ within the potential window of –0.4 to +0.4 V.

Even though the wavelength differs, the absorbance vs. time data exhibit the same overall trend. As the potential becomes more negative over time, the absorbance in the range of 600–700 nm increases, whereas the absorbance at 900 nm, corresponding to the oxidized form, decreases. The corresponding basis set can be found in Appendix Figure .17.

At a scan rate of 2 mV/s, the potential is swept between −0.4 V and +0.4 V. Within this potential window, the absorbance at wavelengths corresponding to the more oxidized state of the polymer and those associated with the more reduced state can be observed throughout the potential sweep. Such spectral evolution can be monitored at very slow scan rates; however, as the scan rate increases, the potential changes more rapidly, and consequently, the lifetime of each oxidation state becomes shorter. Since it is not experimentally feasible to capture each transient oxidation state at time scales on the order of 10^{-5}–10^{-6} s across the 350–1100 nm spectral range due to the limitations of available sensors and instruments, we instead employ principal component analysis (PCA). In this approach, the spectra are reconstructed by decomposing the dataset into the number of components determined by PCA and recombining them with appropriate coefficients. This allows us to analyze how much each component contributes and how these contributions evolve with respect to the initial state.

As an initial step to evaluate whether the obtained coefficients are meaningful with respect to the applied potential, this analysis was performed on the basis set elements. Each column corresponds to the average of 1000 spectra collected over 30 s.

Figure 3.15, the spectra were reconstructed by multiplying the coefficients, `coef1` and `coef2`, plotted on the y-axis, with the two components selected from the same basis set. The variation of these coefficients as a function of time, in correlation with the sweep potential, and their relationship with the absorbance changes at specifically chosen wavelengths of the same film, are presented in the figure on the same axis and scaled by the same factor.

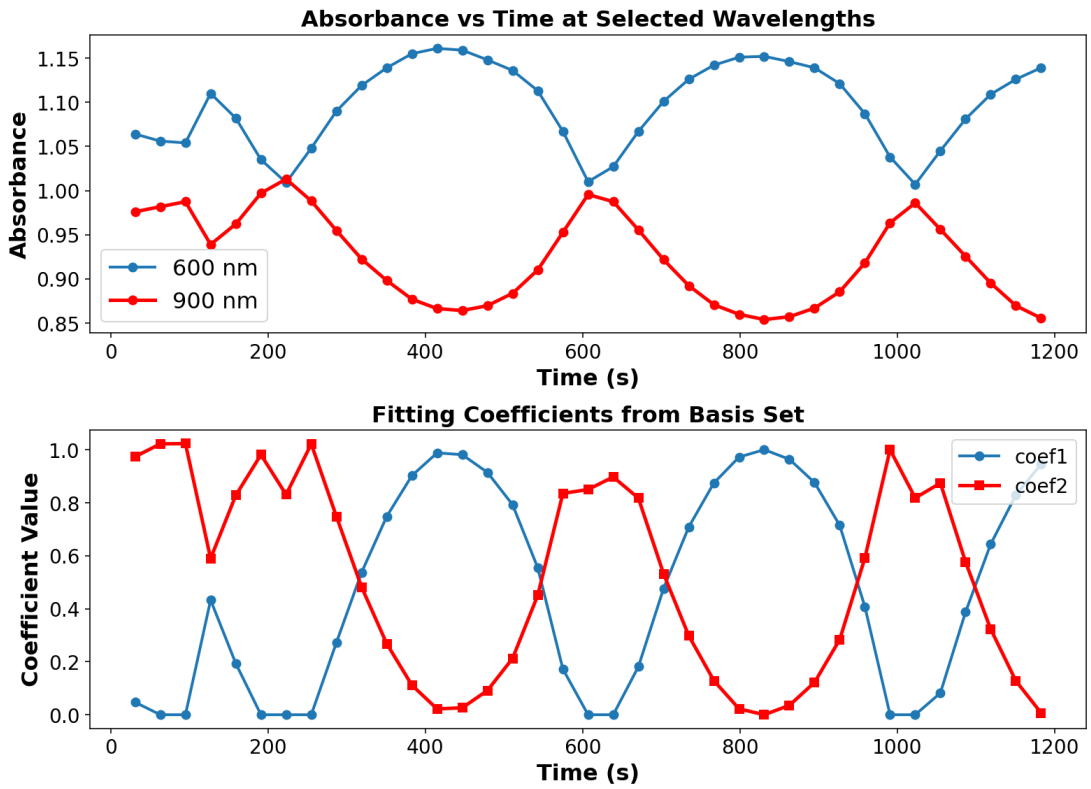

Figure 3.15: Time and potential evolution of the fitted coefficients (`coef1` and `coef2`) obtained from basis set fitting. The x-axis represents the measurement time, which corresponds to the potential sweep during the experiment, while the y-axis shows the coefficient values determined from the optimization. The film thickness is approximately 127 nm, with a potential window of –0.4 to +0.4 V and a sweep rate of 4 mV s^{-1}.

The data were collected using a homemade potentiostat within the potential window of −400 mV to +400 mV at a frequency of 0.0025 s^{-1}, which corresponds to a sweep rate of 4 mV s^{-1}. Considering that the duration of one complete cycle is 400 s, with 200 s allocated to either the forward or reverse scan, the observed increase and decrease in absorbance over a full cycle (400 s) and the corresponding trend followed by the coefficients confirm that the mathematically derived coefficients are consistent with the absorbance evolution. This agreement establishes the correlation between the obtained coefficients, the absorbance response, and the underlying chemical redox processes.

Figure 3.16 shows data analysis obtained with the Gamry potentiostat within the –400 to +600 mV potential window. The two samples have similar thicknesses; however, in this case, the sweep rate is 2 mV s^{-1} and the experiment time is longer.

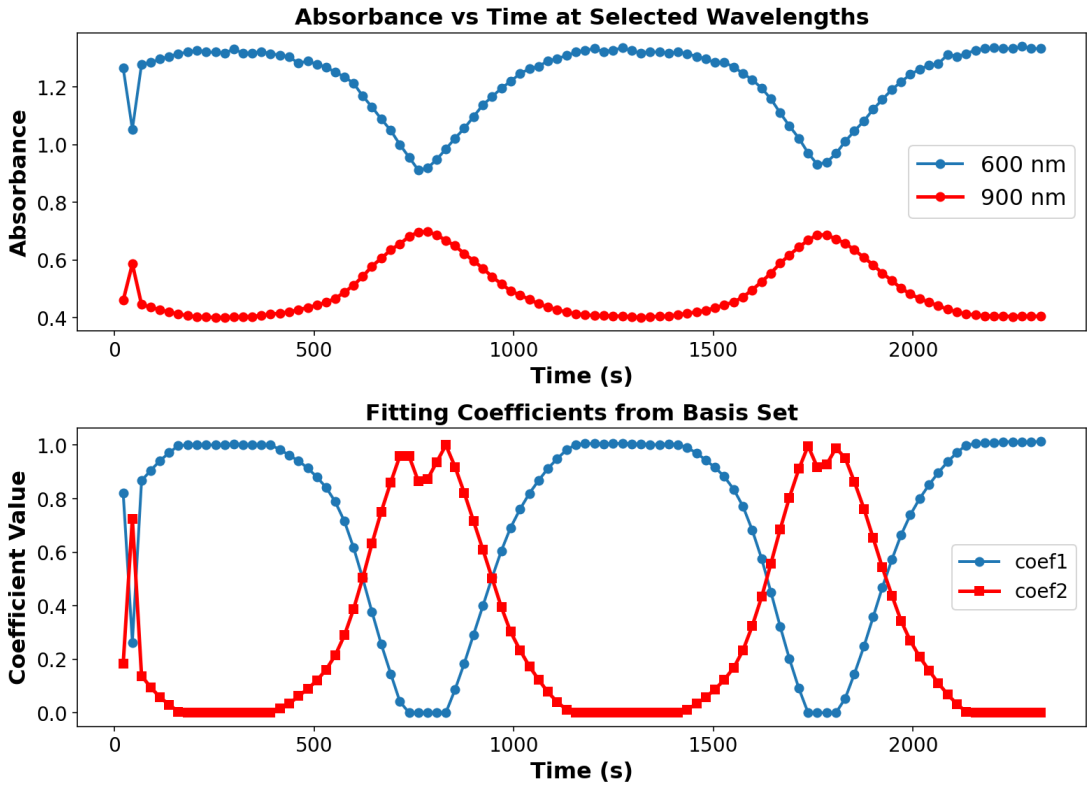

Figure 3.16: Time evolution of the fitted coefficients (`coef1` and `coef2`) obtained from basis set fitting. The x-axis represents the measurement time, while the y-axis shows the coefficient values determined from the optimization. The film thickness is 127 nm, with a potential window of –0.4 to +0.6 V and a sweep rate of 2 mV s^{-1}.

The result of the PCA analysis, in which the first principal component accounts for more than 95% of the variance, indicates that the majority of the variance in the dataset lies along a single direction. If the explained variance had been 100%, all data points would fall on a straight line, implying complete linear dependence. However, both the coefficient analysis applied to the basis set and the absorbance evolution at 600 nm and 900 nm reveal clear nonlinear trends.

In addition, although the overall trend is similar, the rate of absorbance increase differs at different wavelengths.

As shown in Figures 3.15 and 3.16, the absorbance increase is not constant; its derivative decreases as the signal approaches an upper limit. This slowdown suggests that the polymer is nearing its maximum doping level, although confirmation would require examination over a wider potential window. While the potential increment is fixed across all intervals, the corresponding absorbance responses vary, clearly indicating a limitation in the doping mechanism. At such low sweep rates, there is sufficient time for ions to diffuse freely; however, the reduced availability or accessibility of doping sites appears to play a dominant role. This interpretation is further supported by the longer time-scale experiment in Figure 3.16, where the fitted coefficients (`coef1` and `coef2`) obtained from basis set analysis closely track the absorbance changes at 600 and 900 nm. The strong correlation between absorbance evolution and coefficient dynamics highlights the onset of saturation effects and the gradual depletion of accessible redox sites.

The nonlinearity of the absorbance response to equal potential increments also explains the necessity of a second principal component in the PCA analysis. This is further supported by the failure of single-component fits, which cannot adequately capture the deviation from linearity in the experimental data.

The primary aim of this project was to obtain information about the Faradaic reaction by utilizing absorbance data, thereby eliminating the contribution of capacitive currents. In this regard, although using absorbance changes does not yield a strictly linear relationship between potential and absorbance variation, it nevertheless provides complementary insight into the nature of oxidation/reduction or doping/dedoping processes. For this reason, in the next stage of the study, we will analyze the spectroscopic response measured at varying sweep rates.

In the color contrast section, we clearly observed and demonstrated a significant difference between the conditioning measurements and those acquired during cycling. Initially, a constant potential was applied to the polymer in order

to establish the same reference point for each measurement.

In theory, applying the same potential to the same polymer at different time intervals should result in identical spectra. Here, we present an experimental result that includes only the polymer spectra recorded during conditioning, prior to applying different sweep rates.

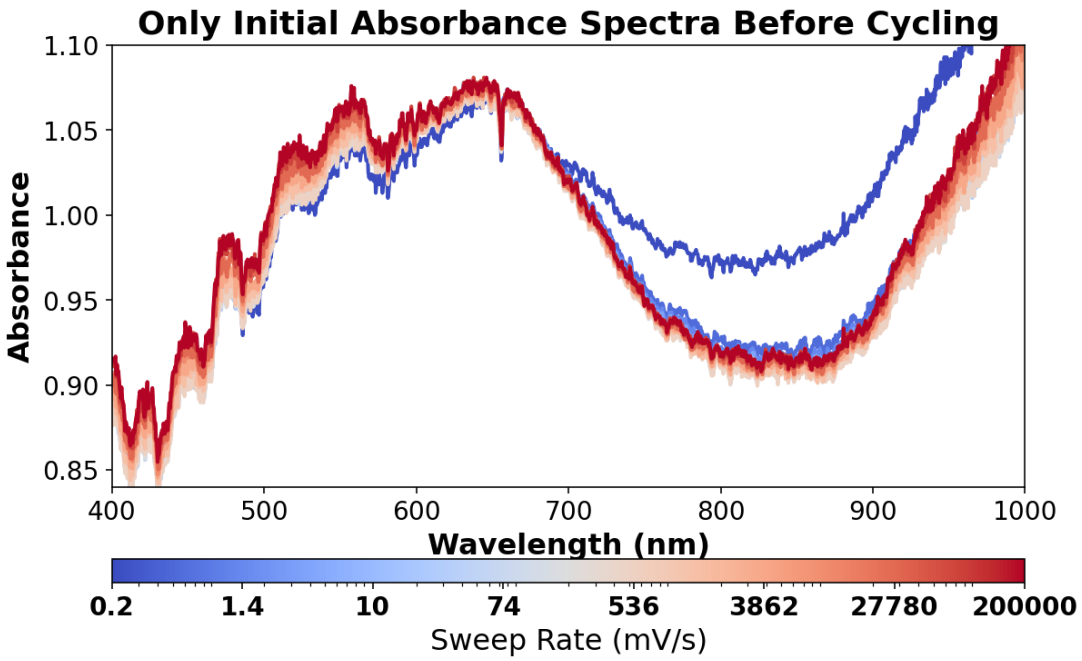

Figure 3.17: Initial absorbance spectra as a function of wavelength. The spectra are obtained before cycling and demonstrate the initial optical response of the polymer film.

As shown in Fig. 3.17, the initial spectra nearly start from the same state; however, with increasing sweep rate, they gradually shift upward, reaching a maximum difference of approximately 0.05 absorbance units.

Let us now investigate how each fundamental component of the polymer evolves when starting from the same reference state and applying the potential at different sweep rates.

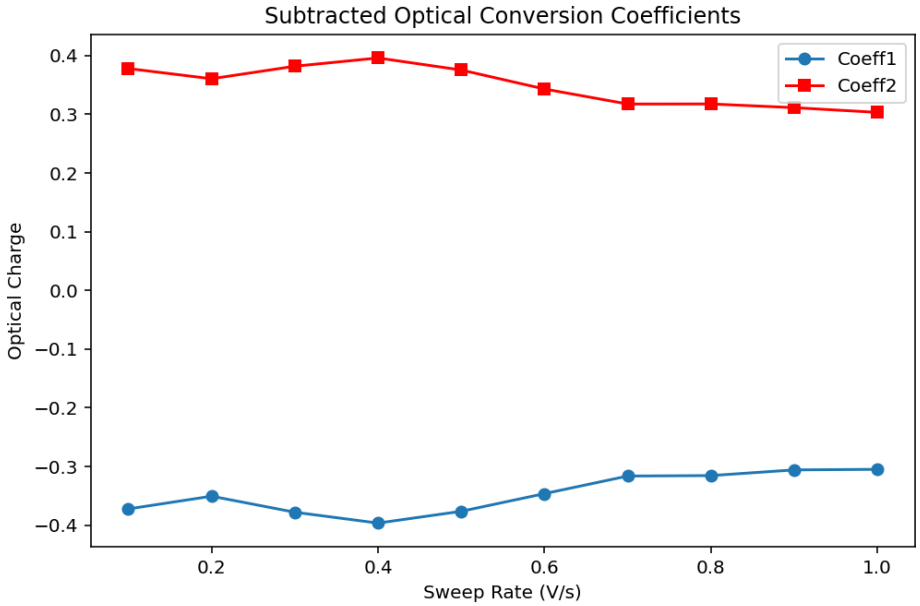

Figure 3.18: The variation of the optical charge coefficients with sweep rate for a polymer film with an approximate thickness of 145 nm.

In the table below (Table 3.2), the calculated coefficients corresponding to the conditioning spectra and the cyclic voltammetry spectra measured at sweep rates ranging from 100 mV/s to 1000 mV/s are presented. The figure above (Fig. 3.18) was obtained by subtracting the coefficients of the conditioning spectra from those of the CV spectra.

Table 3.2: Fitted coefficients (*coeff1* and *coeff2*) obtained from basis set analysis during *Conditioning* and subsequent *CV* measurements at different sweep rates (100–1000 mV/s). The alternating row colors highlight the difference between Conditioning and CV data at each sweep rate.

Measurement	**Coeff 1**	**Coeff 2**
100 Conditioning	0.038	0.95
100 CV	0.54	0.46
200 Conditioning	0.19	0.79
200 CV	0.47	0.53
300 Conditioning	0.20	0.77
300 CV	0.37	0.62
400 Conditioning	0.20	0.76
400 CV	0.40	0.58
500 Conditioning	0.22	0.75
500 CV	0.37	0.62
600 Conditioning	0.21	0.76
600 CV	0.37	0.61
700 Conditioning	0.21	0.75
700 CV	0.38	0.60
800 Conditioning	0.21	0.75
800 CV	0.35	0.63
900 Conditioning	0.22	0.74
900 CV	0.35	0.63
1000 Conditioning	0.22	0.74
1000 CV	0.35	0.63

As previously discussed, the use of conditioning spectra ensures that the polymer starts each measurement from the same reference point. This allows for a direct evaluation of how the coefficients vary with the applied sweep rate (Table 3.2). Interestingly, despite applying the same potential during the acquisition of the initial conditioning spectra, an upward shift is observed in the baseline

response. This systematic shift can also be confirmed by examining the initial coefficient values listed in Table 3.2, which gradually increase with sweep rate.

On the other hand, in the figure below (Fig. 3.19), the plot generated solely from the cycling coefficients without subtraction is presented.

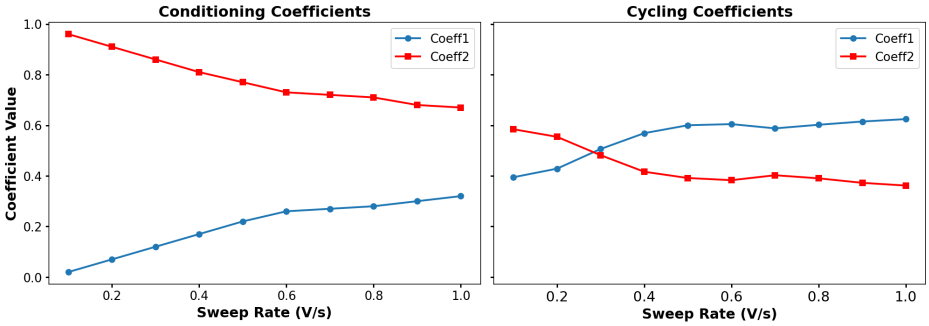

Figure 3.19: Comparison of fitted coefficients obtained from basis set analysis as a function of sweep rate. (Left) During the *conditioning* stage, *coeff1* increases while *coeff2* decreases with increasing sweep rate. (Right) During the *cycling* stage.

Let us now consider the physical meaning of these coefficients. As observed in the basis set analysis, the coefficients can be regarded as representing concentration profiles of the electroactive species. At slow sweep rates, when evolved as a function of either time or potential, the coefficients follow the progression of the redox process and therefore reflect the dynamics of one or two complete cycles within the experiment. In other words, the coefficients are not arbitrary fitting parameters but rather carry direct information about the temporal and potential dependent evolution of the polymer during the electrochemical process.

When considering the cycling regime, each data point representing a given sweep rate actually corresponds to the average over multiple cycles. For instance, at 100 mV/s the measurement associated with a single data point is obtained as the average over three cycles. As the sweep rate increases, the cycles evolve more rapidly, and therefore a larger number of cycles are incorporated within the same measurement window. This distinction is important, since higher sweep rates

not only shorten the duration of individual cycles but also effectively increase the number of repeated redox events contributing to the averaged spectral response.

During cycling, an individual spectrum can be expressed as a linear combination of the basis vectors, such that

$$\mathbf{A}(E,t) \;=\; \mathrm{coeff}_1(E,t)\,\mathbf{b}_1 \;+\; \mathrm{coeff}_2(E,t)\,\mathbf{b}_2,$$

where $\mathbf{A}(E,t)$ denotes the measured absorbance spectrum at a given potential E (or time t), and $\mathbf{b}_1$ and $\mathbf{b}_2$ represent the characteristic basis spectra associated with the coefficients, respectively. The coefficients coeff_1 and coeff_2 thus quantify the relative weighting of these two processes during the electrochemical cycling, effectively serving as concentration-like descriptors that evolve as a function of sweep rate and potential.

If we focus on the difference between the initial cycling coefficients, this essentially reflects how much the absorbance of the polymer, starting from the same oxidation state, changes on average during cycling in terms of the components associated with reduction and oxidation. Since each subsequent sweep rate is faster than the previous one, the most evident parameter that changes is the time available for ion diffusion. Therefore, the observed variations in the coefficients can be directly linked to the extent to which the ionic motion is kinetically limited by the timescale imposed by the sweep rate.

For instance, at a sweep rate of 0.2 V/s the duration of one cycle reaches approximately 8.0 s. Considering a polymer film with a thickness of 100 nm and assuming a counter-ion diffusion coefficient on the order of 10^{-5} cm^2/s, the corresponding diffusion time can be estimated as 10^{-5} s. For a thicker film of 500 nm, this value increases to 2.5×10^{-4} s, while for a 1 µm film it reaches 10^{-3} s at the same diffusion coefficient. Compared to the 8 s cycle time, these diffusion times are sufficiently short to ensure complete ion penetration into the polymer during each cycle.

In contrast, if the diffusion coefficient is decreased to 10^{-10} cm^2/s for films of identical thickness, the estimated diffusion times become significantly longer: 0.1 ms for a 100 nm film, 0.25 s for a 500 nm film, and up to 100 s for a 1 µm thick film. These results highlight the strong dependence of ion transport kinetics on both the diffusion coefficient and the film thickness, and illustrate how, at sufficiently low diffusion coefficients, ion penetration can become severely rate-limiting.

In the examples between 0.1 V/s and 1.0 V/s, the durations of a single cycle corresponding to increasing sweep rates are summarized in Table 3.4.

Table 3.3: Estimated diffusion times ($\tau = L^2/D$) for counter-ion penetration in conducting polymer films of different thicknesses (L) and diffusion coefficients (D). At a sweep rate of 0.2 V/s (cycle period $\approx$ 8 s), diffusion is sufficiently fast for $D = 10^{-5}$ cm^2/s across all thicknesses, whereas for $D = 10^{-10}$ cm^2/s ion transport can become severely rate-limiting.

Film thickness L	$D = 10^{-5}$ cm^2/s	$D = 10^{-10}$ cm^2/s	Unit
100 nm	1.0×10^{-5}	1.0×10^{-4}	s
500 nm	2.5×10^{-4}	2.5×10^{-1}	s
1 µm	1.0×10^{-3}	1.0×10^{2}	s

Table 3.4: Sweep rate, corresponding cycle period and frequency values (2 significant figures).

Sweep Rate (V/s)	**Period per cycle (s)**	**Frequency (Hz)**
0.10	16	0.063
0.20	8.0	0.13
0.30	5.3	0.19
0.40	4.0	0.25
0.50	3.2	0.31
0.60	2.7	0.37
0.70	2.3	0.44
0.80	2.0	0.50
0.90	1.8	0.56
1.00	1.6	0.63

Even at a sweep rate of 1.0 V/s, the duration of a single cycle is still about 1.6 s, which is sufficient for the ions to respond within this timescale for film thicknesses on the nanometer scale. This is summarized in Table 3.3.

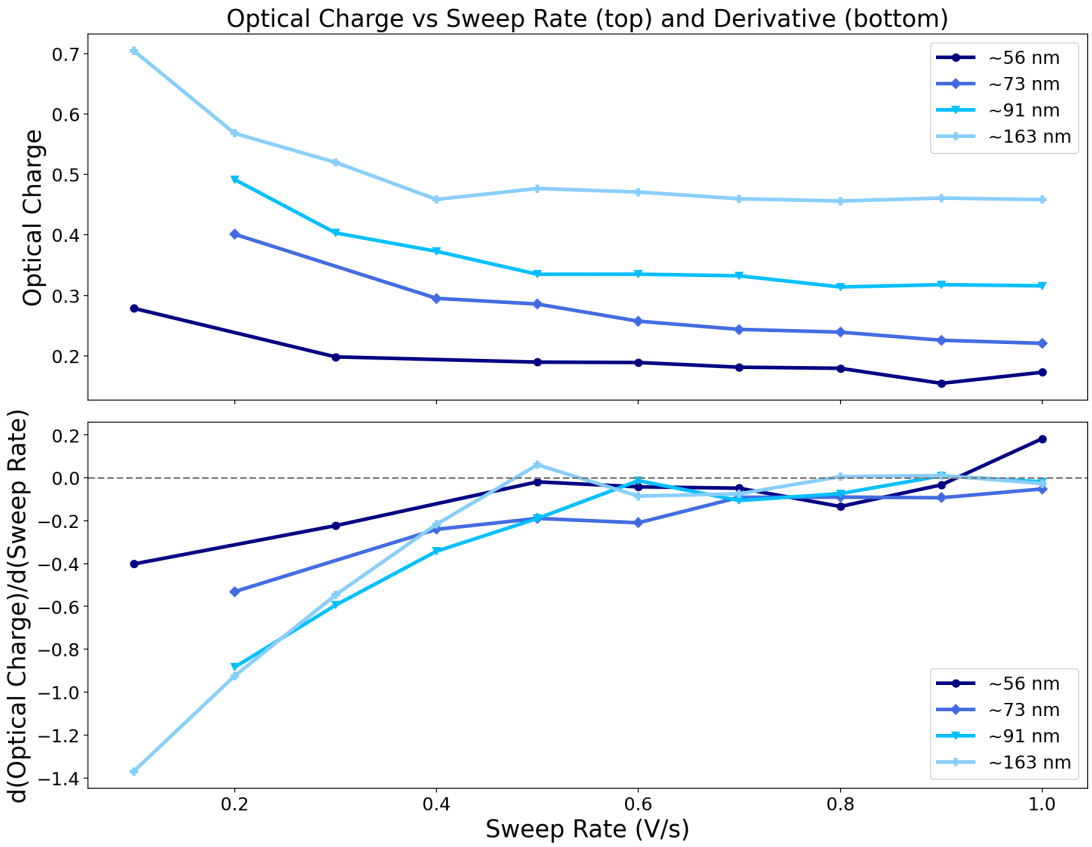

Figure 3.20: The variation of the optical charge coefficients with sweep rate, explaining the change in absorbance across the entire spectrum for polymer films with approximate thicknesses of 56, 73, 91, and 163 nm.

In Figure 3.20, the optical charge response of polymer films with thicknesses of 56, 73, 91, and 163 nm is shown for sweep rates between 0.1 V/s and 1.0 V/s. We refer to this quantity as the "optical charge" since it is obtained by taking the difference between the initial and final states, thereby reflecting an effective average of the redox conversion. A critical point here is to ensure that all measurements start from the same state. In the data presented in Figure 3.20, small variations in the initial coefficients were observed (e.g., 0.40, 0.41, 0.39, etc.). Despite these fluctuations, a stable trend of the difference coefficients at slow sweep rates was clearly observed. Only the positive coefficients are presented here; however, we note that the coefficients of the complementary component exhibit the same magnitude but with a negative sign.

Table 3.5: Selected sweep rate, cycle period, and frequency values (2 significant figures).

Sweep Rate (V/s)	**Period per cycle (s)**	**Frequency (Hz)**
1.0×10^{4}	1.5×10^{-4}	6.5×10^{3}
2.8×10^{4}	5.8×10^{-5}	1.7×10^{4}
7.5×10^{4}	2.2×10^{-5}	4.7×10^{4}
2.0×10^{5}	8.0×10^{-6}	1.3×10^{5}

We consider the trend observed at slow sweep rates to represent only the visible part of the iceberg. If the aim is to shed light on the ion transfer limitations in the polymer and their interplay with electron transfer under these conditions, it is essential to reach much higher sweep rates.

For instance, Table 3.5 summarizes the sweep rates and corresponding cycle durations that could be achieved using the homemade potentiostat.

For films with a thickness of 100 nm or below, and considering diffusion coefficients in the range of 10^{-5} to 10^{-10} $cm^2\,s^{-1}$, a timescale of 10^{-5} to 10^{-4} s is generally regarded as sufficient for ionic diffusion (although within the polymer matrix the effective coefficients may be lower due to the restricted ion motion). However, measurements performed with the fast homemade potentiostat at sweep rates between 1.0×10^4 and 2.0×10^5 V/s suggest that even in such thin films the process may already be limited by ion diffusion.

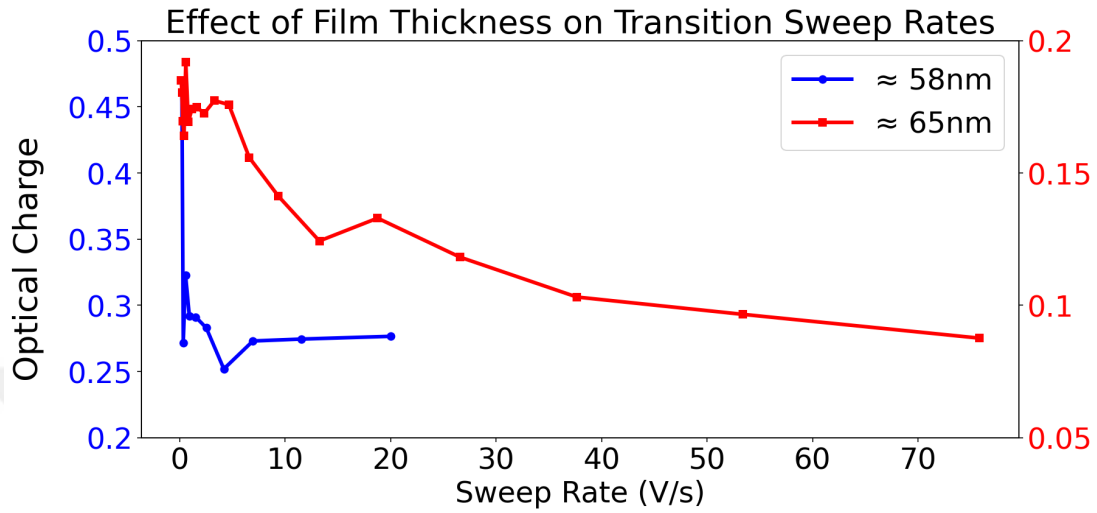

Figure 3.21: Effect of film thickness on the transition sweep rates. Optical charge is plotted as a function of sweep rate for films with thicknesses of approximately 58 nm (blue) and 65 nm (red).

In a diffusion-limited process, the optical charge is expected to reach a steady-state response as the sweep rate increases. As shown in Fig. 3.21, a similar behavior is observed here, where the coefficients converge at higher sweep rates, reflecting the transition to a non-diffusion-limited regime.

If the motion of ions penetrating into the polymer is hindered, this would imply that the oxidized polymer cannot be fully compensated by its counter-ions under charge neutrality conditions. In such a situation, if the polymer is still capable of undergoing a certain degree of color change, this indicates that (1) electrons can switch states even in the absence of sufficient ions, or (2) electron transfer can proceed independently of complete ionic compensation.

As a counter-argument, the observed decrease in the extent of color change could also be attributed to gradual degradation of the polymer, leading to a reduced ability to switch colors over time. To confirm or exclude this possibility, surface chemical spectroscopic techniques (XPS, ATR-IR) and microscopic/structural characterization methods (IR microscopy, SEM) of the used

or aged films may be required. In addition, for stability control, cyclic voltammetry and spectroscopic measurements of the same samples were repeated and compared.

While the first and second measurements were found to be in excellent agreement, after approximately five hours the effect of polymer degradation became evident. This is clearly reflected in the third measurement, where the coefficients decrease, indicating a diminished ability of the polymer to undergo reversible color switching. Furthermore, the color-switching capacity of the polymer was evaluated at very slow sweep rates both before and after the fast scans, and it was observed that the polymer retained its color-changing ability.

As shown in Fig. 3.22, consecutive measurements at fast sweep rates on polymer films of different thicknesses demonstrate the reproducibility of the extracted coefficients and confirm that the optical response is preserved during repeated cycling.

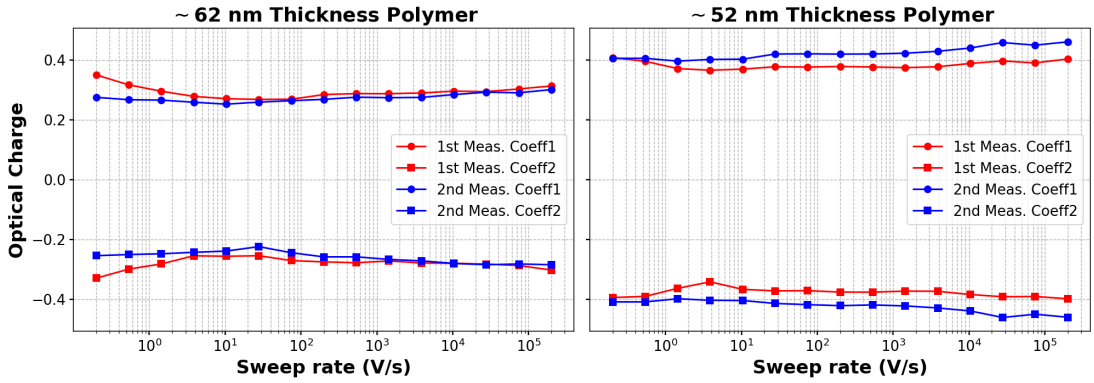

Figure 3.22: Consecutive measurements of the same polymer film at fast sweep rates. Both panels show the evolution of the extracted coefficients (Coeff1 and Coeff2) as a function of sweep rate The left panel corresponds to a $\sim$ 62 nm film, while the right panel corresponds to a $\sim$ 52 nm film. In each case, the first (red symbols) and second (blue symbols) measurements demonstrate the reproducibility of the optical response during consecutive cycling.

In conclusion, the subtracted coefficients were observed to level off at increasing sweep rates. To verify that this saturation and the decreasing trend of the coefficients were not caused by polymer degradation, consecutive measurements were carried out. These experiments confirmed that no significant degradation occurred during the first and second measurements, with minor signs of degradation only appearing in the third measurement after approximately five hours. Therefore, the limiting behavior of the coefficients is interpreted as a transition into a regime where ion diffusion becomes restricted, rather than as a consequence of polymer degradation.

As a final step, only the coefficients obtained during cyclic voltammetry will be examined in the following section. The focus will be on clarifying the physical meaning of these coefficients when they are not subtracted from a reference value.

Figure 3.19 presented the CV coefficients in the range of 0.1–1 V/s. Below, we observe the variation of the weighted contributions of the components as a function of sweep rate for polymer films of three different thicknesses. In the subsequent figure (Fig. 3.23), the basis spectra corresponding to these components are shown, i.e., the elements selected from the basis set that were used to generate the data.

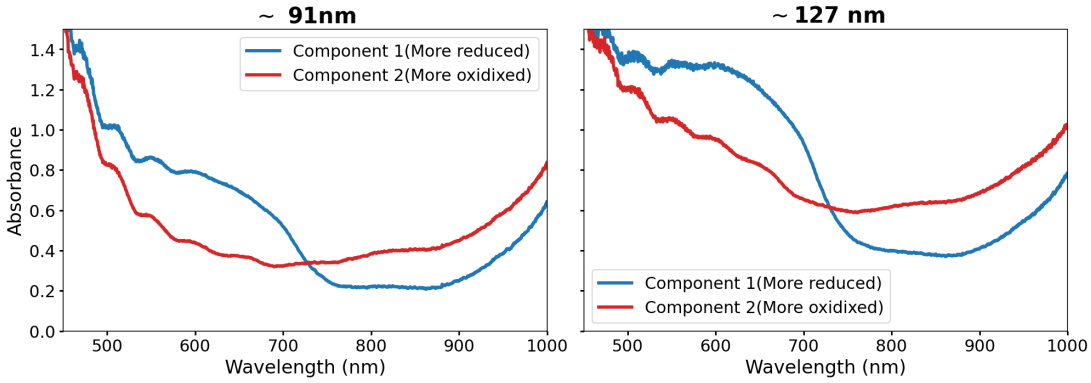

Figure 3.23: Basis set spectra corresponding to the components used in the analysis of cyclic voltammetry data.These spectra represent the characteristic absorbance features selected as basis elements, which were linearly combined through their coefficients to reconstruct the measured optical response.

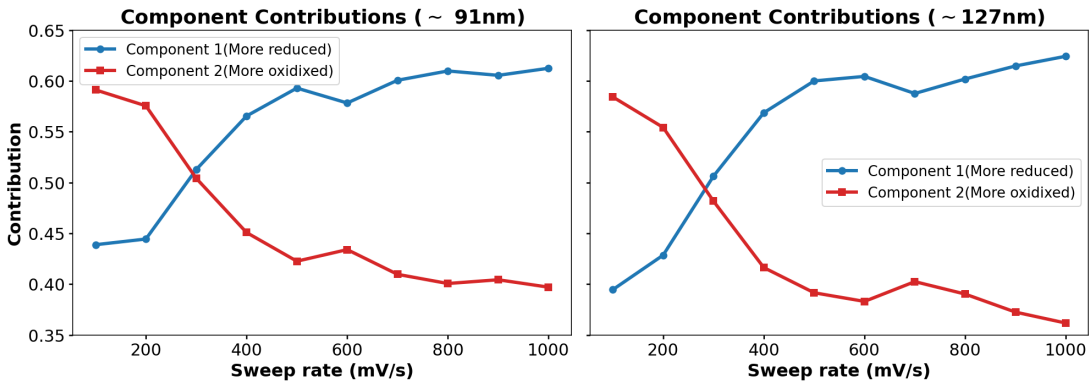

Figure 3.24: Weighted contributions of Component 1 and Component 2 as a function of sweep rate. (a) Film of ∼91 nm thickness; (b) Film of ∼127 nm thickness. These contributions were obtained from basis set fitting and represent the relative optical weight of reduced and oxidized states across sweep rates ranging from 100 to 1000 mV/s.

When Figures 3.24 and 3.25 are examined in parallel, it is evident that the coefficient corresponding to the more reduced component exhibits an increasing trend with increasing sweep rates. In contrast, the coefficient representing the more oxidized state of the polymer shows a decreasing trend in both examples. This behavior was not only observed in the cases presented here, but was consistently found in other measurements as well. Let us now focus on the physical meaning of this observation. Returning once again to the following equation,

$$\mathbf{A}(E,t) \;=\; \mathrm{coeff}_1(E,t)\,\mathbf{b}_1 \;+\; \mathrm{coeff}_2(E,t)\,\mathbf{b}_2,$$

At a given applied potential E and at time t, the absorbance spectrum can be expressed as the contribution of its individual components. However, here t corresponds to an average time. Considering, for instance, that a single cycle lasts on the order of 10^{-3} s, a 30 s measurement corresponds to approximately 30,000 cycles between -0.4 V and $+0.4$ V. At higher sweep rates this number increases even further. Thus, the extracted component represents the average response over all ∼30,000 cycles.

It is observed that the contribution of the more oxidized component decreases with increasing sweep rate. This indicates that oxidation of the polymer becomes more difficult at higher sweep rates, while the polymer spends more time in its reduced state. This directly demonstrates that the kinetics of oxidation and reduction in the polymer are not symmetric.

In conducting polymer films, the redox mechanism couples electron transfer along the polymer backbone with anion motion from the electrolyte. During oxidation, electrons are removed and ions are inserted (doping), while during reduction electrons are gained and anions leave (dedoping), enabling reversible changes in conductivity and optical properties.

$$\text{Polymer}^0 \underset{\text{reduction}}{\overset{\text{oxidation}}{\rightleftharpoons}} \text{Polymer}^+ + e^- \quad \text{(with ion insertion/extraction)}$$

Therefore, the decrease of the coefficient representing the oxidized contribution with increasing sweep rate indicates that the doping process, i.e., the insertion of ions, becomes limited. At slow scan rates, the polymer film has sufficient time to undergo doping, and thus the contribution of the oxidized state is high in fact, even larger than that of the reduced state. In contrast, as the sweep rate increases, this value decreases from about 0.6 to 0.4. Although the decrease is nonlinear, it tends to level off at higher sweep rates. On the other hand, since the polymer cannot be fully doped, the time spent in the reduced state, and consequently its contribution, increases. These two changes are complementary, and the rate of change is found to be nearly identical for the same sweep rate.

This observation further supports our assumption of the "optical charge," since the doping process is limited by the incomplete diffusion of ions, approaching a saturation limit that constrains the redox conversion.

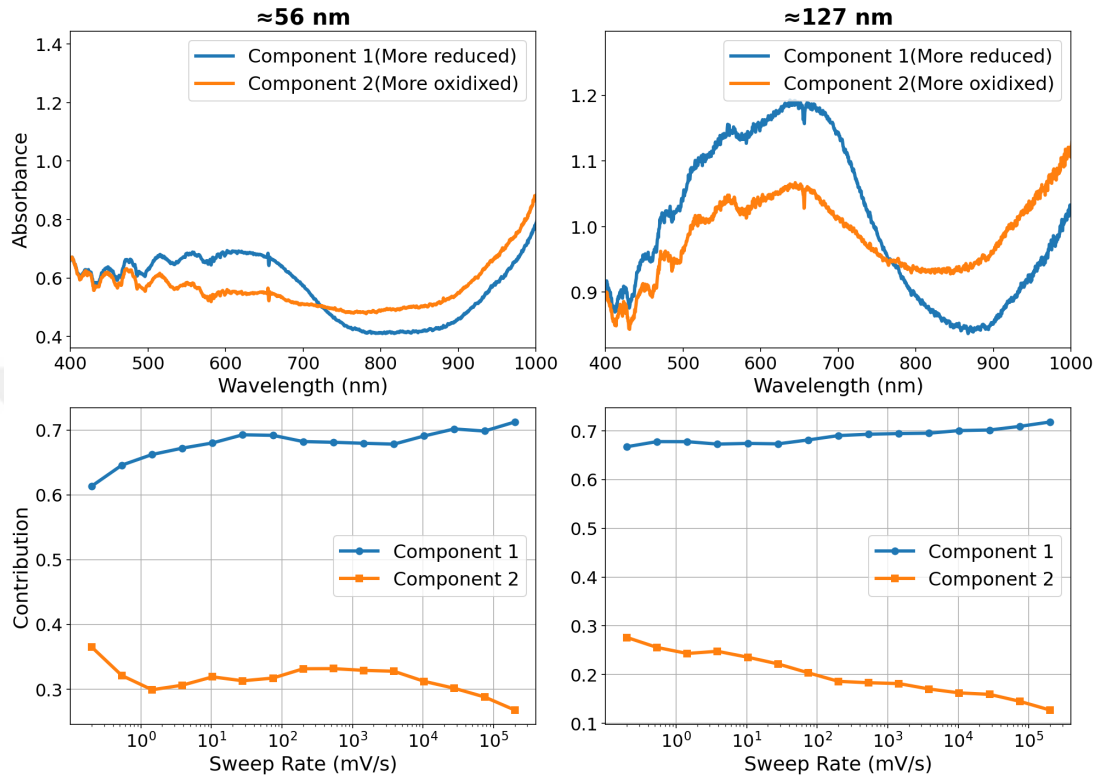

Figure 3.25: Contribution ratios of two spectral components as a function of scan rate for polymer films with thicknesses of approximately 56 nm and 127 nm. The semilogarithmic representation highlights the variation of Component 1 and Component 2 with increasing scan rates in the range of 0.2–200,000 $\mathrm{V\,s^{-1}}$.

In the case of slow scans (0.1–1 $\mathrm{V\,s^{-1}}$, Fig. 3.24), approximately ten data points were analyzed, providing a detailed view of the contribution changes within a narrow scan rate window. In contrast, for fast scans (0.2–200,000 $\mathrm{V\,s^{-1}}$, see Fig. 3.25), fifteen data points were collected, covering a much broader range of sweep rates. Within this extended regime, the same general trends were observed; however, due to the much higher sweep rates, the contribution of the oxidized component decreases far more significantly. Whereas in the slow scan regime the oxidized contribution stabilizes around a minimum of ∼0.35, in the fast scan regime it can drop as low as 0.1. This behavior highlights the parallelism between the physical processes occurring in the system and the mathematical coefficients extracted from the spectral deconvolution, further supporting the consistency of

the model.

Chapter 4

MODELING

In the *Results and Discussion* section, electrochemical analyses were first presented, which revealed that the capacitive nature of the conducting polymer obscures the underlying Faradaic response. As a result, it becomes impossible to isolate and analyze the current originating solely from the redox processes. In earlier studies, attempts were made to deconvolute the Faradaic current from the double-layer charging contribution in potential sweep voltammetry measurements by applying Iterative Target Transformation Factor Analysis (ITTFA) [110]. In another approach, which is also followed in this thesis, the cyclic voltammetry response of a one-dimensional ion-coupled polymer system was modeled by employing the fundamental transport equations (Nernst–Planck–Poisson) under the assumption of charge neutrality.

4.1 Setup

In this section, the mathematical and numerical framework employed to simulate ion and charge transport in the conducting polymer electrode is introduced. The system is represented by five coupled variables: the concentrations of positive and negative ions in the electrolyte (c^+, c^-), the Faradaic charge stored in the

polymer (Q_F), and the electrostatic potentials in the solid polymer (Φ_1) and the electrolyte solution (Φ_2). The spatial domain is one-dimensional, extending across the polymer electrode and the adjacent electrolyte diffusion layer with a total length $L = 1$ cm. The electrode porosity is explicitly included through the parameter e_p.

Governing Parameters and Constants

The transport and reaction processes are governed by ionic charges ($z^+ = +1$, $z^- = -1$), Faraday's constant ($F = 96485$ C mol^{-1}), the gas constant ($R = 8.314$ J mol^{-1} K^{-1}), and the temperature ($T = 298.15$ K). Effective transport coefficients are determined by correcting the bulk diffusion coefficients ($D^+ = 1.03 \times 10^{-5}$ cm^2 s^{-1}, $D^- = 1.81 \times 10^{-5}$ cm^2 s^{-1}) with the MacMullin number ($N_{\mathrm{ME,P}} = 10^6$) to account for the porous structure of the polymer.

The polymer film can exchange charge between oxidized and reduced states, with a maximum volumetric charge storage of $Q_{F,\max} = 344.65$ C cm^{-3}. The open-circuit potential is taken as $E_{\mathrm{OCP}} = 0.5$ V, and electron transfer kinetics are parameterized by the anodic and cathodic transfer coefficients ($\alpha_a = \alpha_c = 0.5$).

Domain Discretization and Initial Conditions

The one-dimensional electrode–electrolyte system is discretized into N_J grid points. The initial state vector is assigned as

$$c^+(x,0) = c^+_{\mathrm{bulk}}, \quad c^-(x,0) = c^-_{\mathrm{bulk}}, \quad Q_F(x,0) = Q_{F,\min}, \quad \Phi_1(x,0) = E_{\mathrm{app}}, \quad \Phi_2(x,0) = E_{\mathrm{ref}},$$

with bulk ionic concentrations $c^+_{\mathrm{bulk}} = c^-_{\mathrm{bulk}} = 0.1$ M.

Boundary and Interface Conditions

At the polymer/current collector boundary ($x = 0$), flux continuity and potential constraints are applied, including the prescribed applied potential E_{app}. At the electrolyte bulk boundary ($x = L$), the ionic concentrations are fixed at their bulk values, the solution potential is set to the reference E_{ref}, and the polymer charge is taken to vanish ($Q_F = 0$). At the polymer–electrolyte interface ($x = x_{\text{split}}$), special coupling conditions are enforced to guarantee continuity of fluxes and potentials across the heterogeneous domains.

Numerical Implementation

Spatial derivatives are approximated using second-order central finite differences with adaptive tolerance for grid resolution. The coupled algebraic system arising from discretization is assembled into block matrices (A, B, D, G, X, Y), which are combined into a banded structure. The resulting sparse linear system is solved iteratively using SciPy's sparse solver until convergence is achieved within a tolerance of 10^{-10}. At each iteration, the solution vector is updated and convergence is assessed based on the maximum absolute error between successive iterations.

This numerical setup enables the self-consistent calculation of ion concentration profiles, charge accumulation in the polymer, and potential distributions across the electrode/electrolyte system.

4.1.1 Linearization

Each governing equation in the polymer region, the polymer–electrolyte interphase, the bulk electrolyte, and the boundary conditions is inherently nonlinear, since the dependent variables (c^+, c^-, Q_F, Φ_1, and Φ_2) appear in coupled exponential and multiplicative forms. In order to solve the system numerically, these nonlinear equations must be *linearized*, that is, approximated by a set of linear

algebraic equations around the current iteration point.

In practice, this involves expanding the nonlinear terms into a first-order Taylor series around the present estimate of the solution vector.

The process of linearization therefore provides a systematic way to incrementally update the solution by repeatedly solving a linearized problem until convergence to the nonlinear solution is achieved.

Polymer electrode region

Variables	**Governing equations**
$\mathbf{c_+}$	$\frac{\partial(\varepsilon_p c_+)}{\partial t} = z_+ F \frac{\partial}{\partial x}\left(u_{+,p} c_+ \frac{\partial \Phi_2}{\partial x}\right) + \frac{\partial}{\partial x}\left(D_{+,p}\frac{\partial c_+}{\partial x}\right) - \frac{s_+}{nF} aj$
$\mathbf{c_-}$	$\frac{\partial(\varepsilon_p c_-)}{\partial t} = z_- F \frac{\partial}{\partial x}\left(u_{-,p} c_- \frac{\partial \Phi_2}{\partial x}\right) + \frac{\partial}{\partial x}\left(D_{-,p}\frac{\partial c_-}{\partial x}\right) - \frac{s_-}{nF} aj$
$\mathbf{Q_f}$	$\frac{\partial Q_f}{\partial t} = aj$
$\mathbf{\Phi_1}$	$aj = \frac{\partial}{\partial x}\left(\sigma_p \frac{\partial \Phi_1}{\partial x}\right)$
$\mathbf{\Phi_2}$	$\sum_i z_i c_i = 0$

Where:

$$aj = ai_{0,\mathrm{ref}} \left\{ (1-\theta)\left(\frac{c_-}{c_{-,\mathrm{ref}}}\right) \exp\left(\frac{\alpha_a F \eta}{RT}\right) - \theta_{\exp} \exp\left(-\frac{\alpha_c F \eta}{RT}\right) \right\}$$

$$a_j = ai_{0,\text{ref}} \left\{ \left(\frac{Q_{F,\text{MAX}} - Q_F}{Q_{F,\text{MAX}}} \right) \left(\frac{c_-}{c_{-,\text{REF}}} \right) \exp\left(\frac{\alpha_a F \eta}{RT} \right) - \left(\frac{Q_F}{Q_{F,\text{MAX}}} \right) \exp\left(-\frac{\alpha_c F \eta}{RT} \right) \right\}$$

Variable	Description	Unit
c_+	Concentration of cations in polymer/electrolyte phase	
c_-	Concentration of anions in polymer/electrolyte phase	
Φ_1	Potential in the electronically conducting polymer (solid) phase	
Φ_2	Potential in the electrolyte phase	
Q	Faradaic charge stored in the polymer per unit volume	

Parameter	Description	Unit
a	Specific surface area of the polymer electrode	
$i_{0,\text{ref}}$	Exchange current density at reference concentration	
$Q_{\max}$	Maximum charge capacity of the polymer	
$c_{-,\text{Ref}}$	Reference anion concentration	
α_a	Anodic charge transfer coefficient	
α_c	Cathodic charge transfer coefficient	
F	Faraday constant	
R	Universal gas constant	
T	Absolute temperature	
η	Overpotential: $\eta = \Phi_1 - \Phi_2 - E_{\text{eq}}$	
ϵ_p	Porosity of the polymer film	

The governing equation for the concentration of cations c_+ in the polymer phase can be split into four components to simplify the calculations. :

Time-dependent accumulation of c_+ This term represents the rate of change of cation concentration in time within the porous polymer phase:

$$\frac{\partial(\varepsilon_p c_+)}{\partial t} \tag{4.1}$$

The second term accounts for the movement of cations due to the electric field:

$$z_+ F \frac{\partial}{\partial x}\left(u_{+,p} c_+ \frac{\partial \Phi_2}{\partial x}\right) \tag{4.2}$$

This is the electromigration term where $u_{+,p}$ is the ionic mobility.

The third term describes diffusion due to concentration gradients:

$$\frac{\partial}{\partial x}\left(D_{+,p} \frac{\partial c_+}{\partial x}\right) \tag{4.3}$$

Where $D_{+,p}$ is the effective diffusion coefficient of the cation in the polymer.

The final term due to the electrochemical reaction:

$$-\frac{s_+}{nF} aj \tag{4.4}$$

The full equation governs the time evolution of cation concentration under the influence of electromigration, diffusion, and electrochemical reaction.

$$\frac{\partial(\varepsilon_p C_+)}{\partial t} = z_+ F \frac{\partial}{\partial x}\left(u_{+,p} C_+ \frac{\partial \phi_2}{\partial x}\right) + \frac{\partial}{\partial x}\left(D_{+,p} \frac{\partial C_+}{\partial x}\right) - \frac{s_+ aj}{nF} \tag{4.5}$$

The next step is to linearize the divided parts of the equations. We will start with the first part:

$$\frac{\partial(\varepsilon_p C_+)}{\partial t} = \frac{\varepsilon_p \Delta C_+}{\Delta t} = \frac{\varepsilon_p C_+}{\Delta t} - \frac{\varepsilon_p C_+^p}{\Delta t} \tag{4.6}$$

Next comes the second part, which corresponds to electromigration:

$$\alpha_{+,p}\frac{\partial}{\partial x}\left(C_+\frac{\partial\phi_2}{\partial x}\right) \tag{4.7}$$

Where,

$$u_{+,p}=\frac{D_{+,p}}{RT} \qquad \Rightarrow \qquad z_+Fu_{+,p}=\frac{z_+FD_{+,p}}{RT}=\alpha_{+,p} \tag{4.8}$$

Defining: $C_+=C_+^p+\Delta C_+$ and $\phi_2=\phi_2^p+\Delta\phi_2$. Inserting these into Equation (4.7) gives the following:

$$\alpha_{+,p}\frac{\partial}{\partial x}\left[(C_+^p+\Delta C_+)\left(\frac{\partial\phi_2^p}{\partial x}+\frac{\partial\Delta\phi_2}{\partial x}\right)\right] \tag{4.9}$$

$$\alpha_{+,p}\frac{\partial}{\partial x}\left[C_+^p\frac{\partial\phi_2^p}{\partial x}+C_+^p\frac{\partial\Delta\phi_2}{\partial x}+\Delta C_+\frac{\partial\phi_2^p}{\partial x}+\Delta C_+\frac{\partial\Delta\phi_2}{\partial x}\right] \tag{4.10}$$

$$\begin{aligned}\alpha_{+,p}\Bigg[&\frac{\partial C_+^p}{\partial x}\frac{\partial\phi_p^2}{\partial x}+C_+^p\frac{\partial^2\phi_2^p}{\partial x^2}+\frac{\partial C_+^p}{\partial x}\frac{\partial\Delta\phi_2}{\partial x}\\&+C_+^p\frac{\partial^2\Delta\phi_2}{\partial x^2}+\frac{\partial\Delta C_+}{\partial x}\frac{\partial\phi_2^p}{\partial x}+\Delta C_+\frac{\partial^2\phi_2^p}{\partial x^2}\\&+\boxed{\Delta C_+\frac{\partial^2\Delta\phi_2}{\partial x^2}\quad\text{(Neglected)}}\Bigg]\end{aligned} \tag{4.11}$$

$$\begin{aligned}\alpha_{+,p}\Bigg[&\frac{\partial C_+^p}{\partial x}\frac{\partial\phi_p^2}{\partial x}+C_+^p\frac{\partial^2\phi_2^p}{\partial x^2}+\frac{\partial C_+^p}{\partial x}\frac{\partial\Delta\phi_2}{\partial x}\\&+C_+^p\frac{\partial^2\Delta\phi_2}{\partial x^2}+\frac{\partial\Delta C_+}{\partial x}\frac{\partial\phi_2^p}{\partial x}+\Delta C_+\frac{\partial^2\phi_2^p}{\partial x^2}\Bigg]\end{aligned} \tag{4.12}$$

We define the perturbed components of potential and concentration as differences from their previous values.

$$\Delta\phi_2=\phi_2-\phi_2^p \qquad \text{and} \qquad \Delta C_+=C_+-C_+^p \tag{4.13}$$

By substituting the difference expressions into the equation (4.12), we proceed with back-substitution to obtain the coefficients of the variables themselves.

$$\begin{aligned}\alpha_{+,p}\Bigg[& \frac{\partial C_+^p}{\partial x}\frac{\partial \phi_2^p}{\partial x} + C_+^p \frac{\partial^2 \phi_2^p}{\partial x^2} \\ & + \frac{\partial C_+^p}{\partial x}\left(\frac{\partial \phi_2}{\partial x} - \frac{\partial \phi_2^p}{\partial x}\right) \\ & + C_+^p \left(\frac{\partial^2 \phi_2}{\partial x^2} - \frac{\partial^2 \phi_2^p}{\partial x^2}\right) \\ & + \left(\frac{\partial C_+}{\partial x} - \frac{\partial C_+^p}{\partial x}\right)\frac{\partial \phi_2^p}{\partial x} \\ & + (C_+ - C_+^p)\frac{\partial^2 \phi_2^p}{\partial x^2}\Bigg]\end{aligned} \tag{4.14}$$

$$\begin{aligned}\alpha_{+,p}\Bigg[& \frac{\partial C_+^p}{\partial x}\frac{\partial \phi_2^p}{\partial x} + C_+^p \frac{\partial^2 \phi_2^p}{\partial x^2} + \frac{\partial C_+^p}{\partial x}\frac{\partial \phi_2}{\partial x} - \frac{\partial C_+^p}{\partial x}\frac{\partial \phi_2^p}{\partial x} \\ & + C_+^p \frac{\partial^2 \phi_2}{\partial x^2} - C_+^p \frac{\partial^2 \phi_2^p}{\partial x^2} + \frac{\partial C_+}{\partial x}\frac{\partial \phi_2^p}{\partial x} - \frac{\partial C_+^p}{\partial x}\frac{\partial \phi_2^p}{\partial x} \\ & + C_+ \frac{\partial^2 \phi_2^p}{\partial x^2} - C_+^p \frac{\partial^2 \phi_2^p}{\partial x^2}\Bigg]\end{aligned} \tag{4.15}$$

Finally part 2 could be obtained as:

$$\alpha_{+,p}\left[\frac{\partial C_+^p}{\partial x}\frac{\partial \phi_2}{\partial x} + C_+^p \frac{\partial^2 \phi_2}{\partial x^2} + \frac{\partial \phi_2^p}{\partial x}\frac{\partial C_+}{\partial x} - \frac{\partial \phi_2^p}{\partial x}\frac{\partial C_+^p}{\partial x} + C_+ \frac{\partial^2 \phi_2^p}{\partial x^2} - C_+^p \frac{\partial^2 \phi_2^p}{\partial x^2}\right] \tag{4.16}$$

Part 3 is the diffusion part:

$$\frac{\partial}{\partial x}\left(D_{+,p}\frac{\partial C_+}{\partial x}\right) \Rightarrow D_{+,p}\frac{\partial}{\partial x}\left(\frac{\partial C_+^p}{\partial x}+\frac{\partial \Delta C_+}{\partial x}\right) \tag{4.17}$$

$$\Rightarrow D_{+,p}\frac{\partial}{\partial x}\left(\frac{\partial C_+^p}{\partial x}+\frac{\partial C_+}{\partial x}-\frac{\partial C_+^p}{\partial x}\right) \tag{4.18}$$

$$\Rightarrow D_{+,p}\frac{\partial}{\partial x}\left(\frac{\partial C_+}{\partial x}\right) \tag{4.19}$$

$$= D_{+,p}\frac{\partial^2 C_+}{\partial x^2} \tag{4.20}$$

The final part is the electrochemical reaction term. After linearizing this part, we can combine all components and construct the equation table for the first variable, C_+.

$$-\frac{S_+}{nF}\,ai_{0,\mathrm{ref}}\left\{\left(\frac{Q_{\max}-Q}{Q_{\max}}\right)\left(\frac{C_-}{C_{-,\mathrm{ref}}}\right)e^{\frac{\alpha_a F\eta}{RT}}-\left(\frac{Q}{Q_{\max}}\right)e^{-\frac{\alpha_c F\eta}{RT}}\right\} \tag{4.21}$$

Defining:

$$\frac{S_+\,ai_{0,\mathrm{ref}}}{nF}=\sigma_+,\quad \frac{\alpha_a F}{RT}=\chi_a,\quad \frac{\alpha_c F}{RT}=\chi_c,\quad \eta=\phi_1-\phi_{\mathrm{re}}-(\phi_2-\phi_{\mathrm{re}})-\phi_{\mathrm{Eq}} \tag{4.22}$$

$$-\sigma_+\left\{\left(\frac{Q_{\max}-Q}{Q_{\max}}\right)\left(\frac{C_-}{C_{-,\mathrm{ref}}}\right)e^{\chi_a\eta}-\left(\frac{Q}{Q_{\max}}\right)e^{-\chi_c\eta}\right\} \tag{4.23}$$

$$Q=Q^p+\Delta Q,\quad C_-=C_-^p+\Delta C_-,\quad \eta=\eta^p+\Delta\eta \tag{4.24}$$

$$-\sigma_+\left\{\frac{1}{Q_{\max}C_{-,\mathrm{ref}}}\left(Q_{\max}-Q\right)C_-\,e^{\chi_a\eta}-\left(\frac{1}{Q_{\max}}\right)Q\,e^{-\chi_c\eta}\right\} \tag{4.25}$$

$$-\sigma_+\Bigg\{\left(\frac{1}{Q_{\max}\,C_{-,\mathrm{ref}}}\right)(Q_{\max}-Q^p-\Delta Q)\,(C_-^p+\Delta C_-)\,e^{\chi_a(\eta^p+\Delta\eta)} - \left(\frac{1}{Q_{\max}}\right)(Q^p+\Delta Q)\,e^{-\chi_c(\eta^p+\Delta\eta)}\Bigg\} \tag{4.26}$$

$$e^{\chi_a(\eta^p+\Delta\eta)} \approx e^{\chi_a\eta^p}\,(1+\chi_a\Delta\eta) \tag{4.27}$$

$$e^{-\chi_c(\eta^p+\Delta\eta)} \approx e^{-\chi_c\eta^p}\,(1-\chi_c\Delta\eta) \tag{4.28}$$

$$\eta=\phi_1-\phi_2-U_{\mathrm{ref}} \quad\Rightarrow\quad e^{\chi_a\eta}=e^{\chi_a\phi_1}\,e^{-\chi_a\phi_2}\,e^{-\chi_aU_{\mathrm{Eq}}}$$

$$-\sigma_+\Bigg\{\frac{e^{-\chi_aU_{\mathrm{Eq}}}\,e^{\chi_a\phi_1^p}\,e^{-\chi_a\phi_2^p}}{Q_{\max}\,C_{-,\mathrm{ref}}}(Q_{\max}-Q^p-\Delta Q)\,(C_-^p+\Delta C_-)\,(1+\chi_a\Delta\eta) - \frac{e^{-\chi_cU_{\mathrm{Eq}}}\,e^{\chi_c\phi_2^p}\,e^{-\chi_c\phi_1^p}}{Q_{\max}}(Q^p+\Delta Q)\,(1-\chi_c\Delta\eta)\Bigg\} \tag{4.29}$$

Defining ,

$$A=\frac{e^{-\chi_aU_{\mathrm{Eq}}}\,e^{\chi_a\phi_1^p}\,e^{-\chi_a\phi_2^p}}{Q_{\max}\,C_{-,\mathrm{ref}}} \tag{4.30}$$

$$C=\frac{e^{-\chi_cU_{\mathrm{Eq}}}\,e^{\chi_c\phi_2^p}\,e^{-\chi_c\phi_1^p}}{Q_{\max}} \tag{4.31}$$

The simplified version of Equation 4.29 becomes:

$$-\sigma_+\left\{A\,(Q_{\max}-Q^p-\Delta Q)\,(C_-^p+\Delta C_-)\,(1+\chi_a\Delta\eta)-C\,(Q^p+\Delta Q)\,(1-\chi_c\Delta\eta)\right\} \tag{4.32}$$

$$-\sigma_+\Big\{A\Big[Q_{\max}C_-^p + Q_{\max}\Delta C_- - Q^pC_-^p - Q^p\Delta C_- - \Delta Q\,C_-^p - \cancel{\Delta Q\,\Delta C_-}\Big](1+\chi_a\Delta\eta)$$
$$- C\Big[Q^p - Q^p\chi_c\Delta\eta + \Delta Q - \cancel{\Delta Q\chi_c\Delta\eta}\Big]\Big\} \tag{4.33}$$

$$\begin{aligned}-\sigma_+\Big\{A\Big[&Q_{\max}C_-^p + Q_{\max}C_-^p\,\chi_a\Delta\eta + Q_{\max}\Delta C_- + \cancel{Q_{\max}\Delta C_-\,\chi_a\Delta\eta}\\ &- Q^pC_-^p - Q^pC_-^p\,\chi_a\Delta\eta - Q^p\Delta C_- - \cancel{Q^p\Delta C_-\,\chi_a\Delta\eta}\\ &- \Delta Q\,C_-^p - \cancel{\Delta Q\,C_-^p\,\chi_a\Delta\eta}\Big]\\ &- C\Big[Q^p - Q^p\chi_c\Delta\eta + \Delta Q\Big]\Big\}\end{aligned} \tag{4.34}$$

Again we perform back substitution,

$$\Delta\eta = \eta - \eta^p \tag{4.35}$$
$$\Delta C_- = C_- - C_-^p \tag{4.36}$$
$$\Delta Q = Q - Q^p \tag{4.37}$$

Equation 4.34 becomes:

$$\begin{aligned}-\sigma_+\Big\{A\Big[&Q_{\max}C_-^p + Q_{\max}C_-^p\chi_a(\eta-\eta^p) + Q_{\max}(C_- - C_-^p)\\ &- Q^pC_-^p - Q^pC_-^p\chi_a(\eta-\eta^p) - Q^p(C_- - C_-^p) - (Q-Q_p)C_-^p\Big]\\ &- C\Big[Q^p - Q^p\chi_c(\eta-\eta^p) + Q - Q^p\Big]\Big\}\end{aligned} \tag{4.38}$$

Rearranging the multiplication,

$$\begin{aligned}-\sigma_+\Big\{A\Big[&\cancel{Q_{\max}C_-^p} + Q_{\max}C_-^p\chi_a\eta - Q_{\max}C_-^p\chi_a\eta^p + Q_{\max}C_-\\ &- \cancel{Q_{\max}C_-^p} - \cancel{Q^pC_-^p} - Q^pC_-^p\chi_a\eta + Q^pC_-^p\chi_a\eta^p\\ &- Q^pC_- + \cancel{Q^pC_-^p} - QC_-^p + Q^pC_-^p\Big]\\ &- C\Big[\cancel{Q^p} - Q^p\chi_c\eta + Q^p\chi_c\eta^p + Q - \cancel{Q^p}\Big]\Big\}\end{aligned} \tag{4.39}$$

Finally, Rearranging the multiplication,

$$
\begin{aligned}
-\sigma_+\Big\{ A\Big[& Q_{\max} C_-^p \chi_a \eta - Q_{\max} C_-^p \chi_a \eta^p + Q_{\max} C_- \\
& - Q^p C_-^p \chi_a \eta + Q^p C_-^p \chi_a \eta^p - Q^p C_- - Q C_-^p + Q^p C_-^p \Big] \\
& - C\Big[- Q^p \chi_c \eta + Q^p \chi_c \eta^p + Q \Big] \Big\}
\end{aligned} \tag{4.40}
$$

Now we can combine all parts to obtain the complete linearized equation. Equations 4.6 , 4.16 , 4.20 and 4.40 :

$$
\begin{aligned}
\varepsilon_p \frac{C_+}{\Delta t} - \varepsilon_p \frac{C_+^p}{\Delta t} = \alpha_{+,p} \Bigg[& \frac{\partial C_+^p}{\partial x}\frac{\partial \phi_2}{\partial x} + C_+^p \frac{\partial^2 \phi_2}{\partial x^2} + \frac{\partial \phi_2^p}{\partial x}\frac{\partial C_+}{\partial x} \\
& - \frac{\partial \phi_2^p}{\partial x}\frac{\partial C_+^p}{\partial x} + C_+ \frac{\partial^2 \phi_2^p}{\partial x^2} - C_+^p \frac{\partial^2 \phi_2^p}{\partial x^2} \Bigg] \\
& + D_{+,p} \frac{\partial^2 C_+}{\partial x^2} \\
& - \sigma_+ \Bigg\{ A\Big[Q_{\max} C_-^p \chi_a \eta - Q_{\max} C_-^p \chi_a \eta^p + Q_{\max} C_- \\
& \quad - Q^p C_-^p \chi_a \eta + Q^p C_-^p \chi_a \eta^p - Q^p C_- - Q C_-^p + Q^p C_-^p \Big] \\
& \quad - C\Big[- Q^p \chi_c \eta + Q^p \chi_c \eta^p + Q \Big] \Bigg\}
\end{aligned} \tag{4.41}
$$

The left-hand side of the equation(4.42) consists of the unknown variables, while the right-hand side contains the constant values.

$$
\begin{aligned}
\varepsilon_p \frac{C_+}{\Delta t} &- \alpha_{+,p}\left[\frac{\partial C_+^p}{\partial x}\frac{\partial \phi_2}{\partial x} + C_+^p \frac{\partial^2 \phi_2}{\partial x^2} + \frac{\partial \phi_2^p}{\partial x}\frac{\partial C_+}{\partial x} + C_+ \frac{\partial^2 \phi_2^p}{\partial x^2}\right] - D_{+,p}\frac{\partial^2 C_+}{\partial x^2} \\
&+ \sigma_+\left\{A\Big[Q_{\max}C_-^p\chi_a\eta + Q_{\max}C_- - Q^pC_-^p\chi_a\eta - Q^pC_- - QC_-^p\Big] - C\Big[Q - Q^p\chi_c\eta\Big]\right\} \\
&= \alpha_{+,p}\left[-\frac{\partial \phi_2^p}{\partial x}\frac{\partial C_+^p}{\partial x} - C_+^p\frac{\partial^2 \phi_2^p}{\partial x^2}\right] \\
&\quad - \sigma_+\left\{A\Big[-Q_{\max}C_-^p\chi_a\eta^p + Q^pC_-^p\chi_a\eta^p + Q^pC_-^p\Big] + CQ^p\chi_c\eta^p\right\} + \varepsilon_p\frac{C_+^p}{\Delta t}
\end{aligned}
\tag{4.42}
$$

Next step is the construction of the equation table.

Equation for: C_+	**a**	**b**	**d**
C_+	$-D_{+,p}$	$-\alpha_{+,p}\frac{\partial \phi_2^p}{\partial x}$	$\frac{\varepsilon_p}{\Delta t} - \alpha_{+,p}\frac{\partial^2 \phi_2^p}{\partial x^2}$
C_-	0	0	$-\sigma_+ A\left(Q_{\max} - Q^p\right)$
Q	0	0	$-\sigma_+ AC_-^p - \sigma_+ C$
ϕ_1	0	0	$\sigma_+ AC_-^p\chi_a(Q_{\max} - Q^p) + \sigma_+ CQ^p\chi_c$
ϕ_2	$-\alpha_{+,p}C_+^p$	$-\alpha_{+,p}\frac{\partial C_+^p}{\partial x}$	$-\sigma_+ AC_-^p\chi_a(Q_{\max} - Q^p) - \sigma_+ CQ^p\chi_c$

Table 4.1: Coefficient matrix terms for variable C_+ in finite difference discretization

$$
\begin{aligned}
g = &\alpha_{+,p}\left[-\frac{\partial \phi_2^p}{\partial x}\frac{\partial C_+^p}{\partial x} - C_+^p\frac{\partial^2 \phi_2^p}{\partial x^2}\right] \\
&- \sigma_+\left\{A\Big[-Q_{\max}C_-^p\chi_a\eta^p + Q^pC_-^p\chi_a\eta^p + Q^pC_-^p\Big] + CQ^p\chi_c\right\} \\
&+ \varepsilon_p\frac{C_+^p}{\Delta t}
\end{aligned}
$$

Similar calculations should be performed for the other variables. For C_-, the final equation and the corresponding equation table are as follows:

$$
\begin{aligned}
&\varepsilon_p \frac{C_-}{\Delta t} - \alpha_{-,p}\left[\frac{\partial C_-^p}{\partial x}\frac{\partial \phi_2}{\partial x} + C_-^p\frac{\partial^2 \phi_2}{\partial x^2} + \frac{\partial \phi_2^p}{\partial x}\frac{\partial C_-}{\partial x} + C_-\frac{\partial^2 \phi_2^p}{\partial x^2}\right] - D_{-,p}\frac{\partial^2 C_-}{\partial x^2} \\
&\quad + \sigma_-\left\{A\Big[Q_{\max}C_-^p\chi_a\eta + Q_{\max}C_- - Q^pC_-^p\chi_a\eta - Q^pC_- - QC_-^p\Big] - C\Big[Q - Q^p\chi_c\eta\Big]\right\} \\
&\quad = \alpha_{-,p}\left[-\frac{\partial \phi_2^p}{\partial x}\frac{\partial C_-^p}{\partial x} - C_-^p\frac{\partial^2 \phi_2^p}{\partial x^2}\right] \\
&\qquad - \sigma_-\left\{A\Big[-Q_{\max}C_-^p\chi_a\eta^p + Q^pC_-^p\chi_a\eta^p + Q^pC_-^p\Big] + CQ^p\chi_c\eta^p\right\} + \varepsilon_p\frac{C_-^p}{\Delta t}
\end{aligned}
\tag{4.43}
$$

Equation for: C_-	**a**	**b**	**d**
C_+	0	0	0
C_-	$-D_{-,p}$	$-\alpha_{-,p}\frac{\partial \phi_2^p}{\partial x}$	$\frac{\varepsilon_p}{\Delta t} - \alpha_{-,p}\frac{\partial^2 \phi_2^p}{\partial x^2} + \sigma_- A(Q_{max} - Q^p)$
Q	0	0	$-\sigma_- AC_-^p - \sigma_- C$
ϕ_1	0	0	$\sigma_- AC_-^p\chi_a(Q_{max} - Q^p) + \sigma_- CQ^p\chi_c$
ϕ_2	$-\alpha_{-,p}C_-^p$	$-\alpha_{-,p}\frac{\partial C_-^p}{\partial x}$	$-\sigma_- AC_-^p\chi_a(Q_{max} - Q^p) - \sigma_- CQ^p\chi_c$

Table 4.2: Coefficient matrix terms for variable C_-

$$
\begin{aligned}
g =& \alpha_{-,p}\left[-\frac{\partial \phi_2^p}{\partial x}\frac{\partial C_-^p}{\partial x} - C_-^p\frac{\partial^2 \phi_2^p}{\partial x^2}\right] \\
&- \sigma_-\left\{A\Big[-Q_{\max}C_-^p\chi_a\eta^p + Q^pC_-^p\chi_a\eta^p + Q^pC_-^p\Big] + CQ^p\chi_c\eta^p\right\} \\
&+ \varepsilon_p\frac{C_-^p}{\Delta t}
\end{aligned}
$$

Next variable is charge, Q,

$$\frac{\partial Q}{\partial t} = a_j \tag{4.44}$$

$$\Rightarrow \quad \frac{Q - Q^p}{\Delta t} = a\, i_{0,\text{ref}} \Bigg\{ A \Big[Q_{\max} C_-^p \chi_a \eta - Q_{\max} C_-^p \chi_a \eta^p + Q_{\max} C_- - Q^p C_-^p \chi_a \eta + Q^p C_-^p \chi_a \eta^p - Q^p C_- - Q C_-^p + Q^p C_-^p \Big] - C \Big[Q - Q^p \chi_c + Q^p \chi_c \eta^p \Big] \Bigg\} \tag{4.45}$$

$$\frac{Q}{\Delta t} - a\, i_{0,\text{ref}} \left\{ A \left[Q_{\max} C_-^p \chi_a \eta + Q_{\max} C_- - Q^p C_-^p \chi_a \eta - Q^p C_- - Q C_-^p \right] - C \left[Q - Q^p \chi_c \eta \right] \right\} = a\, i_{0,\text{ref}} \left\{ A \left[-Q_{\max} C_-^p \chi_a \eta^p + Q^p C_-^p \chi_a \eta^p + Q^p C_-^p \right] + C Q^p \chi_c \eta^p \right\} + \frac{Q^p}{\Delta t} \tag{4.46}$$

Equaiton for: Q	**a**	**b**	**d**
C_+	0	0	0
C_-	0	0	$-a\, i_{0,\text{ref}}\, A\, (Q_{max} - Q^p)$
Q	0	0	$\frac{1}{\Delta t} + a\, i_{0,\text{ref}} A C_-^p + a\, i_{0,\text{ref}} C$
ϕ_1	0	0	$-a\, i_{0,\text{ref}} A C_-^p \chi_a\, (Q_{max} - Q^p) - a\, i_{0,\text{ref}} C \chi_c Q^p$
ϕ_2	0	0	$a\, i_{0,\text{ref}} A C_-^p \chi_a\, (Q_{max} - Q^p) + a\, i_{0,\text{ref}} C \chi_c Q_F^p$

Table 4.3: Coefficient matrix terms for variable Q

$$g = a\, i_{0,\text{ref}} A \Big[C_-^p Q^p - C^p Q_{\max} \chi_a (\phi_1^p - \phi_2^p) + C_-^p Q^p \chi_a (\phi_1^p - \phi_2^p) \Big] - a\, i_{0,\text{ref}} C Q^p \chi_c (\phi_1^p - \phi_2^p) + \frac{Q^p}{\Delta t}$$

The next variable is ϕ_1.

$$a_j = \frac{\partial}{\partial x} \left(\rho_p \frac{\partial \phi_1}{\partial x} \right) \Rightarrow a_j = \frac{\partial \rho_p}{\partial x} \frac{\partial \phi_1}{\partial x} + \rho_p \frac{\partial^2 \phi_1}{\partial x^2} \tag{4.47}$$

$$\rho_p = \left(\frac{\rho_{\min} - \rho_{\max}}{Q_{\min} - Q_{\max}} \right) (Q - Q_{\max}) + \rho_{\max} = kQ - kQ_{\max} + \rho_{\max} \tag{4.48}$$

$$a_j = k \frac{\partial Q}{\partial x} \frac{\partial \phi_1}{\partial x} + (kQ - kQ_{\max} + \rho_{\max}) \left(\frac{\partial^2 \phi_1}{\partial x^2} \right) \tag{4.49}$$

$$a_j = k \frac{\partial Q}{\partial x} \cdot \frac{\partial \phi_1}{\partial x} + kQ \cdot \frac{\partial^2 \phi_1}{\partial x^2} - kQ_{\max} \cdot \frac{\partial^2 \phi_1}{\partial x^2} + \rho_{\max} \cdot \frac{\partial^2 \phi_1}{\partial x^2} \tag{4.50}$$

$$\begin{aligned} a_j = {} & k \left(\frac{\partial Q^p}{\partial x} + \frac{\partial \Delta Q}{\partial x} \right) \left(\frac{\partial \phi_1^p}{\partial x} + \frac{\partial \Delta \phi_1}{\partial x} \right) \\ & + k(Q^p + \Delta Q) \left(\frac{\partial^2 \phi_1^p}{\partial x^2} + \frac{\partial^2 \Delta \phi_1}{\partial x^2} \right) \\ & - kQ_{\max} \left(\frac{\partial^2 \phi_1^p}{\partial x^2} + \frac{\partial^2 \Delta \phi_1}{\partial x^2} \right) \\ & + \rho_{\max} \left(\frac{\partial^2 \phi_1^p}{\partial x^2} + \frac{\partial^2 \Delta \phi_1}{\partial x^2} \right) \end{aligned} \tag{4.51, 4.52}$$

$$\begin{aligned} a_j = {} & k \left(\frac{\partial Q^p}{\partial x} \cdot \frac{\partial \phi_1^p}{\partial x} + \frac{\partial Q^p}{\partial x} \cdot \frac{\partial \Delta \phi_1}{\partial x} + \frac{\partial \Delta Q}{\partial x} \cdot \frac{\partial \phi_1^p}{\partial x} + \cancel{\frac{\partial \Delta Q}{\partial x} \cdot \frac{\partial \Delta \phi_1}{\partial x}} \right) \\ & + kQ^p \cdot \frac{\partial^2 \phi_1^p}{\partial x^2} + kQ^p \cdot \frac{\partial^2 \Delta \phi_1}{\partial x^2} + k\Delta Q \cdot \frac{\partial^2 \phi_1^p}{\partial x^2} + \cancel{k\Delta Q \cdot \frac{\partial^2 \Delta \phi_1}{\partial x^2}} \\ & - kQ_{\max} \cdot \frac{\partial^2 \phi_1^p}{\partial x^2} - kQ_{\max} \cdot \frac{\partial^2 \Delta \phi_1}{\partial x^2} \\ & + \rho_{\max} \cdot \frac{\partial^2 \phi_1^p}{\partial x^2} + \rho_{\max} \cdot \frac{\partial^2 \Delta \phi_1}{\partial x^2} \end{aligned} \tag{4.53}$$

$$
\begin{aligned}
a_j = & k\frac{\partial Q^p}{\partial x}\cdot\frac{\partial \phi_1^p}{\partial x} \\
& + k\frac{\partial Q^p}{\partial x}\cdot\left(\frac{\partial \phi_1}{\partial x}-\frac{\partial \phi_1^p}{\partial x}\right) \\
& + k\left(\frac{\partial Q}{\partial x}-\frac{\partial Q^p}{\partial x}\right)\cdot\frac{\partial \phi_1^p}{\partial x} \\
& + kQ^p\cdot\frac{\partial^2 \phi_1^p}{\partial x^2} + kQ^p\cdot\left(\frac{\partial^2 \phi_1}{\partial x^2}-\frac{\partial^2 \phi_1^p}{\partial x^2}\right) \\
& + k(Q-Q^p)\cdot\frac{\partial^2 \phi_1^p}{\partial x^2} \\
& - kQ_{\max}\cdot\frac{\partial^2 \phi_1^p}{\partial x^2} - kQ_{\max}\cdot\left(\frac{\partial^2 \phi_1}{\partial x^2}-\frac{\partial^2 \phi_1^p}{\partial x^2}\right) \\
& + \rho_{\max}\cdot\frac{\partial^2 \phi_1^p}{\partial x^2} + \rho_{\max}\cdot\left(\frac{\partial^2 \phi_1}{\partial x^2}-\frac{\partial^2 \phi_1^p}{\partial x^2}\right)
\end{aligned} \tag{4.54}
$$

$$
\begin{aligned}
a_j = & k\frac{\partial Q^p}{\partial x}\cdot\frac{\partial \phi_1^p}{\partial x} \\
& + k\frac{\partial Q^p}{\partial x}\cdot\frac{\partial \phi_1}{\partial x} - k\frac{\partial Q^p}{\partial x}\cdot\frac{\partial \phi_1^p}{\partial x} \\
& + k\frac{\partial Q}{\partial x}\cdot\frac{\partial \phi_1^p}{\partial x} - k\frac{\partial Q^p}{\partial x}\cdot\frac{\partial \phi_1^p}{\partial x} \\
& + kQ^p\cdot\frac{\partial^2 \phi_1^p}{\partial x^2} \\
& + kQ^p\cdot\frac{\partial^2 \phi_1}{\partial x^2} - kQ^p\cdot\frac{\partial^2 \phi_1^p}{\partial x^2} \\
& + kQ\cdot\frac{\partial^2 \phi_1^p}{\partial x^2} - kQ^p\cdot\frac{\partial^2 \phi_1^p}{\partial x^2} \\
& - kQ_{\max}\cdot\frac{\partial^2 \phi_1^p}{\partial x^2} - kQ_{\max}\cdot\frac{\partial^2 \phi_1}{\partial x^2} + kQ_{\max}\cdot\frac{\partial^2 \phi_1^p}{\partial x^2} \\
& + \rho_{\max}\cdot\frac{\partial^2 \phi_1^p}{\partial x^2} + \rho_{\max}\cdot\frac{\partial^2 \phi_1}{\partial x^2} - \rho_{\max}\cdot\frac{\partial^2 \phi_1^p}{\partial x^2}
\end{aligned} \tag{4.56}
$$

$$
\begin{aligned}
a_j = & k\left[\frac{\partial Q^p}{\partial x}\cdot\frac{\partial \phi_1}{\partial x}+\frac{\partial Q}{\partial x}\cdot\frac{\partial \phi_1^p}{\partial x}-\frac{\partial Q^p}{\partial x}\cdot\frac{\partial \phi_1^p}{\partial x}\right] \\
& + k\left[Q^p\cdot\frac{\partial^2 \phi_1}{\partial x^2}-Q^p\cdot\frac{\partial^2 \phi_1^p}{\partial x^2}+Q\cdot\frac{\partial^2 \phi_1^p}{\partial x^2}\right] \\
& - kQ_{\max}\cdot\frac{\partial^2 \phi_1}{\partial x^2}+\rho_{\max}\cdot\frac{\partial^2 \phi_1}{\partial x^2}
\end{aligned} \tag{4.57}
$$

Since we have already linearized the Butler–Volmer term earlier, the expression below now represents the linearized form of a_j and whole equation.

$$
\begin{aligned}
& a\, i_{0,\mathrm{ref}}\left\{A\left[Q_{\max}C_-^p\chi_a\eta+Q_{\max}C_--Q^pC_-^p\chi_a\eta-Q^pC_--QC_-^p\right]-C\left(Q-Q^p\chi_c\eta\right)\right\} \\
& \quad - k\left(\frac{\partial Q^p}{\partial x}\cdot\frac{\partial \phi_1}{\partial x}+\frac{\partial Q}{\partial x}\cdot\frac{\partial \phi_1^p}{\partial x}\right) \\
& \quad - k\left(Q^p\cdot\frac{\partial^2 \phi_1}{\partial x^2}+Q\cdot\frac{\partial^2 \phi_1^p}{\partial x^2}\right)+kQ_{\max}\cdot\frac{\partial^2 \phi_1}{\partial x^2}-\rho_{\max}\cdot\frac{\partial^2 \phi_1}{\partial x^2} \\
& = -a\, i_{0,\mathrm{ref}}\left\{A\left[-Q_{\max}C_-^p\chi_a\eta^p+Q^pC_-^p\chi_a\eta^p+Q^pC_-^p\right]-C\left(Q^p\chi_c\eta^p\right)\right\} \\
& \quad - k\frac{\partial Q^p}{\partial x}\cdot\frac{\partial \phi_1^p}{\partial x}-kQ^p\cdot\frac{\partial^2 \phi_1^p}{\partial x^2}
\end{aligned} \tag{4.58}
$$

Finally, the equation table for the variable ϕ_1 is given below:

Equation for: ϕ_1	**a**	**b**	**d**
C^+	0	0	0
C^-	0	0	$a\, i_{0,\text{ref}} A(\theta_m - Q^p)$
Q	0	$-k\dfrac{\partial \phi_1^p}{\partial x}$	$-a\, i_{0,\text{ref}} A C^{-p}$ $-k\dfrac{\partial^2 \phi_1^p}{\partial x^2}$ $-a\, i_{0,\text{ref}} C$
ϕ_1	$-kQ^p + kQ_m$ $-\rho_{\max}$	$-k\dfrac{\partial Q^p}{\partial x}\dfrac{1}{2x}$	$a\, i_{0,\text{ref}} A C^{-p} \chi_a(\theta_m - Q^p)$ $+a\, i_{0,\text{ref}} C Q^p \chi_c$
ϕ_2	0	0	$-a\, i_{0,\text{ref}} A C^{-p} \chi_a(\theta_m - Q^p)$ $-a\, i_{0,\text{ref}} C Q^p \chi_c$

Table 4.4: Coefficient matrix terms for variable ϕ_1

And finally, the last variable is ϕ_2. The linearized equation for ϕ_2 and its corresponding table are given below.

Equation for ϕ_2:

$$\sum_i z_i c_i = 0 \tag{4.59}$$

$$z_+ C_+ + z_- C_- = 0 \tag{4.60}$$

$$\Rightarrow \quad z_+ \left(C_+^p + \Delta C_+\right) + z_- \left(C_-^p + \Delta C_-\right) = 0 \tag{4.61}$$

$$z_+ C_+^p + z_+ \Delta C_+ + z_- C_-^p + z_- \Delta C_- = 0 \tag{4.62}$$

Substitute $\Delta C_+ = C_+ - C_+^p$ and $\Delta C_- = C_- - C_-^p$:

$$
\begin{aligned}
& z_+ C_+^p + z_+(C_+ - C_+^p) + z_- C_-^p + z_-(C_- - C_-^p) = 0 \\
\Rightarrow \quad & z_+ C_+^p + z_+ C_+ - z_+ C_+^p + z_- C_-^p + z_- C_- - z_- C_-^p = 0 \\
\Rightarrow \quad & z_+ C_+ + z_- C_- = 0
\end{aligned}
$$

Equation for: ϕ_2	**a**	**b**	**d**
C^+	0	0	z_+
C^-	0	0	z_-
Q_F	0	0	0
ϕ_1	0	0	0
ϕ_2	0	0	0

Table 4.5: Coefficient matrix terms for variable ϕ_2

Electrolyte diffusion layer

Equation for: C^+	**a**	**b**	**d**
C^+	$-D_+$	$-\alpha_+ \dfrac{\partial \phi_2^0}{\partial x}$	$\dfrac{1}{\Delta t} - \alpha_+ z_+^2 \dfrac{\partial^2 \phi_2^0}{\partial x^2}$
C^-	0	0	0
Q_F	0	0	0
ϕ_1	0	0	0
ϕ_2	$-z_+ C_+^0$	$-\alpha_+ \dfrac{\partial C_+^0}{\partial x}$	0

Table 4.6: Coefficient matrix for electrolyte diffusion layer (left block)

$$g = \alpha_+ \left[-\frac{\partial C_+^p}{\partial x} \frac{\partial \phi_2^p}{\partial x} - C_+^p \frac{\partial^2 \phi_2^p}{\partial x^2} \right] + \frac{C_+^p}{\Delta t} \tag{4.63}$$

Equation for: C^-	**a**	**b**	**d**
C^+	0	0	0
C^-	$-D_-$	$-\alpha_- \dfrac{\partial \phi_2^0}{\partial x}$	$\dfrac{1}{\Delta t} - \alpha_- z_-^2 \dfrac{\partial^2 \phi_2^0}{\partial x^2}$
Q_F	0	0	0
ϕ_1	0	0	0
ϕ_2	$-\alpha_- C_-^0$	$-\alpha_- \dfrac{\partial C_-^0}{\partial x}$	0

Table 4.7: Coefficient matrix for electrolyte diffusion layer (right block)

$$g = \alpha_- \left[-\frac{\partial C_-^p}{\partial x} \frac{\partial \phi_2^p}{\partial x} - C_-^p \frac{\partial^2 \phi_2^p}{\partial x^2} \right] + \frac{C_-^p}{\Delta t} \tag{4.64}$$

Equation for: Q_F	**a**	**b**	**d**
C^+	0	0	0
C^-	0	0	0
Q_F	0	0	1
ϕ_1	0	0	0
ϕ_2	0	0	0

Source term: $g = 0$

Table 4.8: Coefficient matrix for variable Q_F

Equation for: ϕ_1	**a**	**b**	**d**
C^+	0	0	0
C^-	0	0	0
Q_F	0	0	0
ϕ_1	0	0	1
ϕ_2	0	0	0

Source term: $g = 0$

Table 4.9: Coefficient matrix for variable ϕ_1

Equation for: ϕ_2	**a**	**b**	**d**
C^+	0	0	z_+
C^-	0	0	z_-
Q_F	0	0	0
ϕ_1	0	0	0
ϕ_2	0	0	0

Source term: $g = 0$

Table 4.10: Coefficient matrix for variable ϕ_2

Boundary at current collector/polymer electrode

Equation for C^+	**p**	**e**
C^+	$-D_+ p$	$-\alpha_+ p \left(\frac{\partial \phi_2^p}{\partial x}\right)$
C^-	0	$\sigma_+ A(\theta_{F,m} - q_F^p)$
Q_F	0	$-\sigma_+ A C_-^p - \delta_+ C$
ϕ_1	0	$\sigma_+ A C_-^p \chi_a(\theta_{F,m} - q_F^p) + \delta_+ C q_F^p \chi_c$
ϕ_2	$-\alpha_+ p C_+^p$	$-\sigma_+ A C_-^p \chi_o(\theta_{F,m} - q_F^p) - \delta_+ C q_F^p \chi_c$

Table 4.11: Boundary conditions at the current collector/polymer electrode interface

$$\begin{aligned} f = & -\sigma_+ A \left[C_-^p q_F^p - C_-^p q_{F,m} \chi_o(\phi_1^p - \phi_2^p) + C_-^p q_F^p \chi_a(\phi_1^p - \phi_2^p)\right] \\ & + \delta_+ C q_F^p \chi_c(\phi_1^p - \phi_2^p) - \alpha_+ p\, C_+^p \frac{\partial \phi_2^p}{\partial x} \end{aligned} \tag{4.65}$$

Equation for C^-	**p**	**e**
C^+	0	0
C^-	$-D_- p$	$\sigma_- A(\theta_{F,m} - q_F^p) - \alpha_- p \left(\dfrac{\partial \phi_2^p}{\partial x}\right)$
Q_F	0	$-\sigma_- A C_-^p - \delta_- C$
ϕ_1	0	$\sigma_- A C_-^p \chi_a(\theta_{F,m} - q_F^p) + \delta_- C q_F^p \chi_c$
ϕ_2	$-\alpha_- p C_+^p$	$-\sigma_- A C_-^p \chi_o(\theta_{F,m} - q_F^p) - \delta_- C q_F^p \chi_c$

Table 4.12: Boundary condition terms at current collector/polymer interface (C^- side)

$$
\begin{aligned}
f = \; & -\sigma_- A \left[C_-^p q_F^p - C_-^p q_{F,m} \chi_o(\phi_1^p - \phi_2^p) - C_-^p q_F^p \chi_a(\phi_1^p - \phi_2^p)\right] \\
& + \delta_- C q_F^p \chi_c(\phi_1^p - \phi_2^p) - \alpha_- p \, C_+^p \frac{\partial \phi_2^p}{\partial x}
\end{aligned}
\tag{4.66}
$$

Equation for Q_F	**p**	**e**
C^+	0	0
C^-	0	$-2\delta_{\sigma,\mathrm{ref}} A(\theta_{F,m} - q_F^p)$
Q_F	0	$\dfrac{1}{\Delta t} + 2\delta_{\sigma,\mathrm{ref}} A C_-^p + 2\delta_{\sigma,\mathrm{ref}} C$
ϕ_1	0	$-2\delta_{\sigma,\mathrm{ref}} A C_-^p \chi_a(\theta_{F,m} - q_F^p) - 2\delta_{\sigma,\mathrm{ref}} C \chi_c$
ϕ_2	0	$+2\delta_{\sigma,\mathrm{ref}} A C_-^p \chi_o(\theta_{F,m} - q_F^p) + 2\delta_{\sigma,\mathrm{ref}} C \chi_c$

Table 4.13: Coefficient matrix for Q_F at electrolyte/polymer interface

$$f = 2\delta_{\sigma,\mathrm{ref}} A \left[C_-^p q_F^p - q_{F,m}^p \chi_o (\phi_1^p - \phi_2^p) + C_-^p q_F^p \chi_a (\phi_1^p - \phi_2^p) \right] - 2\delta_{\sigma,\mathrm{ref}} C q_F^p \chi_c (\phi_1^p - \phi_2^p) + \frac{q_F^p}{\Delta t} \tag{4.67}$$

Equation for ϕ_1	**p**	**e**
C^+	0	0
C^-	0	0
Q_F	0	0
ϕ_1	0	1
ϕ_2	0	0

Source term:

$$f = E_{\mathrm{ap}} + \phi_{\mathrm{ref}}$$

Table 4.14: Boundary condition for ϕ_1

Equation for ϕ_2	**p**	**e**
C^+	$-Fz_+D_+p$	0
C^-	$-Fz_-D_-p$	0
Q_F	0	0
ϕ_1	0	0
ϕ_2	$-k_{\mathrm{sef}}$	0

Source term:

$$f = 0$$

Table 4.15: Boundary condition for ϕ_2

Interface at polymer electrode/diffusion layer

Equation for C_+	**a**	**b**	**d**
C^+	0	$-D_+p + D_+$	$-\alpha_+ p\frac{\partial \phi_2^p}{\partial x} + \alpha\frac{\partial \phi_2^p}{\partial x}$
C^-	0	0	0
Q_F	0	0	0
ϕ_1	0	0	0
ϕ_2	0	$q_+ pC_+^p + \alpha C_+^p$	0

$$g = -\alpha_+ pC_+^p\frac{\partial \phi_2^p}{\partial x} + \alpha C_+^p\frac{\partial \phi_2^p}{\partial x}$$

Table 4.16: Interfacial condition at polymer/diffusion layer for C_+

Equation for C_-	**a**	**b**	**d**
C^+	0	0	0
C^-	0	$-D_-p + D_-$	$-\alpha_- p\frac{\partial \phi_2^p}{\partial x} + \alpha\frac{\partial \phi_2^p}{\partial x}$
Q_F	0	0	0
ϕ_1	0	0	0
ϕ_2	0	$-\alpha_- pC_-^p + \alpha C_-^p$	0

Source term:

$$g = -\alpha_- pC_-^p\frac{\partial \phi_2^p}{\partial x} + \alpha C_-^p\frac{\partial \phi_2^p}{\partial x}$$

Table 4.17: Interfacial condition at polymer/diffusion layer for C_-

Equation for Q_F	**a**	**b**	**d**
C^+	0	0	0
C^-	0	0	0
Q_F	0	1	0
ϕ_1	0	0	0
ϕ_2	0	0	0

Source term: $g = 0$

Table 4.18: Coefficient matrix for Q_F

Equation for ϕ_1	**a**	**b**	**d**
C^+	0	0	0
C^-	0	0	0
Q_F	0	0	0
ϕ_1	0	1	0
ϕ_2	0	0	0

Source term: $g = 0$

Table 4.19: Coefficient matrix for ϕ_1

Equation for ϕ_2	**a**	**b**	**d**
C^+	0	$-Fz_+D_+p + Fz_+D_+$	0
C^-	0	$-Fz\_D\_p + Fz\_D\_$	0
Q_F	0	0	0
ϕ_1	0	0	0
ϕ_2	0	$-k_{\text{sef}} + k_s$	0

Source term: $g = 0$

Table 4.20: Coefficient matrix for ϕ_2

Boundary at bulk solution

Equation for C^+	**p**	**e**
C^+	0	1
C^-	0	0
Q_F	0	0
ϕ_1	0	0
ϕ_2	0	0

Boundary condition: $C^+ = C_{\text{ref}}$

Source term:

$$f = C_{\text{ref}}$$

Table 4.21: Boundary condition at bulk solution for C^+

Equation for C^-	**p**	**e**
C^+	0	0
C^-	0	1
Q_F	0	0
ϕ_1	0	0
ϕ_2	0	0

Table 4.22: Boundary condition at bulk solution

Equation for Q_F	**p**	**e**
C^+	0	0
C^-	0	0
Q_F	0	1
ϕ_1	0	0
ϕ_2	0	0

Boundary condition: $Q_F = 0$

Table 4.23: Boundary matrix for $Q_F = 0$

Equation for ϕ_1	**p**	**e**
C^+	0	0
C^-	0	0
Q_F	0	0
ϕ_1	0	1
ϕ_2	0	0

Boundary condition: $\phi_1 = 0$

Table 4.24: Boundary matrix for $\phi_1 = 0$

Equation for ϕ_2	**p**	**e**
C^+	0	0
C^-	0	0
Q_F	0	0
ϕ_1	0	0
ϕ_2	0	1

Boundary condition: $\phi_2 = \phi_{\text{ref}}$

Table 4.25: Boundary matrix for $\phi_2 = \phi_{\text{ref}}$

4.2 Constructions of Coefficient Matrices

Equation	C^+	C^-	Q	ϕ_1	ϕ_2
Eq1	$-D_+p$	0	0	0	$-\alpha_+p\,C^+$
Eq2	0	$-D_-p$	0	0	$-\alpha_-p\,C^-$
Eq3	0	0	0	0	0
Eq4	0	0	0	$-KQ^p + KQ_{\max} - \rho_{\max}$	0
Eq5	0	0	0	0	0

Table 4.26: sma matrix before interphase region

Equation	C^+	C^-	Q	ϕ_1	ϕ_2
Eq1	$-\alpha_+p\frac{\partial\phi_2^p}{\partial x}$	0	0	0	$-\alpha_+p\frac{\partial C_+^p}{\partial x}$
Eq2	0	$-\alpha_-p\frac{\partial\phi_2^p}{\partial x}$	0	0	$-\alpha_-p\frac{\partial C_-^p}{\partial x}$
Eq3	0	0	0	0	0
Eq4	0	0	$-k\frac{\partial\phi_1^p}{\partial x}$	$-k\frac{\partial Q^p}{\partial x}$	0
Eq5	0	0	0	0	0

Table 4.27: smb before interphase region

4.3 Modelling Results and Future Work

The coefficient matrices of the linearized equations have been constructed, and ongoing efforts are focused on debugging errors in the code. Particular attention is being paid to addressing the divergence problem encountered during simulations. Future work will involve refining the numerical implementation to improve

stability, as well as exploring alternative solution strategies to ensure convergence and robustness of the model.

Chapter 5

CONCLUSIONS AND FUTURE WORK

The work presented in this thesis set out to address one of the long-standing questions in the field of conducting polymers: the interplay between electron transfer and ion motion, and the extent to which these processes are separable. Conventional electrochemical analysis using cyclic voltammetry has proven insufficient in probing redox processes in conducting polymers. While cyclic voltammetry remains one of the most widely adopted tools in electrochemistry, it inherently convolutes Faradaic and capacitive currents, thereby making it difficult to distinguish their respective contributions. This limitation was clearly demonstrated in this study, where even after normalization procedures the voltammetric currents reflected a complex mixture of diffusion-limited and diffusionless response.

Cyclic Voltammetry and Normalization

When the current was normalized by either the sweep rate or its square root, convergence was observed in well-defined potential regions, identifying domains dominated by diffusion or surface-confined redox effects. These results confirmed

that capacitive contributions cannot be ignored, particularly at higher potentials, and that current normalization alone is insufficient for fully understanding the redox dynamics of conducting polymers. Although normalization approaches can provide insight, they do not deconvolute the simultaneous contributions of redox and charging currents. This finding motivated the use of additional, complementary spectroscopic techniques to isolate and understand electron-transfer phenomena.

Spectroelectrochemistry and the Basis of PCA Analysis

By complementing cyclic voltammetry with simultaneous UV–Vis spectroscopic monitoring, a new dimension was added to the understanding of conducting polymer redox processes. At very slow sweep rates (2 mV/s), the full range of redox states could be probed. The spectroscopic dataset obtained under these quasi-equilibrium conditions, spanning wavelengths between 350 nm and 1100 nm, was unique for each polymer film. In this thesis, such datasets were collectively referred to as the *basis set*.

When the spectroscopic measurements taken before cycling (conditioning), during cycling, and after cycling were jointly analyzed with principal component analysis (PCA), it was observed that an approximately 100-dimensional dataset (reflecting the absorbance at each wavelength) could be reduced to just two principal components without significant loss of information. The first principal component consistently explained around 95% of the total variance in the dataset, while the second accounted for nearly all of the remaining variance.

The fact that two components were sufficient to reconstruct the entire dataset aligns with the presence of isosbestic points, which were observed both in this study and in previous reports. An isosbestic point, where spectra intersect at

a fixed wavelength, indicates two-state interconversion between oxidized and reduced species. Thus, the mathematical result of PCA that only two spectral components are required was consistent with the physical evidence of isosbestic behavior.

Fitting of Spectra Using Two Components

The two components identified through PCA were then employed to fit the spectroscopic data collected under two experimental conditions: (1) at constant applied potential (conditioning), and (2) during cyclic voltammetry at various sweep rates. The rationale for this approach is straightforward: during conditioning, where the polymer is held at a fixed potential, the absorbance remains constant and therefore the spectral coefficients are expected to remain unchanged as well. Conversely, during cycling, where the potential continuously sweeps between reduction and oxidation limits, the polymer repeatedly switches between states, and the average spectroscopic response provides information about the relative contributions of oxidized and reduced components at various sweep rates from slow to fast.

This fitting procedure allowed the quantitative tracking of how much the polymer resided in oxidized versus reduced states during cyclic voltammetry at different sweep rates. Importantly, at high sweep rates—up to 200,000 V/s—the measured response represents the average of thousands of cycles collected within a 30-second experimental window. This averaging captures the overall balance of states and enables quantitative comparison across sweep rates.

Interpretation of Coefficients

The two fitted coefficients derived from the PCA analysis were evaluated in two complementary ways. First, the conditioning coefficients were examined. These

coefficients remained essentially constant across repeated experiments at the same applied potential, confirming that the method is stable and that the polymer maintains its optical response so long as no degradation occurs.

Second, the cycling coefficients were evaluated as a function of sweep rate. A systematic trend was observed: the coefficient associated with the more oxidized state tended to decrease with increasing sweep rate, whereas the coefficient corresponding to the more reduced state showed a complementary increase. This behavior is consistent with the expectation that, under fast potential sweeps, ion diffusion into the polymer may become limited. Since full ion insertion cannot keep up with the electron transfer at high rates, the polymer appears to spend relatively less time in the oxidized state and more time in the reduced state. Importantly, the coefficient assigned to the oxidized state did not fall to zero, suggesting that oxidation can still occur even when ion diffusion is partially hindered. This observation indicates that electron transfer may proceed independently of complete ion motion.

Optical Charge as a Descriptor

Beyond evaluating the raw coefficients, a new descriptor termed "optical charge" was defined. This quantity was calculated as the difference between the cycling and conditioning coefficients at a given sweep rate, i.e.

$$Q_{\mathrm{Opt}} = C_{\mathrm{cycle}} - C_{\mathrm{cond}}$$

Here, Q_{opt} represents the effective average change in optical absorbance during cycling relative to the reference state, and can be interpreted as the net optical modulation induced by redox switching of the polymer.

The optical charge values were observed to approach a steady-state level that became largely independent of further increases in scan rate. This apparent saturation suggests that, once ionic motion imposes a rate limitation, additional increases in sweep rate do not significantly alter the overall optical response.

Importantly, the residual net response remains non-zero, indicating that electron transfer can still proceed even when ionic motion is partially hindered. While this trend initially appears consistent with a steady-state regime, closer inspection of the coefficient values reveals more complex behavior that warrants further investigation. In particular, although conditioning is typically performed at the open-circuit potential (OCP), it is essential to assess how the initial state of the film influences the measured optical charge. Starting from a dedoped state by applying negative potentials, versus beginning from a doped state with positive potentials, may yield different optical charge evolutions.

Future Work

In this study, PEDOT films were synthesized via chronopotentiometry for different deposition durations, resulting in films with varying thicknesses. An attempt was made to investigate the dependence of sweep rate response on film thickness. However, this analysis proved challenging due to several factors. In future work, this relationship should be systematically examined using more uniform coatings, ideally prepared as continuous layers of well-defined and controlled thicknesses. Such samples would allow a more rigorous assessment of the interplay between sweep rate and film thickness.

In addition, systematic studies on the effect of film thickness prepared by various coating methods, as well as the role of different counter-ions, will be carried out. Extending the approach to other polymers and electrochromic materials will further broaden the applicability of the methodology.

As a secondary aspect of this work, efforts were initiated to develop a physics-based model capable of separating capacitive and faradaic current contributions. The long-term aim of this modeling approach is to reproduce the cyclic voltammetry response under the specific experimental conditions studied here, and to provide a framework that can be directly fitted to the cyclic voltammetry data. Preliminary steps indicated the feasibility of this approach, and future work will

focus on refining the model to achieve convergence and reliable reproduction of the experimental cyclic voltammetry signals.

Bibliography

[1] C. E. D. Chidsey. "Free Energy and Temperature Dependence of Electron Transfer at the Metal–Electrolyte Interface". In: *Science* 251.4996 (1991), pp. 919–922. DOI: 10.1126/science.251.4996.919.

[2] A. Ulman. *An Introduction to Ultrathin Organic Films: From Langmuir–Blodgett to Self–Assembly*. See Part II: Langmuir–Blodgett films, p. 101. Academic Press, 1991.

[3] Irving Langmuir. "The Constitution and Fundamental Properties of Solids and Liquids. II. Liquids". In: *Journal of the American Chemical Society* 39.9 (1917), pp. 1848–1906. DOI: 10.1021/ja02254a006.

[4] Jacob Sagiv. "Organized monolayers by adsorption. 1. Formation and structure of oleophobic mixed monolayers on solid surfaces". In: *Journal of the American Chemical Society* 102.1 (1980), pp. 92–98. DOI: 10.1021/ja00521a016.

[5] Stephen R. Wasserman, Yu Tai Tao, and George M. Whitesides. "Structure and reactivity of alkylsiloxane monolayers formed by reaction of alkyltrichlorosilanes on silicon substrates". In: *Langmuir* 5.4 (1989), pp. 1074–1087. DOI: 10.1021/la00088a035.

[6] Allen J. Bard and Larry R. Faulkner. *Electrochemical Methods: Fundamentals and Applications*. 2nd ed. Chapter 17.2, p. 757. Wiley, 2001.

[7] Henry Taube, Howard Myers, and Ronald L. Rich. "Observations on the Mechanism of Electron Transfer in Solution". In: *Journal of the American Chemical Society* 75.16 (1953), pp. 4118–4119. DOI: 10.1021/ja01112a546.

[8] Rudolph A. Marcus. "Electron Transfer Reactions in Chemistry: Theory and Experiment". In: *Nobel Lecture*. Nobel Lecture, December 8, 1992. Noyes Laboratory of Chemical Physics, California Institute of Technology. The Nobel Foundation. Stockholm, 1992.

[9] Donald G. Truhlar, Bruce C. Garrett, and Stephen J. Klippenstein. "Current Status of Transition-State Theory". In: *The Journal of Physical Chemistry* 100.31 (1996), pp. 12771–12800. DOI: 10.1021/jp953748q.

[10] J. R. Miller, L. T. Calcaterra, and G. L. Closs. "Intramolecular long-distance electron transfer in radical anions: The effects of free energy and solvent on the reaction rates". In: *Journal of the American Chemical Society* 106.10 (1984), pp. 3047–3049. DOI: 10.1021/ja00322a058.

[11] David J. Griffiths and Darrell F. Schroeter. *Introduction to Quantum Mechanics*. 3rd ed. Cambridge: Cambridge University Press, 2018. ISBN: 9781107189638.

[12] John F. Smalley et al. "Interfacial Electron-Transfer Kinetics of Ferrocene through Oligophenyleneethynylene Bridges Attached to Gold Electrodes as Constituents of Self-Assembled Monolayers: Observation of a Nonmonotonic Distance Dependence". In: *Journal of the American Chemical Society* 126.44 (2004), pp. 14620–14630. DOI: 10.1021/ja047458b.

[13] E. Laviron. "General expression of the linear potential sweep voltammogram in the case of diffusionless electrochemical systems". In: *Journal of Electroanalytical Chemistry and Interfacial Electrochemistry* 101.1 (1979), pp. 19–28. DOI: 10.1016/S0022-0728(79)80075-3.

[14] E. Laviron. "A multilayer model for the study of space distributed redox modified electrodes: Part I. Description and discussion of the model". In: *Journal of Electroanalytical Chemistry and Interfacial Electrochemistry* 112.1 (1980), pp. 1–9. DOI: 10.1016/S0022-0728(80)80002-7.

[15] Matěj Velický et al. "Electron Transfer Kinetics on Mono- and Multilayer Graphene". In: *ACS Nano* 8.10 (2014), pp. 10089–10100. DOI: 10.1021/nn504298r.

[16] Hun-Gi Hong and Thomas E. Mallouk. “Electrochemical Measurements of Electron Transfer Rates through Zirconium 1,2-Ethanediylbis(phosphonate) Multilayer Films on Gold Electrodes”. In: *Langmuir* 7.10 (1991), pp. 2362–2369. DOI: 10.1021/la00057a010.

[17] Ke Ji et al. “Lithium intercalation into bilayer graphene”. In: *Nature Communications* 10.1 (2019), p. 275. DOI: 10.1038/s41467-018-07942-z. URL: https://doi.org/10.1038/s41467-018-07942-z.

[18] K. Mizushima et al. “LixCoO2 (0 ¡ x ¡ 1): A new cathode material for batteries of high energy density”. In: *Materials Research Bulletin* 15.6 (1980), pp. 783–789. DOI: 10.1016/0025-5408(80)90012-4.

[19] Martin Winter et al. “Insertion Electrode Materials for Rechargeable Lithium Batteries”. In: *Advanced Materials* 10.10 (1998), pp. 725–763. DOI: 10.1002/(SICI)1521-4095(199807)10:10<725::AID-ADMA725>3.0.CO;2-Z.

[20] A. K. Padhi, K. S. Nanjundaswamy, and J. B. Goodenough. “Phospho-olivines as Positive-Electrode Materials for Rechargeable Lithium Batteries”. In: *Journal of The Electrochemical Society* 144.4 (1997), pp. 1188–1194. DOI: 10.1149/1.1837571.

[21] Babak Anasori, Maria R. Lukatskaya, and Yury Gogotsi. “2D Metal Carbides and Nitrides (MXenes) for Energy Storage”. In: *Nature Reviews Materials* 2 (2017), p. 16098. DOI: 10.1038/natrevmats.2016.98.

[22] Dandan Zhang et al. “In situ monitoring redox processes in energy storage using UV–Vis spectroscopy”. In: *Nature Energy* 8 (2023), pp. 567–576. DOI: 10.1038/s41560-023-01240-9.

[23] B. E. Conway. *Electrochemical Supercapacitors: Scientific Fundamentals and Technological Applications*. New York: Springer Science+Business Media, LLC, 1999. ISBN: 978-1-4757-3060-9. DOI: 10.1007/978-1-4757-3058-6.

[24] Elzbieta Frackowiak and François Béguin. “Carbon materials for the electrochemical storage of energy in capacitors”. In: *Carbon* 39.6 (2001), pp. 937–950. DOI: 10.1016/S0008-6223(00)00183-4.

[25] Ryong Ryoo, Sang Hoon Joo, and Shinae Jun. "Synthesis of Highly Ordered Carbon Molecular Sieves via Template-Mediated Structural Transformation". In: *The Journal of Physical Chemistry B* 103.37 (1999), pp. 7743–7746. DOI: 10.1021/jp991673a.

[26] Cyrille Costentin and Jean-Michel Savéant. "Energy storage: pseudocapacitance in prospect". In: *Chemical Science* 10 (2019). Open Access Article, licensed under CC BY-NC 3.0, pp. 5656–5666. DOI: 10.1039/C9SC01662G.

[27] Alexander C. Forse et al. "New Perspectives on the Charging Mechanisms of Supercapacitors". In: *Journal of the American Chemical Society* 138.18 (2016), pp. 5731–5744. DOI: 10.1021/jacs.6b02115.

[28] B. E. Conway, V. Birss, and J. Wojtowicz. "The role and utilization of pseudocapacitance for energy storage by supercapacitors". In: *Journal of Power Sources* 66.1 (1997), pp. 1–14. DOI: 10.1016/S0378-7753(96)02329-3.

[29] Douglas A. Skoog, Donald M. West, and F. James Holler. *Fundamentals of Analytical Chemistry*. 9th ed. Boston, MA: Saunders College Publishing, 2014.

[30] Veronica Augustyn, Patrice Simon, and Bruce Dunn. "Pseudocapacitive Oxide Materials for High-Rate Electrochemical Energy Storage". In: *Energy & Environmental Science* 7 (2014). Review Article; First published: March 13, 2014, pp. 1597–1614. DOI: 10.1039/C3EE44164D.

[31] Yury Gogotsi and Richard M. Penner. "Energy Storage in Nanomaterials: Capacitive, Pseudocapacitive, or Battery-Like?" In: *ACS Nano* 12.3 (2018), pp. 2081–2083. DOI: 10.1021/acsnano.8b01670.

[32] Cyrille Costentin, Thomas R. Porter, and Jean-Michel Savéant. "How Do Pseudocapacitors Store Energy? Theoretical Analysis and Experimental Illustration". In: *ACS Applied Materials & Interfaces* 9 (2017), pp. 8649–8658. DOI: 10.1021/acsami.6b14100.

[33] Jochen E. Kuhlmann et al. "Electrochemical Characterization of Redox Probes Confined in 3D Conducting Polymer Networks". In: *Chemistry*

– *A European Journal* 28.5 (2021), e202103257. DOI: 10.1002/chem.202103257. URL: https://doi.org/10.1002/chem.202103257.

[34] Wessel van den Bergh et al. "Faster Intercalation Pseudocapacitance Enabled by Adjustable Amorphous Titania Where Tunable Isomorphic Architectures Reveal Accelerated Lithium Diffusivity". In: *Batteries & Supercaps* 5.7 (2022), e202200122. DOI: 10.1002/batt.202200122. URL: https://doi.org/10.1002/batt.202200122.

[35] Sarojini Jeeva Panchu, Kumar Raju, and Hendrik C. Swart. "Emerging Two–Dimensional Intercalation Pseudocapacitive Electrodes for Supercapacitors". In: *ChemElectroChem* 11.8 (2024), e202300810. DOI: 10.1002/celc.202300810.

[36] Richard S. Nicholson and Irving Shain. "Theory of Stationary Electrode Polarography: Single Scan and Cyclic Methods Applied to Reversible, Irreversible, and Kinetic Systems". In: *Analytical Chemistry* 36.4 (1964), pp. 706–723. DOI: 10.1021/ac60210a007.

[37] Matthew Chagnot et al. "Influence of Finite Diffusion on Cation Insertion-Coupled Electron Transfer Kinetics in Thin Film Electrodes". In: *Journal of The Electrochemical Society* 171.1 (2024), p. 010527. DOI: 10.1149/1945-7111/ad1d98.

[38] Matthew Chagnot et al. "Influence of Finite Diffusion on Cation Insertion-Coupled Electron Transfer Kinetics in Thin Film Electrodes". In: *Journal of The Electrochemical Society* 171.1 (2024), p. 010527. DOI: 10.1149/1945-7111/ad1d98.

[39] T.-C. Liu, W.G. Pell, and B.E. Conway. "Behavior of Molybdenum Nitrides as Materials for Electrochemical Capacitors: Comparison with Ruthenium Oxide". In: *Journal of The Electrochemical Society* 145.6 (1998), pp. 1882–1888. DOI: 10.1149/1.1838561.

[40] Wessel van den Bergh et al. "Amorphization of Pseudocapacitive T-Nb_2O_5 Accelerates Lithium Diffusivity as Revealed Using Tunable Isomorphic Architectures". In: *Batteries & Supercaps* 5.6 (2022), e202200208. DOI: 10.1002/batt.202200208.

[41] Yonghui Wu et al. “Defect-Rich MoO_3 Nanobelts for Ultrafast and Wide-Temperature Proton Battery”. In: *Energy Storage Materials* 61 (2023), p. 102849. ISSN: 2405-8297. DOI: 10.1016/j.ensm.2023.102849. URL: https://doi.org/10.1016/j.ensm.2023.102849.

[42] Hye Sung Park et al. “Redox-active charge carriers of conducting polymers as a tuner of conductivity and its potential window”. In: *Scientific Reports* 3 (2013), p. 2454. DOI: 10.1038/srep02454. URL: https://doi.org/10.1038/srep02454.

[43] John Newman. “Resistance for Flow of Current to a Disk”. In: *Journal of The Electrochemical Society* 113.5 (1966), pp. 501–502. DOI: 10.1149/1.2424099. URL: https://doi.org/10.1149/1.2424099.

[44] Stephen W. Feldberg. “Surprising Effect of Uncompensated Resistance on the Cyclic Voltammetric Responses for a Reversible Surface-Confined and Uniformly Accessible Redox Couple”. In: *Analytical Chemistry* 83.15 (2011), pp. 5851–5856. DOI: 10.1021/ac200382v. URL: https://doi.org/10.1021/ac200382v.

[45] Veronica Augustyn et al. “High-rate electrochemical energy storage through Li^+ intercalation pseudocapacitance”. In: *Nature Materials* 12.6 (2013), pp. 518–522. DOI: 10.1038/nmat3601.

[46] C. Kvarnström et al. “Vibrational signatures of electrochemical p- and n-doping of poly(3,4-ethylenedioxythiophene) films: an in situ attenuated total reflection Fourier transform infrared (ATR-FTIR) study”. In: *Journal of Molecular Structure* 521.1–3 (2000). In honour of Professor Giuseppe Zerbi on the occasion of his 65th birthday, pp. 271–277. ISSN: 0022-2860. DOI: 10.1016/S0022-2860(99)00442-1. URL: https://doi.org/10.1016/S0022-2860(99)00442-1.

[47] Stephen W. Feldberg. “Reinterpretation of polypyrrole electrochemistry. Consideration of capacitive currents in redox switching of conducting polymers”. In: *Journal of the American Chemical Society* 106.17 (1984), pp. 4671–4674. DOI: 10.1021/ja00329a004. URL: https://doi.org/10.1021/ja00329a004.

[48] A. F. Diaz et al. “Electrochemistry of conducting polypyrrole films”. In: *Journal of Electroanalytical Chemistry and Interfacial Electrochemistry* 129.1–2 (1981), pp. 115–132. DOI: 10.1016/S0022-0728(81)80008-3. URL: https://doi.org/10.1016/S0022-0728(81)80008-3.

[49] Claude P. Andrieux et al. “Identification of the First Steps of the Electrochemical Polymerization of Pyrroles by Means of Fast Potential Step Techniques”. In: *The Journal of Physical Chemistry* 95 (1991), pp. 10158–10164. DOI: 10.1021/j100176a063. URL: https://doi.org/10.1021/j100176a063.

[50] Virginia Ruiz et al. “Bidimensional Spectroelectrochemistry Applied to the Electrosynthesis and Characterization of Conducting Polymers: Study of Poly[4,4′-bis(butylthio)-2,2′-bithiophene]”. In: *Helvetica Chimica Acta* 84.12 (2001), pp. 3628–3644. DOI: 10.1002/1522-2675(20011219)84:12<3628::AID-HLCA3628>3.0.CO;2-0. URL: https://doi.org/10.1002/1522-2675(20011219)84:12%3C3628::AID-HLCA3628%3E3.0.CO;2-0.

[51] Gursel Sonmez. “Polymeric electrochromics”. In: *Chemical Communications* (2005), pp. 5251–5259. DOI: 10.1039/B510230H.

[52] Chang Gu et al. “Emerging Electrochromic Materials and Devices for Future Displays”. In: *Chemical Reviews* 122.18 (2022), pp. 14679–14721. DOI: 10.1021/acs.chemrev.1c01055.

[53] Namsheer Ka and Chandra Sekhar Rout. “Conducting polymers: a comprehensive review on recent advances in synthesis, properties and applications”. In: *RSC Advances* 11.9 (2021), pp. 5659–5697. DOI: 10.1039/D0RA07800J.

[54] J. L. Brédas and G. B. Street. “Polarons, Bipolarons, and Solitons in Conducting Polymers”. In: *Accounts of Chemical Research* 18.10 (1985), pp. 309–315. DOI: 10.1021/ar00118a004.

[55] Michael E. G. Lyons, ed. *Electroactive Polymer Electrochemistry: Part 1: Fundamentals*. Springer, 2013. ISBN: 978-1475750713.

[56] P. N. Bartlett and J. W. Gardner. "Diffusion and binding of molecules to sites within homogeneous thin films". In: *Philosophical Transactions: Mathematical, Physical and Engineering Sciences* 354.1704 (1996), pp. 35–57. URL: http://www.jstor.org/stable/54539.

[57] Igor Zozoulenko et al. "Polarons, Bipolarons, And Absorption Spectroscopy of PEDOT". In: *ACS Applied Polymer Materials* 1.1 (2019), pp. 83–94. DOI: 10.1021/acsapm.8b00061. URL: https://doi.org/10.1021/acsapm.8b00061.

[58] Zhiting Chen and Erin L. Ratcliff. "Watching Polarons Move in the Energy and Frequency Domains Using Color Impedance Spectroscopy". In: *Chemistry of Materials* 34.23 (2022), pp. 10691–10700. DOI: 10.1021/acs.chemmater.2c02831. URL: https://doi.org/10.1021/acs.chemmater.2c02831.

[59] Alexander Kraft. "Too blue to be good? A critical overview on the electrochromic properties and applications of Prussian blue". In: *Solar Energy Materials and Solar Cells* 278 (2024), p. 113195. ISSN: 0927-0248. DOI: 10.1016/j.solmat.2024.113195. URL: https://www.sciencedirect.com/science/article/pii/S0927024824005075.

[60] Paul Monk, Roger Mortimer, and David Rosseinsky. *Electrochromism and Electrochromic Devices*. Online publication date: August 2009. Cambridge University Press, 2007. ISBN: 9780511550959. DOI: 10.1017/CBO9780511550959.

[61] Jin You Zheng et al. "Review on Recent Progress in WO_3-Based Electrochromic Films: Preparation Methods and Performance Enhancement Strategies". In: *Nanoscale* 15 (2023). Review Article, first published: 09 Nov 2022, pp. 63–79. DOI: 10.1039/D2NR04613H.

[62] Michael Dietrich et al. "Electrochemical and Spectroscopic Characterization of Polyalkylenedioxythiophenes". In: *Journal of Electroanalytical Chemistry* 369.1–2 (1994), pp. 87–92. ISSN: 1572-6657. DOI: 10.1016/0022-0728(94)87085-3. URL: https://www.sciencedirect.com/science/article/pii/0022072894870853.

[63] Wilford Nels Hansen, Theodore Kuwana, and Robert A. Osteryoung. "Observation of Electrode-Solution Interface by Means of Internal Reflection Spectrometry". In: *Analytical Chemistry* 38.13 (1966), pp. 1810–1821. DOI: 10.1021/ac50155a035.

[64] I. Shiyanovskaya. "Isotopic Effect in Evolution of Structure and Optical Gap During Electrochromic Coloration of $WO_3 \cdot 1/3(H_2O)$ Films". In: *Progress in Fourier Transform Spectroscopy*. Ed. by J. Mink, G. Keresztury, and R. Kellner. Vol. 14. Mikrochimica Acta Supplement. Springer, Vienna, 1997. ISBN: 978-3-211-82931-8. DOI: 10.1007/978-3-7091-6840-0_218.

[65] B. W. Faughnan and R. S. Crandall. "Electrochromic Displays Based on WO_3". In: *Display Devices*. Ed. by J. I. Pankove. Vol. 40. Topics in Applied Physics. Published online: 02 July 2005. Springer, Berlin, Heidelberg, 1980. ISBN: 978-3-540-09868-3. DOI: 10.1007/3540098682_12.

[66] Stephan Kirchmeyer and Knud Reuter. "Scientific Importance, Properties and Growing Applications of Poly(3,4-ethylenedioxythiophene)". In: *Journal of Materials Chemistry* 15 (2005). First published: 14 Feb 2005, pp. 2077–2088. DOI: 10.1039/B417803N.

[67] M. Mastragostino et al. "Polymer-Based Electrochromic Devices—I. Poly(3-methylthiophenes)". In: *Electrochimica Acta* 38.1 (1993), pp. 135–140. ISSN: 0013-4686. DOI: 10.1016/0013-4686(93)80020-Z. URL: https://www.sciencedirect.com/science/article/pii/001346869380020Z.

[68] A. Galal et al. "Electrochemical Synthesis, Characterization and Spectroelectrochemical Studies of Some Conducting Poly(heterolene) Films". In: *Proceedings of the Electrochemical Society*. Vol. 90-2. 1990, pp. 179–191.

[69] Jiankang Guo et al. "Fast-Switching WO_3-Based Electrochromic Devices: Design, Fabrication, and Applications". In: *Accounts of Materials Research* 4.5 (2023), pp. 438–447. DOI: 10.1021/accountsmr.2c00217.

[70] Mariam Barawi et al. "A dual band electrochromic device switchable across four distinct optical modes". In: *Journal of Materials Chemistry A* 6 (2018), pp. 10201–10205. DOI: 10.1039/C8TA02636J. URL: https://doi.org/10.1039/C8TA02636J.

[71] Benjamin Z. Zydlewski and Delia J. Milliron. "Dual-Band Electrochromic Devices Utilizing Niobium Oxide Nanocrystals". In: *ACS Applied Materials & Interfaces* 16.19 (2024), pp. 24920–24928. DOI: 10.1021/acsami.4c02997. URL: https://doi.org/10.1021/acsami.4c02997.

[72] Jenelle Fortunato et al. "Dual-Band Electrochromism in Hydrous Tungsten Oxide". In: *ACS Photonics* 10.9 (2023), pp. 3409–3418. DOI: 10.1021/acsphotonics.3c00921.

[73] Robin Tyburski et al. "Proton-Coupled Electron Transfer Guidelines, Fair and Square". In: *Journal of the American Chemical Society* 143.2 (2021), pp. 560–576. DOI: 10.1021/jacs.0c09106. URL: https://doi.org/10.1021/jacs.0c09106.

[74] Dandan Lyu et al. "Operando NMR electrochemical gating studies of ion dynamics in PEDOT:PSS". In: *Nature Materials* 22 (2023), pp. 746–753. DOI: 10.1038/s41563-023-01524-1.

[75] M. Pollak. "Effect of carrier-carrier interactions on some transport properties in disordered semiconductors". In: *Discussions of the Faraday Society* 50 (1970), p. 13. DOI: 10.1039/DF9705000013.

[76] D. H. L. Tjhe, X. Ren, I. E. Jacobs, et al. "Non-equilibrium transport in polymer mixed ionic–electronic conductors at ultrahigh charge densities". In: *Nature Materials* 23 (2024). Published: 26 July 2024, pp. 1712–1719. DOI: 10.1038/s41563-024-01953-6.

[77] Albert Einstein. *Investigations on the Theory of the Brownian Movement*. English translation of Einstein's 1905 paper. London: Methuen & Co. Ltd, 1926. URL: https://archive.org/details/investigationont0000albe/page/16/mode/2up (visited on 08/26/2025).

[78] A. Molina et al. "On the meaning of the diffusion layer thickness for slow electrode reactions". In: *Physical Chemistry Chemical Physics* 15 (2013). Published: 10 Dec 2012, pp. 2381–2388. DOI: 10.1039/C2CP43650G. URL: https://doi.org/10.1039/C2CP43650G.

[79] V. V. Gerasimov and I. L. Rozenfeld. "Effect of temperature on the diffusion current and the thickness of the diffusion layer". In: *Russian Chemical Bulletin* 5 (July 1956), pp. 797–801. DOI: 10.1007/BF01169982. URL: https://doi.org/10.1007/BF01169982.

[80] Frederick G. Cottrell. "Der Reststrom bei galvanischer Polarisation, betrachtet als ein Diffusionsproblem". German. In: *Zeitschrift für Physikalische Chemie* 42U.1 (1903). hdl:2027/uc1.b2655532, p. 385. ISSN: 2196-7156. DOI: 10.1515/zpch-1903-4229. URL: https://doi.org/10.1515/zpch-1903-4229.

[81] J. R. Delmastro and G. L. Booman. "Polarographic kinetic currents for first-order preceding and regeneration reactions at spherical electrodes". In: *Analytical Chemistry* 41.11 (1969), pp. 1409–1420. DOI: 10.1021/ac60279a015.

[82] Allen J. Bard, Larry R. Faulkner, and Henry S. White. *Electrochemical Methods: Fundamentals and Applications*. 3rd. Hoboken, NJ: Wiley, 2022. ISBN: 9781119334064.

[83] Hermann von Helmholtz. "Ueber einige Gesetze der Vertheilung elektrischer Ströme in körperlichen Leitern mit Anwendung auf die thierisch-elektrischen Versuche". In: *Annalen der Physik und Chemie* 165.6 (1853). In German, pp. 211–233. DOI: 10.1002/andp.18531650603.

[84] David C. Grahame. "Differential Capacity of Mercury in Aqueous Sodium Fluoride Solutions. I. Effect of Concentration at 25°". In: *Journal of the American Chemical Society* 76.19 (1954), pp. 4819–4823. DOI: 10.1021/ja01648a014.

[85] Katharina Doblhoff-Dier and Marc T. M. Koper. "Modeling the Gouy–Chapman Diffuse Capacitance with Attractive Ion–Surface Interaction". In: *The Journal of Physical Chemistry C* 125.30 (2021), pp. 16664–16673. DOI: 10.1021/acs.jpcc.1c02381.

[86] David J. Griffiths. *Introduction to Electrodynamics*. 3rd. p. 43. Upper Saddle River, NJ: Prentice Hall, 1999.

[87] Jaroslav Heyrovský and Jiří Kuta. *Principles of Polarography*. Translated by J. Volke. Prague: Publishing House of the Czechoslovak Academy of Sciences / Academic Press, 1965.

[88] John Newman. *Numerical Solution of Coupled, Ordinary Differential Equations*. Tech. rep. UCRL-17739. Report prepared under AEC Contract No. W-7405-eng-48. Lawrence Radiation Laboratory, University of California, Aug. 1967. URL: https://escholarship.org/uc/item/7qj7k1bb.

[89] Taewhan Yeu, Trung V. Nguyen, and Ralph E. White. "A Mathematical Model for Predicting Cyclic Voltammograms of Electronically Conductive Polypyrrole". In: *Journal of the Electrochemical Society* (1988). University of South Carolina Scholar Commons, Chemical Engineering Faculty Publications, pp. 1971–1976. URL: https://scholarcommons.sc.edu/eche_facpub/318.

[90] John Newman. *Numerical Solution of Coupled, Ordinary Differential Equations*. Tech. rep. UCRL-17739. Berkeley: Lawrence Radiation Laboratory, University of California, Aug. 1967.

[91] Aleksandar Y. Mehandzhiyski et al. "Digital twin of a standard electrochemical cell for cyclic voltammetry based on Nernst–Planck–Poisson model". In: *ACS Electrochemistry* 1.2 (2024), pp. 174–185. DOI: 10.1021/acselectrochem.4c00017. URL: https://doi.org/10.1021/acselectrochem.4c00017.

[92] Hao Wang, Alexander Thiele, and Laurent Pilon. "Simulations of cyclic voltammetry for electric double layers in asymmetric electrolytes: A generalized modified Poisson–Nernst–Planck model". In: *The Journal of Physical Chemistry C* 117.36 (2013), pp. 18286–18297. DOI: 10.1021/jp402181e. URL: https://doi.org/10.1021/jp402181e.

[93] Joshua W. Gallaway et al. "Operando identification of the point of $[Mn_2]O_4$ spinel formation during γ-MnO_2 discharge within batteries". In: *Journal of Power Sources* 321 (2016), pp. 135–142. DOI: 10.1016/j.jpowsour.2016.04.141. URL: https://doi.org/10.1016/j.jpowsour.2016.04.141.

[94] Adolf Fick. "Ueber Diffusion". In: *Annalen der Physik* 170.1 (1855). First published: 1855, pp. 59–86. DOI: 10.1002/andp.18551700105.

[95] Adolph Fick. "V. On Liquid Diffusion". In: *The London, Edinburgh, and Dublin Philosophical Magazine and Journal of Science* 10.63 (1855). Published online: 26 May 2009, pp. 30–39. DOI: 10.1080/14786445508641925.

[96] Walter A. Strauss. *Partial Differential Equations: An Introduction*. 2nd. Hoboken, NJ: John Wiley & Sons, 2008, p. 2.

[97] G. D. Smith. *Numerical Solution of Partial Differential Equations: Finite Difference Methods*. 3rd. Oxford: Oxford University Press, 1985.

[98] Randall J. LeVeque. *Finite Difference Methods for Ordinary and Partial Differential Equations: Steady-State and Time-Dependent Problems*. Philadelphia: Society for Industrial and Applied Mathematics (SIAM), 2007. ISBN: 978-0-898716-29-0.

[99] John Newman and Karen E. Thomas-Alyea. *Electrochemical Systems*. 3rd. Electrochemical Society Series. Hoboken, New Jersey: Wiley-Interscience, 2004. ISBN: 0-471-47756-7.

[100] K. Gustafson and T. Abe. "The third boundary condition—was it Robin's?" In: *The Mathematical Intelligencer* 20 (1998), pp. 63–71. DOI: 10.1007/BF03024402. URL: https://doi.org/10.1007/BF03024402.

[101] Camila Cendra et al. "Role of the Anion on the Transport and Structure of Organic Mixed Conductors". In: *Advanced Functional Materials* 29.1 (2019), p. 1807034. DOI: 10.1002/adfm.201807034. URL: https://doi.org/10.1002/adfm.201807034.

[102] E. J. F. Dickinson, J. G. Limon-Petersen, and R. G. Compton. "The electroneutrality approximation in electrochemistry". In: *Journal of Solid State Electrochemistry* 15.7-8 (2011), pp. 1335–1345. DOI: 10.1007/s10008-011-1323-x. URL: https://doi.org/10.1007/s10008-011-1323-x.

[103] Can Berk Uzundal. "Electrochemical Investigations of Ion Transport in Unconventional Environments". M.Sc. Thesis. Ankara, Turkey: Bilkent University, Graduate School of Engineering and Science, July 2018.

[104] I. T. Jolliffe. *Principal Component Analysis*. Springer Series in Statistics. New York: Springer-Verlag, 2002. ISBN: 978-0-387-95442-4. DOI: 10.1007/b98835.

[105] B. Ulgut et al. "A new interpretation of electrochemical impedance spectroscopy to measure accurate doping levels for conducting polymers: Separating Faradaic and capacitive currents". In: *Applied Surface Science* 256.5 (2009), pp. 1304–1308. DOI: 10.1016/j.apsusc.2009.10.031.

[106] B. Krische and M. Zagórska. "Overoxidation in conducting polymers". In: *Synthetic Metals* 28.1-2 (1989), pp. 257–262. DOI: 10.1016/0379-6779(89)90201-5.

[107] Gyözö G. Láng et al. "The Electrochemical Degradation of Poly(3,4-ethylenedioxythiophene) Films Electrodeposited from Aqueous Solutions". In: *Zeitschrift für Physikalische Chemie* 230.9 (2016), pp. 1281–1302. ISSN: 2196-7156. DOI: 10.1515/zpch-2016-0752.

[108] S. Garreau et al. "In Situ Spectroelectrochemical Raman Studies of Poly(3,4-ethylenedioxythiophene) (PEDT)". In: *Macromolecules* 32.20 (1999), pp. 6807–6812. DOI: 10.1021/ma9905674.

[109] Igor A. Vinokurov and Jouko Kankare. "Beer's Law and the Isosbestic Points in the Absorption Spectra of Conductive Polymers". In: *The Journal of Physical Chemistry B* 102.7 (1998), pp. 1136–1140. DOI: 10.1021/jp972702p.

[110] Jiarun Tu, Wensheng Cai, and Xueguang Shao. "Direct separation of faradaic and double layer charging current in potential step voltammetry". In: *Talanta* 116 (2013), pp. 575–580. ISSN: 0039-9140. DOI: 10.1016/j.talanta.2013.07.021. URL: https://www.sciencedirect.com/science/article/pii/S0039914013005948.

A Additional PCA Component Plots

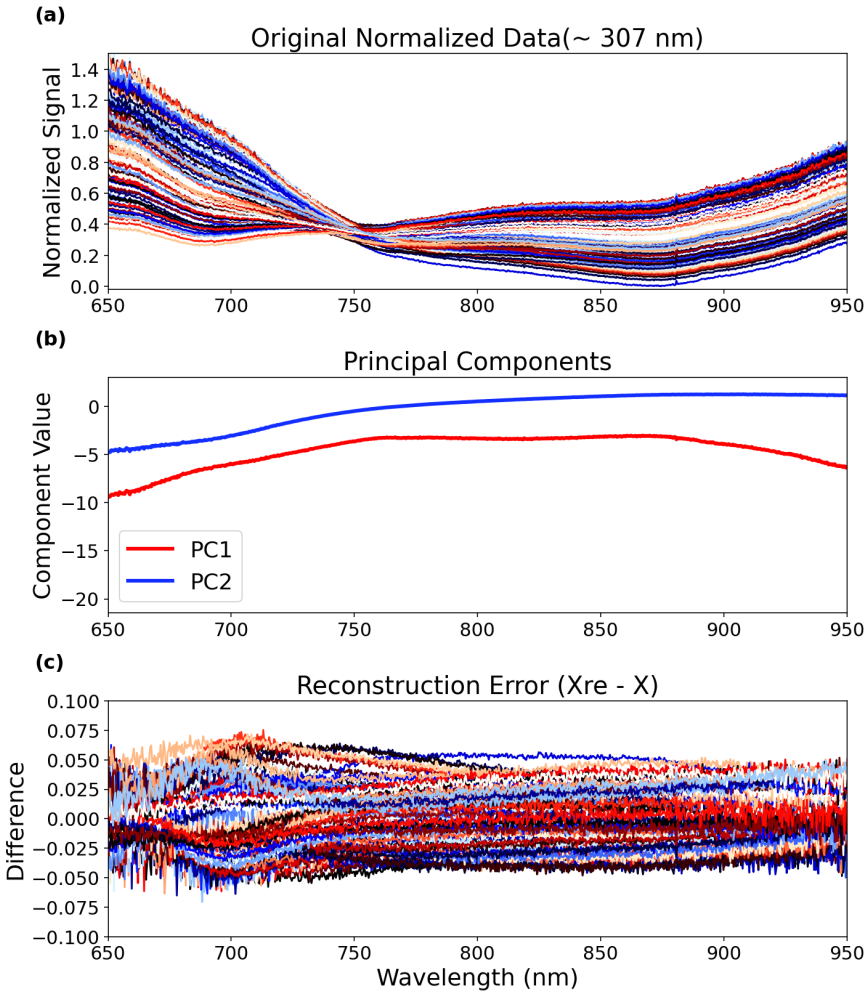

Figure .1: Reconstruction errors for the 307 nm film using one, two, and three principal components (PCs). The explained variance ratios for PC1 to PC5 are 95.47%, 4.30%, 0.10%, 0.054%, and 0.019%, respectively. Increasing the number of components from one to two drastically reduces the reconstruction error, while adding a third component results in only a marginal improvement.

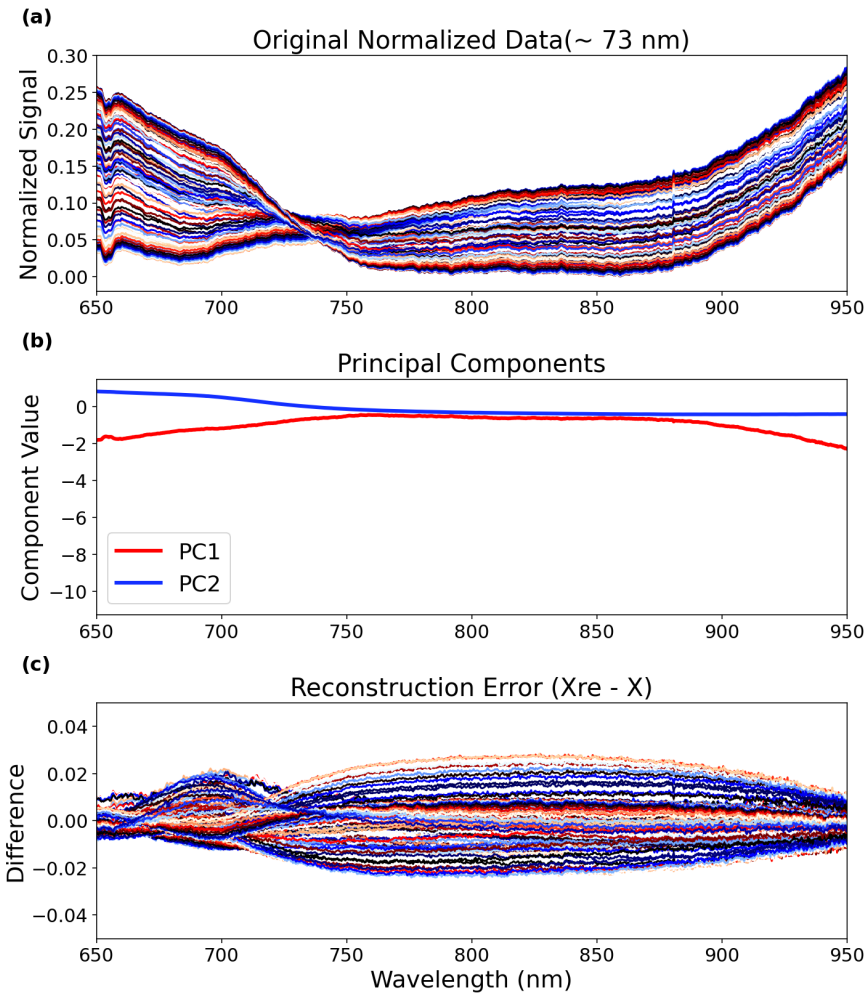

Figure .2: Principal component analysis for the 73 nm film. The first two PCs capture more than 99% of the variance, indicating that higher-order components contribute negligibly.

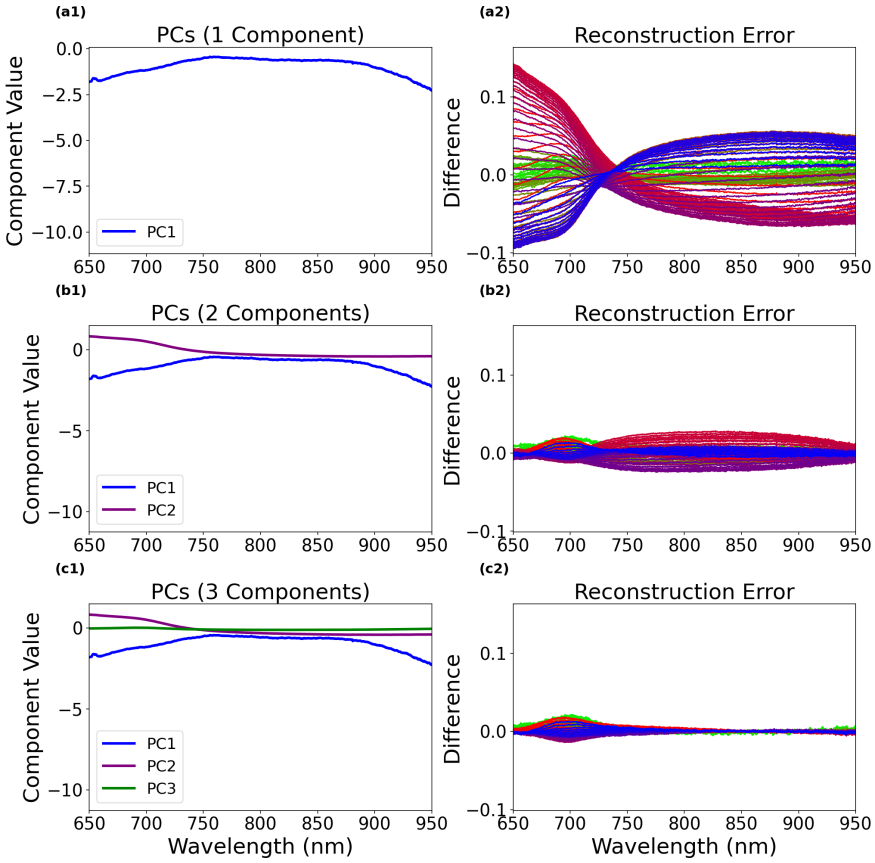

Figure .3: Reconstruction errors for the 73 nm film decrease sharply from one to two PCs, with little improvement for three (variance ratios: 95.04%, 4.90%, 0.026%).

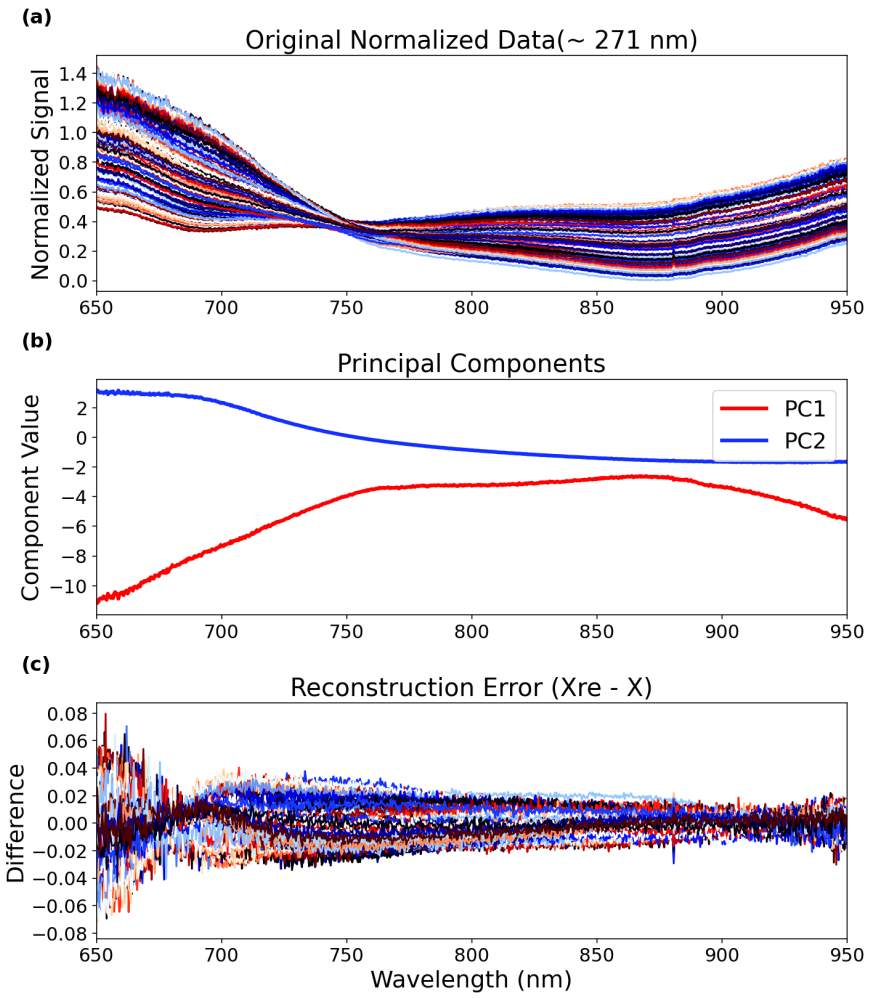

Figure .4: Principal component analysis for the 271 nm film. The first two components explain the vast majority of the variance.

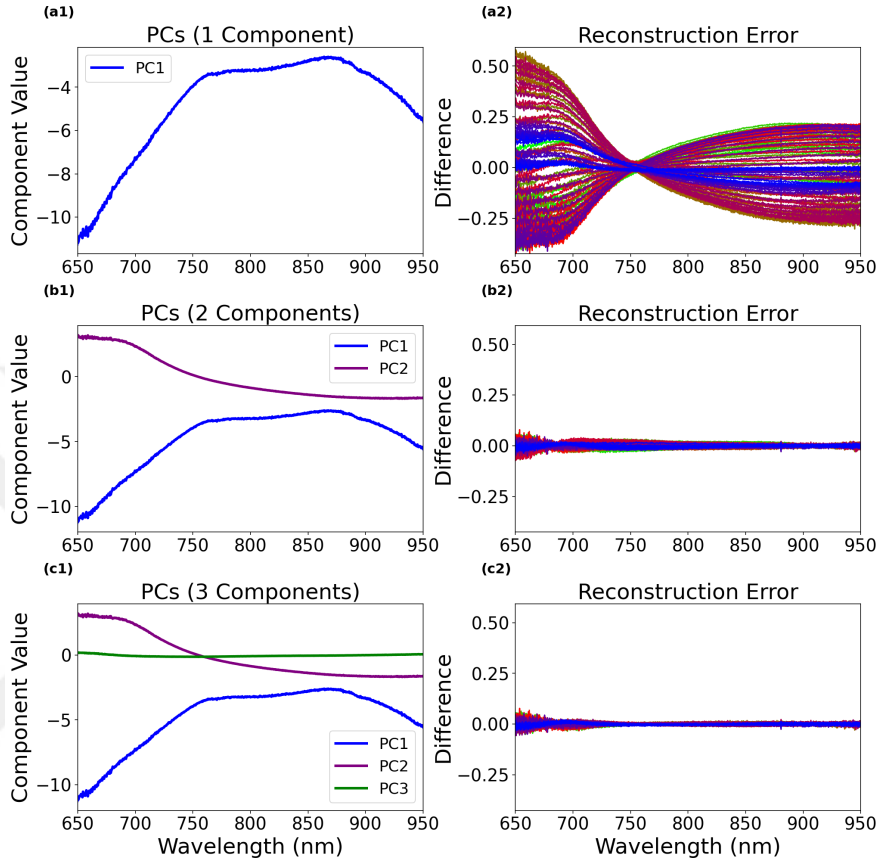

Figure .5: Reconstruction errors for the 271 nm film decrease sharply from one to two PCs, with minimal improvement for three (variance ratios: 95.04%, 4.90%, 0.026%).

B Additional Spectral Curve Fitting for the ≈307 nm Film

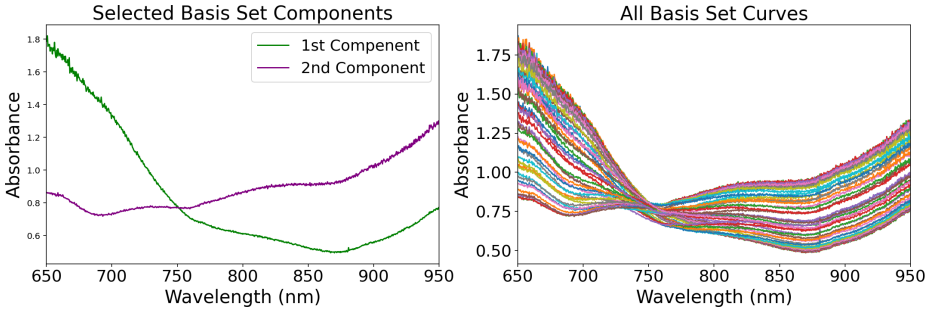

Figure .6: Basis set and spectral components used for fitting the ≈307 nm film.

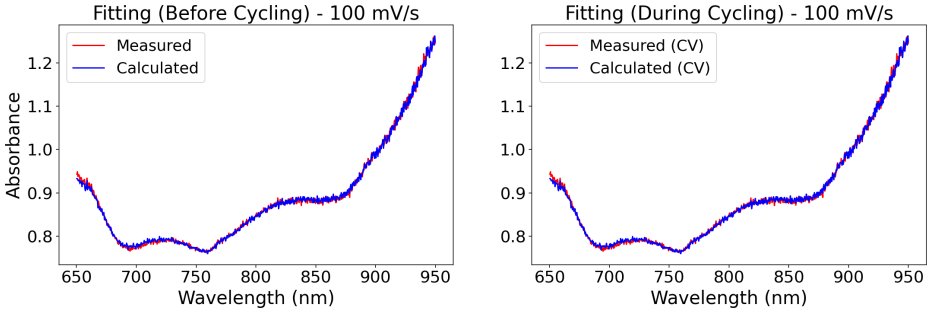

Figure .7: Spectral curve fitting of the 307 nm film at 100 $\mathrm{mV\,s^{-1}}$.

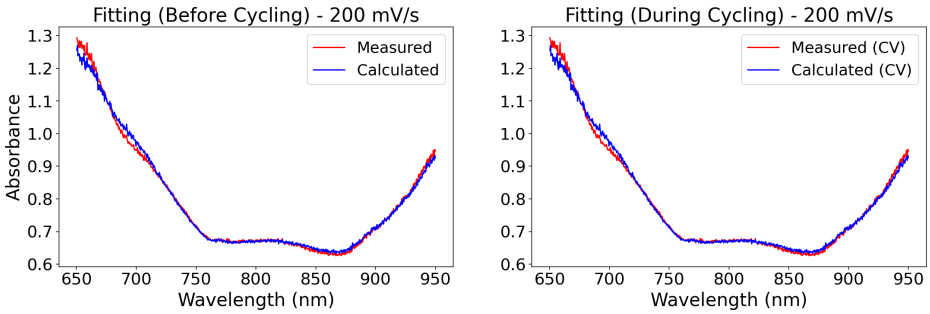

Figure .8: Spectral curve fitting of the 307 nm film at 200 $\mathrm{mV\,s^{-1}}$.

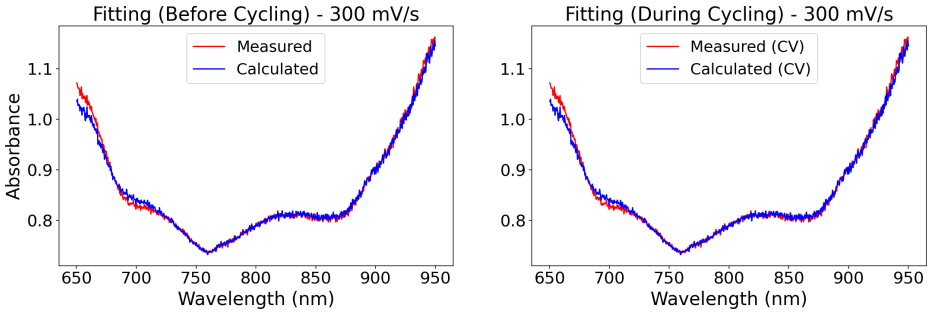

Figure .9: Spectral curve fitting of the 307 nm film at 300 $\mathrm{mV\,s^{-1}}$.

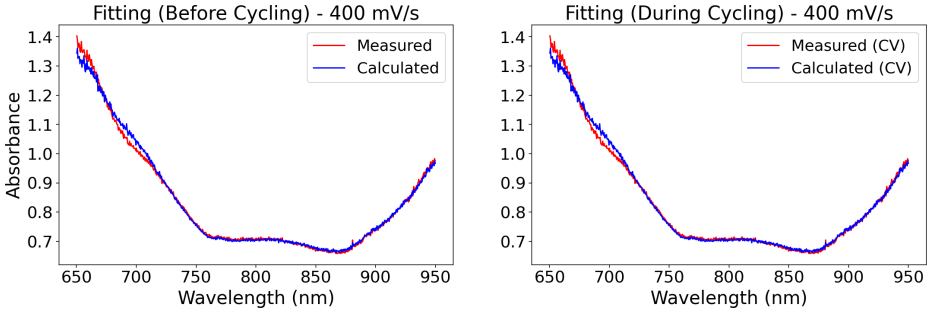

Figure .10: Spectral curve fitting of the 307 nm film at 400 $\mathrm{mV\,s^{-1}}$.

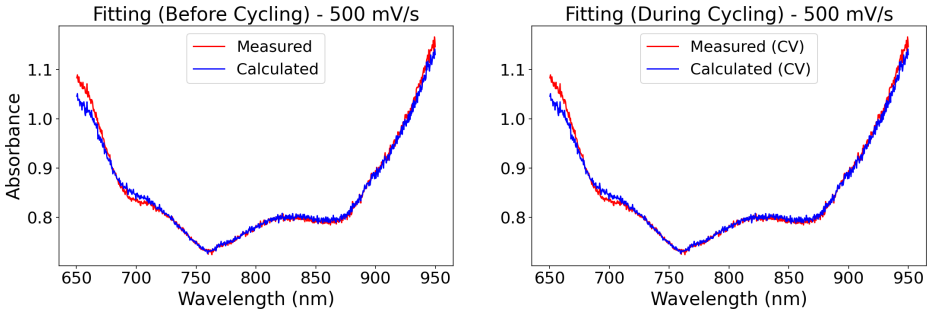

Figure .11: Spectral curve fitting of the 307 nm film at 500 $\mathrm{mV\,s^{-1}}$.

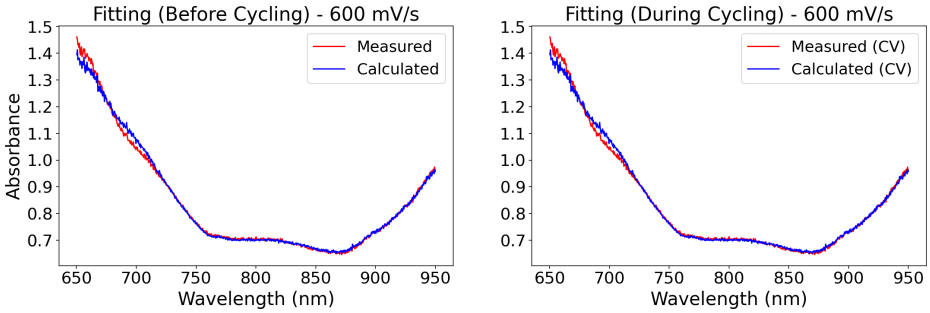

Figure .12: Spectral curve fitting of the 307 nm film at 600 $\mathrm{mV\,s^{-1}}$.

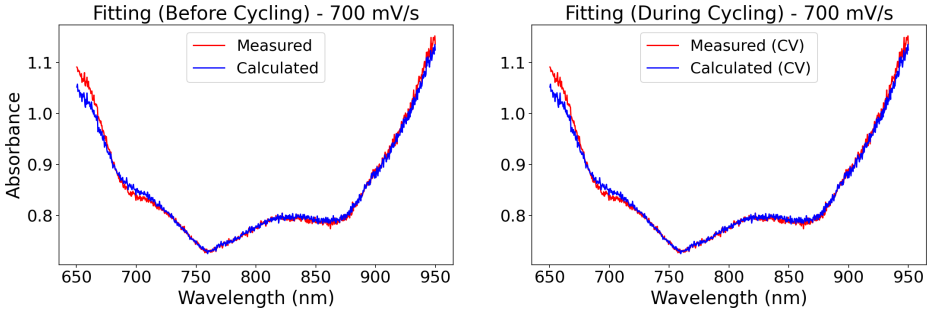

Figure .13: Spectral curve fitting of the 307 nm film at 700 $\mathrm{mV\,s^{-1}}$.

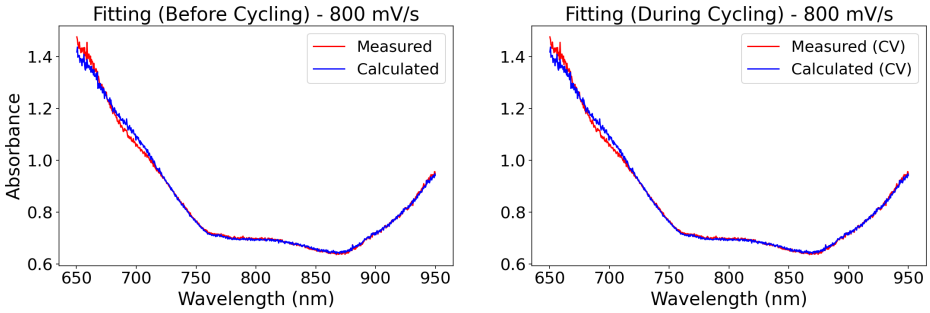

Figure .14: Spectral curve fitting of the 307 nm film at 800 $\mathrm{mV\,s^{-1}}$.

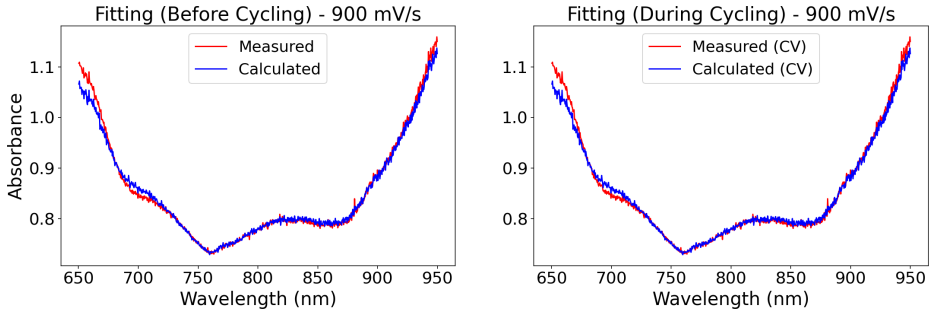

Figure .15: Spectral curve fitting of the 307 nm film at 900 mV s^{-1}.

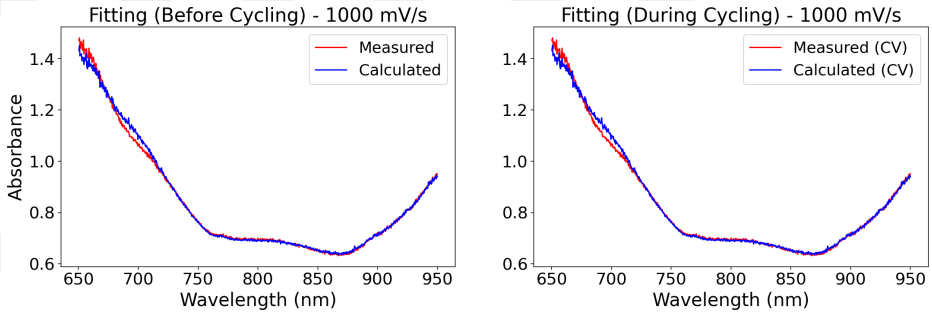

Figure .16: Spectral curve fitting of the 307 nm film at 1000 mV s^{-1}.

C Additional Results and Discussion Figures

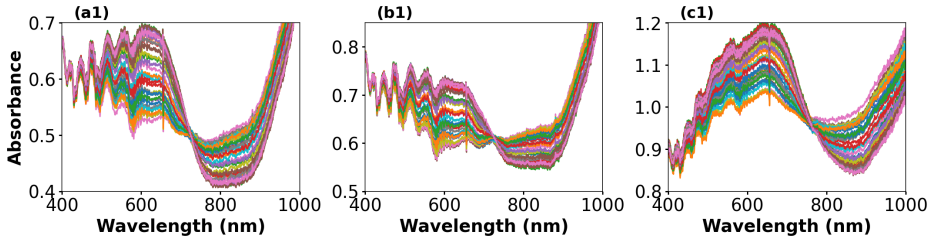

Figure .17: Basis set vectors representing the absorbance data obtained between 350–1100 nm during the potential sweep from −0.4 to 0.4 V.